

Insights into dyke emplacement mechanisms using new high-resolution 3D digital outcrop methods

Gregory M. Dering, BA, MSc



This thesis is presented for the degree of Doctor of Philosophy of The University of Western Australia
Centre for Exploration Targeting, School of Earth Science

Geology

2018

THESIS DECLARATION

I, Gregory Dering, certify that:

This thesis has been substantially accomplished during enrolment in the degree.

This thesis does not contain material which has been submitted for the award of any other degree or diploma in my name, in any university or other tertiary institution.

No part of this work will, in the future, be used in a submission in my name, for any other degree or diploma in any university or other tertiary institution without the prior approval of The University of Western Australia and where applicable, any partner institution responsible for the joint-award of this degree.

This thesis does not contain any material previously published or written by another person, except where due reference has been made in the text and, where relevant, in the Declaration that follows.

The work(s) are not in any way a violation or infringement of any copyright, trademark, patent, or other rights whatsoever of any person.

This research was supported by an Australian Government Research Training Program (RTP) Scholarship and was also funded by a student Top-Up scholarship from the CSIRO Office of the Chief Executive (now Research Plus) Science Leader funding program and the following ARC grants awarded to Assoc. Prof. Marco Fiorentini: CE110001017, FT110100241, and LP120100668.

This thesis contains published work and/or work prepared for publication, some of which has been co-authored.

Signature:

A solid black rectangular box redacting the signature of the author.

Date: Nov. 2, 2018

I present my credentials as a geologist, by stating that in my miscellaneous time I have been a stonemason, and also a great digger of ditches

—*Herman Melville, Moby Dick*

Dedication

For Mike Measures and the other Nevada geologists who introduced me to the craft of fieldwork

Abstract

Dykes are critical for the transport of magma through the crust. Their geometries, connectivity and internal textures preserve important information on dyke emplacement, linkage and magma dynamics. Unfortunately, our ability to develop new insights is limited by the resolution and continuity of data that can be extracted from the field. The emergence of digital photogrammetry along with Unmanned Aerial Vehicles (UAVs, *a.k.a.* drones) have expanded our capability to acquire data from geological outcrops with a precision and sampling density not previously feasible. Using these methods, dyke-related features can be measured across five orders of magnitude (mm to km). UAV-based imagery enables the observation of fine-scale textural features (phenocrysts, chilled zones, stepped margins) that are difficult to quantify on the ground. However, the significance of results depends on 3D model accuracy and resolution, which therefore are tracked and reported. Here, these techniques are reviewed and new approaches for the structural analysis of dykes are derived, which are applied to outstanding exposures of dyke swarms from Albany, southwestern Australia, and the Sierra Nevada, USA.

At Albany, a combination of ultra-high resolution, 3D photogrammetric models (3-4 mm per pixel) and field mapping enabled the identification of a spatial relationship between dyke-parallel faulting, jointing and dyke swarm emplacement. The data show mutually overprinting dyke-fault relationships and a symmetrical increase in the number of faults and joints towards the swarm, indicating that dyke emplacement and faulting were coeval. The identification of coeval dyke-parallel faulting is not expected but matches recent microseismicity surveys indicating shear failure along fault planes parallel to the orientation of intruding dykes. We present the first explanation for such dyke-parallel shear failure where, during dyke emplacement, the elastic properties of the host-rock change due to jointing, leading to local stress reorientation and the triggering of dyke-parallel shear fractures. Dyke-parallel shear failure may be more common than previously thought, especially during upper crustal intrusion events.

In the second study, the role of crystallisation and lateral linkage between dyke segments were examined. Three-dimensional dyke aperture measurements at exceptionally high resolution (3-5 mm per pixel), over strike distances up to ~100 m, yielded 20,000 measurements from 40 discrete dyke segments. This exceptionally dense and precise digital sampling method reveals flat-topped aperture-length profiles and a surprising fine-scale oscillation in dyke aperture. The data confirm the finding of previous studies that solidified dyke tips are commonly much blunter than predicted from linear elastic fracture mechanics. A new model for dyke linkage is presented that accounts for blunt tips between segments, second-order dyke aperture variations and evolution from tapered to flat topped aperture-length profiles. We suggest vertical channels of seismicity identified around laterally propagating dykes are the product of catastrophic linkage between segments, rather than volatile escape or vertical magma migration.

Table of contents

Chapter 1: Introduction	1
1.1 Context of this thesis	1
1.2 Aims of this thesis	2
1.3 Thesis organization	2
1.3.1 Thesis by papers and authorship	2
1.3.1.1 Chapter II	2
1.3.1.2 Chapter III	3
1.3.1.3 Chapter IV	3
1.3.1.4 Chapter V	3
1.3.2 Appendices	4
1.3.1.1 Supporting references	4
1.3.1.2 Lower crustal intrusion networks	4
1.3.1.3 Coauthor contributions external to thesis	5
1.4 References	5
Chapter 2: Review of drones, photogrammetry and emerging sensor technology for the study of dykes: Best practises and future potential	7
Abstract	8
2.1 Introduction	8
2.2 A practical guide for collecting high resolution data from volcanological outcrops	10
2.2.1 Digital photogrammetry	12
2.2.2 Best practise in UAV platform selection	12
2.2.3 Target definition and sampling resolution	16
2.2.4 Use of ground control points	20
2.3 Case studies	23
2.3.1 Example of mapping dyke-induced deformation	23
2.3.2 Example of high resolution aperture measurements	26
2.3.2.1 Extraction of dyke aperture data from non-uniform surfaces	26
2.3.2.2 Aperture result from an andesite dyke	29
2.3.3 Example of subtle lithologic control on dyke geometry	33
2.3.4 Summary	37
2.4 Emerging techniques and technologies	37
2.4.1 Sensors	37
2.4.2 Digital outcrop analysis	39
2.4.2.1 Automated and semi-automated fracture and lithology mapping	39
2.4.2.2 Structural analysis techniques	42
2.5 Discussion	43

2.5.1 UAV technologies as a step-change in field observation	43
2.5.2 Summary of survey quality reporting	44
2.5.3 Insights into volcanic processes using UAV-photogrammetry data	44
2.5.4 Educational value	45
2.6 Conclusion	46
2.7 References	48
Chapter 3: Evidence for dyke-parallel shear during syn-intrusion fracturing	56
Abstract	58
3.1 Introduction	59
3.2 Dyke-induced faulting, fracturing, and seismicity	60
3.2.1 Mechanical predictions	60
3.2.2 Geophysical observations	61
3.3 Geological Setting	64
3.3.1 Albany Fraser Orogen	64
3.3.2 Post-Albany-Fraser Orogen mafic intrusions	64
3.3.3 Vancouver Peninsula locality	65
3.4 Fracture and dyke mapping	67
3.4.1 UAV-assisted photogrammetry	67
3.5 Brittle deformation around dykes	70
3.5.1 Fracture populations	70
3.5.2 Pre- and syn-emplacement dyke-parallel shear	70
3.5.3 Decametre scanline results	71
3.5.4 Metre-scale scanline results	71
3.6 Discussion	80
3.6.1 Dyke-induced fracture zones	80
3.6.2 Conceptual model of dyke-related damage corridors	80
3.6.3 Implications for interpretation of dyke-induced seismicity	81
3.7 Conclusion	84
3.8 References	85
Appendix 3.1: Photogrammetric survey methods and measurement error	89
Appendix 3.2: Scanline data	92
Appendix 3.3: Geologic map of Mistaken Island locality	95

Chapter 4: Dyke propagation and scaling properties revealed from undulating apertures, captured by UAV	96
Abstract	97
4.1 Introduction	98
4.2 Geological setting	99
4.2.1 Study site	100
4.3 Methodology	103
4.3.1 Digital outcrop reconstruction	103
4.3.2 High resolution aperture measurements	104
4.4 Tip Zones	107
4.5 Aperture results	114
4.5.1 Blunt and flat-topped aperture profiles	114
4.5.2 Dyke segments	116
4.6 Discussion	121
4.6.1 Flat tops and blunt ends diverge from predicted aperture profiles	121
4.6.2 A breakout model for dyke growth	122
4.6.3 Aperture as a record of conduit evolution	122
4.6.4 Implications for the geophysical monitoring of dyke propagation	123
4.6.5 Implications for scaling relationships	124
4.7 Conclusion	126
4.8 References	127
Appendix 4.1: Supplemental dyke aperture data	132
Appendix 4.2: Physical parameters for aperture profile models	133
Chapter 5: Conclusion	136
5.1 Original research outcomes	136
5.1.1 Digital outcrop methodologies	136
5.1.2 Dyke-induced fracture corridors	136
5.1.3 Aperture variation	137
5.2 Future research	137
5.3 References	139
Appendix I	140
Appendix II	142
Appendix III	147
Appendix IV	149
Appendix V	151
Appendix VI	n/a
Appendix VII	n/a
Appendix VIII	n/a

Acknowledgements

It was a privilege to be supervised by Steve Barnes, Sandy Cruden, Marco Fiorentini, and Steve Micklethwaite. They each tended the direction of this thesis in their own way and it has been my sincere aim to produce a body of work that they could feel proud to be involved in.

The research presented here was largely funded by a Student Top-Up Scholarship from Steve Barnes and the CSIRO Mineral Systems Flagship. In addition to the opportunities afforded by this funding, I am grateful to Steve for his conscientious warmth, accessibility, and for including me in his research group at every opportunity.

My deep thanks to Sandy Cruden for steering me to the theory when I was lost in the data. And also for many careful edits that improved the precision of the writing and the geological thinking behind the words.

Marco Fiorentini introduced me to the joys of dunite, farmhouse ricotta, and thinking laterally in the southern Alps. For these things and his unwavering support in the preparation of this thesis, I am forever grateful.

From across a continent and sometimes more, Steve Micklethwaite was the guide and a mentor who mustered encouragement and new ideas when it was most needed.

I salute my peers and coauthors, Sam Thiele, Stefan Volgger, and Chris Gonzalez whose knowledge expanded my research.

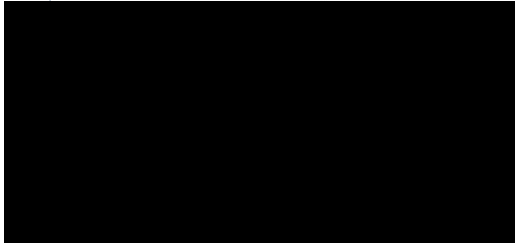
Thanks to Klaus Gessner and Ivan Zibra at the Geological Survey of Western Australia for their mentorship, invitation to collaborate, and financial support of my research.

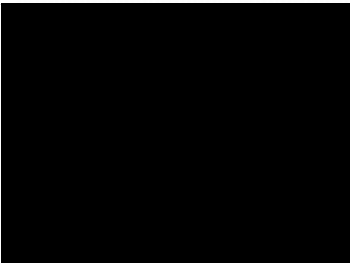
Dave Wagner of Independence, California provided an amazing base camp for Sierra Nevada field work. Work in eastern California was assisted by Ryan Anderson and John Anderson. In Western Australia, Eric Tohver and Michael O'Brien made fieldwork great fun.

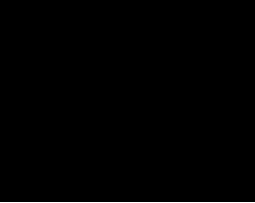
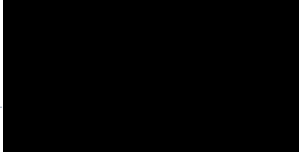
Above all, I thank my ever-patient fiancée, Stacia Gordon, who enabled this academic pursuit that took us both so very far from home. For four years she lifted my spirits and grounded my thoughts. For this and a thousand more things, I am forever grateful and in love.

AUTHORSHIP DECLARATION: CO-AUTHORED PUBLICATIONS

This thesis contains work that has been accepted for publication.

Details of the work:	
Title: Review of drones, photogrammetry and emerging sensor technology for the study of dykes: Best practises and future potential	
Publication: Journal of Volcanology and Geothermal Research, accepted Aug 2018	
Location in thesis: Chapter 2	
Student contribution to work: First author	
Co-author signatures and dates:	
	
<u>02/11/18</u>	<u>02/11/18</u>
icklethwaite	Samuel Thiele
<u>01/11/18</u>	
Alexander Cruden	

Details of the work:	
Title: Evidence for dyke-parallel shear during syn-intrusion fracturing	
Publication: Earth and Planetary Science Letters, accepted Sep 2018	
Location in thesis: Chapter 3	
Student contribution to work: First author	
Co-author signatures and dates:	
	
<u>02/11/18</u>	<u>02/11/18</u>
icklethwaite	Fiorentini
<u>01/11/18</u>	<u>02/11/18</u>
der Cruden	h J Barnes

Student signature		Date: 31/10/2018
I, Marco Fiorentini, certify that the student statements regarding their contribution to each of the works listed above are correct		
Coordinating supervisor signat		Date: 01/11/2018

Chapter 1: Introduction

1.1 Context of this thesis

Dykes are key components of intrusion networks responsible for the transfer of mafic magmas from the mantle into middle and upper continental crust. The geometry of dykes and associated host rock structures are widely used to understand the mechanisms and dynamics of emplacement. These processes have implications for understanding aspects of geology as diverse as volcanic hazards (Roman and Cashman, 2006) and the formation of some of the world's most valuable ore deposits (Barnes et al., 2016). Seismicity associated with active dyke propagation is used to track advance of magma through the crust. However, the mechanisms that trigger seismicity around dykes remain poorly known. A key process in the formation of many intrusion-related PGE-Ni-Cu deposits is protracted magma flux through long-lived conduits. If better understood, the organization of magma flux within crustal-scale intrusion networks and conditions leading to open-system behavior are potentially valuable criteria for targeting ore deposits. Both mineral exploration and volcanic hazard forecasts rely on predictive tools that incorporate a fundamental understanding of dyke emplacement (e.g Barnes and Mungall, 2018; Bonaccorso et al., 2011). However, significant questions persist regarding the processes that dominate successive phases of dyke emplacement, from nucleation, to propagation, to arrest, on which these predictions rely.

Insights into dyke emplacement and the surrounding deformation field have relied on the comparison of field data with analytical solutions from linear elastic fracture mechanics (e.g. Pollard and Muller; 1976; Delaney et al., 1981; Kusumoto et al., 2013). However, in recent decades new geophysical datasets have become available. In particular, the accumulation of seismological data of from dyke propagation events have revealed remarkable time-space relationships between dyke emplacement and deformation (Toda et al., 2002; Ebinger et al., 2010; Sigmundsson et al., 2015). In a broad sense, these studies show that firstly, the seismic energy released is in agreement with the energy required for dyke opening and secondly, seismicity tends to be concentrated around the propagating dyke edges. However, in detail, microseismicity is not restricted to the leading (i.e. active) edges of dykes and a large proportion of the events are not easily explained by existing theory from linear elastic fracture mechanics (Rivalta et al., 2015).

Similarly, studies that compare dyke geometries measured in the field with analytical solutions show significant misfits in aperture profiles (Delaney et al., 1981; Daniels et al., 2012). These studies point to the roll of inelastic deformation and differential solidification rates that are not incorporated into solutions from linear elastic fracture mechanics. However, these types of comparative studies have persistently been limited by the precision and abundance of field data.

To resolve outstanding questions about the mechanics of dyke propagation, linkage and internal magma dynamics, the next generation of data requires more continuous 3D structural measurements of

dykes and characterisation of other parameters at much greater resolution over large areas. The innovation of Structure-from-Motion (SfM) digital photogrammetry from multiple overlapping photographs has led to an explosion in high resolution 3D terrain reconstructions in the Earth sciences (Carrivick et al., 2016). Integrating this powerful image processing approach with unmanned aerial vehicles (UAVs) has enabled highly accurate 3D digital reconstruction of geological outcrops (e.g. Bemis et al., 2014; Pavlis and Mason, 2017).

1.2 Aims of this thesis

This thesis aims firstly to develop methods for the structural analysis of dykes in 3D digital outcrop models. The second component involves the application of these techniques to the analysis of dyke emplacement mechanisms and dyke-induced deformation.

UAV-photogrammetry offers the potential to investigate dyke-related structures at exceptionally high resolution and accuracy, with the ability to reproduce complex natural outcrop geometries. Developing digital analysis methods to capture structural aspects of dykes not readily obtainable by conventional field methods. A further aim is to attach a quantifiable level of confidence to structural data derived digital outcrop models.

In the first of two field investigations, this thesis aims to resolve outstanding questions regarding the extent of dyke-induced damage zones using conventional fracture analysis techniques, microstructural analysis, and the digital techniques described above.

The second field investigation aims to evaluate the role of non-elastic processes such as magma solidification emplacement and organisation of magma flux in dyke networks.

The results of this research have been communicated by numerous conference papers and three manuscripts prepared for publication, two of which have been accepted, so far.

1.3 Thesis organization

1.3.1 Thesis by papers and authorship

This thesis is presented as a series of three manuscripts in accordance with requirements of the UWA Graduate Research School. At the time of thesis submission, two chapters have been peer-reviewed and accepted for publication in *Journal of Volcanology and Geothermal Research* (Chapter 2) and *Earth and Planetary Science Letters* (Chap. 3). These chapters are formatted according to the respective journal requirements. Chapter 4 is formatted according to the requirements for the *Journal of Structural Geology*.

Chapter 2 provides a suite of methods and specific workflows for analysis of dykes from 3D digital outcrop data. Chapter 3 addresses questions of damage zone development around dykes which leads to surprising observations of dyke-parallel shear during swarm emplacement. Chapter 4 explores

mechanisms of dyke growth by measuring variation in dyke aperture at very high resolution. Chapter 5 summarises the main findings of the thesis and their implications for dyke swarm emplacement.

1.3.1.1 Chapter 2

Chapter 2 is titled “Review of drones, photogrammetry and emerging sensor technology for the study of dykes: Best practises and future potential” and was accepted for publication in the Journal of Volcanology and Geothermal Research (Aug. 17, 2018). The first author is Gregory Dering and is coauthored by Steven Micklethwaite, Samuel Thiele, Stefan Volgger, and Alexander Cruden. Dering was the main scientific investigator and author of the paper. Micklethwaite played a central role in manuscript redaction and authored section 2.4.1, on emerging sensor technology. Thiele authored section 2.4.2 on structural analysis techniques. Volgger and Cruden authored section 2.3.3, contributed Table 2, and participated in manuscript redaction.

1.3.1.2 Chapter 3

Chapter 3 is titled “Evidence for dyke-parallel shear during syn-intrusion fracturing” and was accepted for publication in Earth and Planetary Science Letters (Sep. 18, 2018). The first author is Gregory Dering and is coauthored by Steven Micklethwaite, Alexander Cruden, Stephen Barnes, and Marco Fiorentini. Dering was the main scientific investigator and author of the paper. Micklethwaite was critically involved in interpretations and manuscript redaction and participated in fieldwork. Cruden was central to data interpretation and manuscript redaction. Barnes was involved data collection and manuscript redaction. Fiorentini participated in manuscript redaction.

1.3.1.3 Chapter 4

Chapter 4 is titled “Dyke propagation and scaling properties revealed from undulating apertures, captured by UAV” and formatted as a manuscript for submission to Journal of Structural Geology. The first author is Gregory Dering and is coauthored by Steven Micklethwaite, Alexander Cruden, and Marco Fiorentini. Dering was the main scientific investigator and author of the manuscript. Micklethwaite was critically involved in fieldwork, interpretation, and manuscript redaction. Cruden contributed to data interpretation. Fiorentini was also involved in field work and manuscript redaction.

1.3.1.4 Chapter 5

In Chapter 5 the main scientific outcomes of the previous three chapters are summarized. The implications for the physical processes of dyke swarm emplacement are considered along with the future avenues of research capitalizing on UAV photogrammetry methods developed for analysis of dykes and similar geological structures in outcrop.

1.3.2 Appendices

Supplementary materials linked to chapters 3 and 4 are included at the end of those respective chapters. Additional work undertaken in the course of this PhD candidature are included as appendices following Chapter 5. Supporting references (appendices I–IV) are conference abstracts pertaining to research comprising the body of this thesis. Appendix V is an extended abstract first-authored by Dering which summarizes research into mafic intrusion networks in lower continental crust. Research presented in appendix V is conceptually linked to chapters 3 and 4, as all three address mechanisms and dynamics of mafic magma emplacement into continental crust. Appendices VI–VIII are peer-reviewed publications coauthored by Gregory Dering and external to the central aims and topics of this thesis.

1.3.1.1 Supporting references

Appendix I

Dering, G., Barnes, S., Micklethwaite, S., Cruden, A., Fiorentini, M., and Tohver, E., 2016, Dyke tips and melt pathways: Insights from UAV photogrammetry, 13th International Nickel-Copper-PGE Symposium, Fremantle, Western Australia.

Appendix II

Dering, G., Micklethwaite, S., Barnes, S., Fiorentini, M., Cruden, A., and Tohver, E., 2016, An Elevated Perspective: Dyke-related fracture networks analysed with UAV photogrammetry in Proceedings, 7th International Dyke Conference, Beijing, China.

Appendix III

Dering, G., Micklethwaite, S. and Cruden, A.R., 2016, December. High Resolution Analysis of Dyke Tips and Segments, Using Drones. Abstract V53B-3090, presented at American Geophysical Union Fall Meeting, San Francisco, Calif., Dec. 12-18.

Appendix IV

Dering, G., Micklethwaite, S., Barnes, S., Fiorentini, M., Cruden, A., 2016, Relating Seismicity to Dike Emplacement, and the Conundrum of Dyke-Parallel Faulting, Abstract V53B-3090, presented at American Geophysical Union Fall Meeting, San Francisco, Calif., Dec. 12-18.

1.3.1.2 Lower crustal intrusion networks

Appendix V

Dering, G.D., Gonzalez, C., Fiorentini, M., Davis, A., 2017, Arrested in the Ivrea Zone: Ni sulfide mineralisation in lower continental crust, La Balma igneous complex (NW Italian Alps), Society for Geology Applied to Mineral Deposits Biennial Meeting, Quebec City, Canada, 173-Vi29-63.

1.3.1.3 Coauthor contributions external to thesis

Appendix VI

Denyszyn, S.W., Fiorentini, M.L., Maas, R. and **Dering, G.D.**, 2018, A bigger tent for CAMP. *Geology*, 46(9), pp.823-826.

Appendix VII

Zibra, I., White, J.C., Menegon, L., **Dering, G.D.** and Gessner, K., 2018, The ultimate fate of a synmagmatic shear zone. Interplay between rupturing and ductile flow in a cooling granite pluton. *Journal of Structural Geology*, 110, pp.1-23.

Appendix VIII

Ord, A., Hobbs, B., **Dering, G.D.** and Gessner, K., 2018, Nonlinear analysis of natural folds using wavelet transforms and recurrence plots. *Phil. Trans. R. Soc. A*, 376(2126), p.20170257.

1.4 References

- Barnes, S.J. and Mungall, J.E., 2018, Blade-shaped dikes and nickel sulfide deposits: A Model for the emplacement of ore-bearing small intrusions, *Economic Geology*, v.113, p.789-798.
- Barnes, S.J., Cruden, A.R., Arndt, N. and Saumur, B.M., 2016, The mineral system approach applied to magmatic Ni–Cu–PGE sulphide deposits, *Ore Geology Reviews*, v.76, p.296-316.
- Bemis, S. P., Micklethwaite, S., Turner, D., James, M. R. Thiele, S., 2014. Ground-Based and UAV-Based Photogrammetry: A Multi-Scale, High-Resolution Mapping Tool for Structural Geology and Paleoseismology. *Journal of Structural Geology*, v.69, p. 163–178.
- Bonaccorso, A., Bonforte, A., Calvari, S., Del Negro, C., Di Grazia, G., Ganci, G., Neri, M., Vicari, A. and Boschi, E., 2011, The initial phases of the 2008–2009 Mount Etna eruption: A multidisciplinary approach for hazard assessment, *Journal of Geophysical Research: Solid Earth*, v. 116, B03203.
- Daniels, K.A., Kavanagh, J.L., Menand, T. and R. Stephen, J.S., 2012, The shapes of dikes: Evidence for the influence of cooling and inelastic deformation, *Geological Society of America Bulletin*, v.124, p.1102-1112.
- Delaney, P.T. and Pollard, D.D., 1981, Deformation of host rocks and flow of magma during growth of minette dikes and breccia-bearing intrusions near Ship Rock, New Mexico, U.S. Geological Survey Prof. Paper 1202, 69 p.

- Ebinger, C., Ayele, A., Keir, D., Rowland, J., Yirgu, G., Wright, T., Belachew, M. and Hamling, I., 2010, Length and timescales of rift faulting and magma intrusion: The Afar rifting cycle from 2005 to present, *Annual Review of Earth and Planetary Sciences*, v.38, p.439-466.
- Kusumoto, S., Geshi, N. and Gudmundsson, A., 2013, Aspect ratios and magma overpressures of non-feeder dikes observed in the Miyake-jima volcano (Japan), and fracture toughness of its upper part, *Geophysical Research Letters*, v.40, p.1065-1068.
- Pavlis, T.L. and Mason, K.A., 2017. The new world of 3D geologic mapping. *GSA Today*, v.27, no. 9, p. 4-10.
- Pollard, D.D. and Muller, O.H., 1976, The effect of gradients in regional stress and magma pressure on the form of sheet intrusions in cross section, *Journal of Geophysical Research*, v.81, p.975-984.
- Rivalta, E., Taisne, B., Bungler, A.P. and Katz, R.F., 2015, A review of mechanical models of dike propagation: Schools of thought, results and future directions, *Tectonophysics*, v.638, p.1-42.
- Roman, D.C. and Cashman, K.V., 2006, The origin of volcano-tectonic earthquake swarms, *Geology*, v.34, p.457-460.
- Sigmundsson, F., Hooper, A., Hreinsdottir, S., Vogfjord, K.S., Ofeigsson, B.G., Heimisson, E.R., Dumont, S., Parks, M., Spaans, K., Gudmundsson, G.B., Drouin, V., Arnadottir, T., Jonsdottir, K., Gudmundsson, M.T., Hognadottir, T., Fridriksdottir, H.M., Hensch, M., Einarsson, P., Magnusson, E., Samsonov, S., Brandsdottir, B., White, R.S., Agustsdottir, T., Greenfield, T., Green, R.G., Hjartardottir, A.R., Pedersen, R., Bennett, R.A., Geirsson, H., La Femina, P.C., Bjornsson, H., Palsson, F., Sturkell, E., Bean, C.J., Mollhoff, M., Braiden, A.K. and Eibl, E.P.S., 2015, Segmented lateral dyke growth in a rifting event at Bardarbunga volcanic system, Iceland. *Nature*, 517(7533): 191-U158.
- Toda, S., Stein, R.S. and Sagiya, T., 2002, Evidence from the AD 2000 Izu islands earthquake swarm that stressing rate governs seismicity, *Nature*, 419, p.58-61.

Chapter 2

Review of drones, photogrammetry and emerging sensor technology for the study of dykes: Best practises and future potential

Accepted for publication in Journal of Volcanology and Geothermal Research

Gregory M. Dering¹, Steven Micklethwaite², Samuel T. Thiele², Stefan A. Volgger², Alexander R. Cruden²

Corresponding author: Gregory Dering (gregory.dering@research.uwa.edu.au)

¹ARC Centre of Excellence for Core to Crust Fluid Systems, School of Earth Science, The University of Western Australia, Crawley, Western Australia 6009, Australia

²School of Earth, Atmosphere, and Environment, Monash University, Clayton, 3800, Australia

Abstract

Dykes are critical for the transport of magma through the crust and their geometries, connectivity and internal textures preserve important information on dyke emplacement, linkage and magma dynamics. Unfortunately, our ability to develop new insights is limited by the resolution and continuity of data that can be extracted from the field. The emergence of Unmanned Aerial Vehicles (UAVs, *a.k.a.* drones), photogrammetry and other sensor techniques are set to greatly improve our field capabilities. Here we present a workflow emphasising best-practice in UAV survey design, the construction of photogrammetric models and standardised reporting of those models. Emphasis is given to the factors that should be considered in order to resolve the geological features of interest in any study (e.g. wall rock fractures, chilled margins, magmatic breccias, dyke apertures etc). A point-to-raster technique is documented that measures spatial error in the rasters that are derived from photogrammetric models (e.g. orthomosaics and digital elevation models). Using three case studies, we show how dyke swarms can be mapped accurately over areas approaching 1 km², at sub-centimetre resolution. The data illustrate how questions about dyke-induced deformation, host rock controls on segmentation and aperture variation may be addressed, and we present a method for the high density, high precision measurement of dyke apertures in 3D. We also review semi-automated mapping tools and emerging UAV sensing techniques, including hyperspectral and aeromagnetic sensors, and the potentially important contributions they will make to the study of intrusive systems and volcanology more broadly.

2.1 Introduction

The shapes, orientations, associated host rock deformation, and internal textures of dykes, reflect the ambient stress field, emplacement mechanisms, and physical properties of magma (viscosity, velocity, composition, temperature) at the time of dyke formation (e.g. Anderson, 1938; 1951; Delaney and Pollard, 1981; Ernst et al., 1995; Jolly and Sanderson, 1995). Both outcrop exposures and geophysical monitoring of intrusion events provide crucial insight into these processes. In the context of volcano monitoring, dyke-induced deformation has been related to a variety of geophysical signals, including microseismicity (Mt Augustine, Alaska; Cervelli et al., 2006), changes in topography (Mt Etna, Sicily; Ruch et al., 2013), and ground motion (Bárðarbunga, Iceland; Sigmundsson et al., 2015). Consequently, understanding dyke growth and internal magma dynamics has implications for eruption forecasting (e.g. Acocella and Neri, 2009) or other hazards such as volcano flank collapse (Canary Archipelago, Elsworth and Day, 1999). Similarly, exposures of ancient dyke systems in eroded/exhumed settings, provide important insight into controls on the geometry, segmentation, connectivity and internal dynamics of dykes, which complement geophysical observations of modern magmatic systems.

In a recent review, Rivalta et al. (2015) point out that surprisingly few studies of dykes combine both field observations and mechanical models despite the fact that significant debate exists around the process of dyke emplacement and dyke-induced deformation. Existing analytical solutions are dominated

by two schools of thought that describe the principle mechanism of dyke emplacement as controlled by the elastic properties of the host rock (e.g. Weertman, 1971) or, alternatively, as a function of forces acting upon the magma (e.g. Lister and Kerr, 1991). In principle, insights into dyke emplacement mechanisms can be gained by careful mapping of dyke geometries, wall rock deformation and internal textures. At present, the field-based data reported from studies of ancient dykes consist of some combination of dyke width (aperture), exposed length, orientation (strike and dip), opening direction, segmentation, internal textures (flow banding, vesicle alignment, chilled margins, etc.), and fracturing or thermo-mechanical brecciation and erosion in the host rock. Detailed mapping, which is routinely used to capture these data, is typically accomplished by some combination of grid mapping, differential GPS, and aerial imagery (e.g. Delaney et al, 1986; Carracedo, 1994); an approach that is time consuming, subject to interpretation bias (Jones et al., 2004), and covers relatively small surface areas. Our ability to distinguish between emplacement and linkage mechanisms is affected not only by the limited number of observations we can make around individual dykes, but also the possibility that dyke geometry undergoes post-emplacement changes due to magma withdrawal (Daniels et al., 2012). To resolve outstanding questions about the mechanics of dyke propagation, linkage and internal magma dynamics, the next generation of data requires more continuous 3D structural measurements of dykes and characterisation of other parameters at much greater resolution over large areas.

The innovation of Structure-from-Motion (SfM) digital photogrammetry from multiple overlapping photographs has led to an explosion in high resolution 3D terrain reconstructions in the Earth sciences. The potential to produce highly accurate 3D scene reconstructions using UAV photogrammetry (Eisenbeiss, 2009) has been repeatedly demonstrated by benchmarking 3D point clouds against equivalent data collected by laser scanning techniques (James and Robson, 2012; Smith and Vericat, 2015; Micheletti et al., 2015). However, to date photogrammetry workflows in geoscience have emphasised the reconstruction of terrain surfaces (e.g. Rippin et al., 2015; Oúedraogo et al., 2014), whereas little attention has been given to constraining the ability of surveys to resolve features with different pixel colour information (textural accuracy) but little variation in topographic relief. Likewise, techniques to measure and extract structural geometries and detail from bedrock surfaces are in their infancy.

In this paper we describe how UAV-based SfM methodologies can be applied to the mapping and analysis of dykes and their host rocks. This review concerns micro UAVs, which are those with a maximum combined weight < 25 kg, because this is the technology that has become readily available and is regularly being used by the research community. We first lay out a pragmatic methodology for 3D reconstruction of dykes exposed in outcrop. Then, through a number of case studies, demonstrate how measurements of dyke-related structures and textures can be derived from the resulting 3D outcrop data. We discuss best-practise in reporting models and quantifying errors. These techniques advance field

measurements by attaching quantifiable precision to field data and collecting measurements at a density that has been previously unachievable. Although we focus here on the mapping of dykes, the methods and workflows outlined can be applied to a large range of studies requiring outcrop mapping.

2.2 A practical guide for collecting high resolution data from volcanological outcrops

Here we discuss the factors that should be considered when planning photogrammetric surveys to produce digital outcrop models with the appropriate topographic and textural resolution to be able to extract accurate measurements and distinguish textural features of dykes, or associated deformation. We also suggest a protocol for reporting error that has the advantage of being independent of photogrammetry software used to produce dense point clouds, orthorectified images, and DEMs.

At the outset, it is important to plan the extent, resolution, and accuracy required to generate a useful digital outcrop model for any given study. The workflow in Figure 1 outlines the steps that should be considered when designing a survey that is fit-for-purpose. The workflow emphasises the need to first consider the minimum and maximum dimensions of the geological features one is trying to resolve before designing a survey.

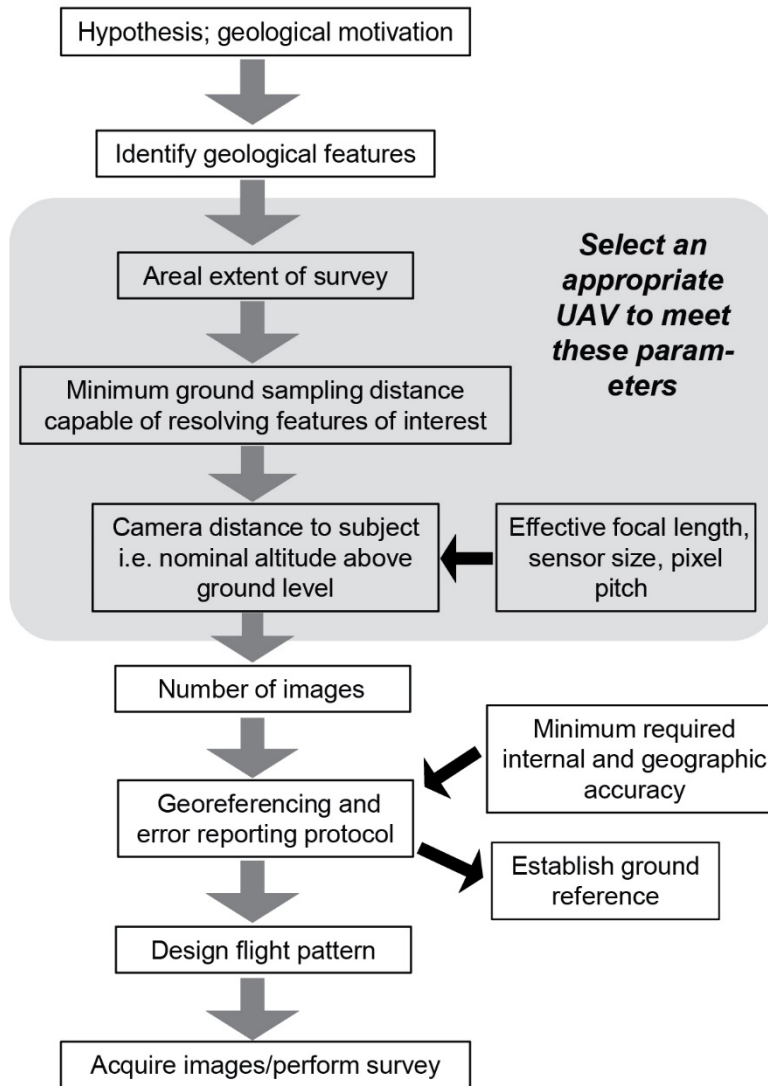


Figure 1 A hypothesis-driven workflow for photogrammetry survey planning that incorporates geological parameters into the design.

2.2.1. *Digital photogrammetry*

Digital photogrammetry is a technique which combines computer vision and photogrammetry algorithms to extract 3D geometries from a series of digital 2D images. The workflow begins by detecting and matching features (arrays of pixels) between overlapping images which capture a static scene from different locations. Providing a sufficient number of feature matches are correctly identified, the ‘structure’ of the scene can then be reconstructed, and the camera positions, orientations, and lens properties are estimated in order to produce a so-called sparse point cloud. The sparse point cloud and associated camera information are the basis for a much more detailed reconstruction using Multi-View Stereo (MVS) methods. The result is a dense point cloud which provides a 3D photorealistic representation of the colour, texture, and geometry of the scene. Derivative products such as triangulated textured meshes, orthomosaics and DEMs can then be generated as required (c.f. Bemis et al., 2014), although as we will demonstrate later analysis can also be conducted directly on the point cloud. For a more detailed discussion of SfM and MVS methods in geoscience, see Carrivick et al. (Chap. 3, 2016).

Generation of digital outcrop with SfM-MVS methods is attractive for the combination of ease of use, low cost and flexibility, as compared to alternatives such as laser scanning (LiDAR). Unlike traditional photogrammetry which relies firstly on a stereo view of image pairs that are precisely offset, and secondly, the use of metric cameras, SfM functions without prior input of camera position or orientation. In practical terms, using the SfM-MVS technique geologists may document an outcrop in 3D by collecting images with as little as a handheld camera and a scale bar. Workflows for SfM-MVS processing are now accessible via a number of open-source and commercial software platforms (https://en.wikipedia.org/wiki/Comparison_of_photogrammetry_software), many of which were listed by Bemis et al. (2014).

The quality of dense point clouds (and derivative products) is highly dependent on the quality of the input images, the distribution of camera locations, the scene properties and reference information. Therefore, in the following sections we describe protocols for ensuring high quality results for digital outcrop reconstruction. These are applicable to both terrestrial and aerial image acquisition, but we discuss the protocol in terms of UAV-based acquisitions.

2.2.2 *Best practise in UAV platform selection*

UAV photogrammetry surveys need to be designed based on resolution requirements (size of features be resolved), surface area and outcrop morphology (steep cliff or coastal platform), which dictate the choice of equipment (fixed-wing versus multi-rotor UAV). The resolution of the resulting 3D point clouds, orthomosaics and DEMs depends on the so-called ground sampling distance (GSD; otherwise known as ground pixel size) which can be understood as the distance that 1 pixel within an aerial image represents in the real world (e.g., 7mm per pixel). It follows that a smaller GSD will result in a high-resolution model. The GSD is governed by the choice of camera equipment (physical size of sensor,

sensor resolution, focal length) and the distance above ground level or distance to the object (Fig. 2). Therefore, it is important to determine the desired GSD before first choosing equipment and planning the survey. For example, it is impractical to employ a fixed-wing UAV to acquire imagery with sub-cm resolution because it would have to fly at a very low altitude which would result in blurry imagery (due to the speed required to maintain flight) that is unsuitable for SfM processing. For such cases, a multi-rotor UAV that allows flying at low horizontal flight speeds and low altitudes should be favoured to guarantee sharp imagery at high spatial resolution and overlap.

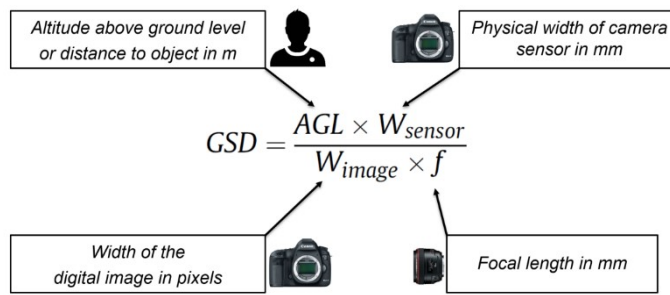


Figure 2 Ground sampling distance (GSD) as a function of camera parameters and distance to subject.

The majority of modern UAVs can be operated with mission planning software, which allows them to automatically follow predefined waypoints and systematically acquire aerial imagery with a set image overlap and GSD. The flight planning software is typically implemented via an app that is running on a smartphone or tablet computer. Multirotor UAVs manufactured by DJI currently enjoy wide use in the scientific community and so, in Table 1 we summarise popular flight planning software that is available for these machines.

A final consideration for survey design is the environmental conditions in which the UAV will operate, namely time of day, wind, temperate and altitude at the site. Time of day dictates to some extent the lighting conditions. Ambient lighting conditions are ideal (cloud cover, middle of the day; c.f. Bemis et al., 2014) unless shadows in the scene have the advantage of illustrating features of interest. In environments generally subject to windy conditions, fixed wing UAVs are affected by the wind direction and wind speed more so than multirotor UAVs. Survey design needs to consider wind direction when being planned, in particular as flight paths can deviate from planned and camera positions can be tilted. If deploying a UAV at greater altitudes, lift is inhibited and flight times are reduced, so surveys are forced to cover smaller areas. Ambient temperature is also known to impact battery life and motor performance (as specified by the manufacturer), again affecting flight time and the area over which a survey should be designed. Good safe practice mandates that any UAV survey also needs to assess these environmental factors before flight.

Software Name	Operating system(s)	Cloud processing capabilities	Source reference	Best use case	Pros	Cons
MapPilot	iOS only	YES	https://support.dronesmadeeasy.com	Flat or hilly landscapes (e.g., coastal platforms, stockpiles, etc.)	<ul style="list-style-type: none"> - Highly automated workflow - Terrain following - Photogrammetry survey templates (normal, grid and line mission) - Automatic flight speed adjustment to minimise motion blur - Multi-battery management 	
FlyLitchi	iOS Android	NO	https://flylitchi.com/	Complex surveys such as steep cliffs, pit walls or tall structures (e.g., towers)	<ul style="list-style-type: none"> - Highly flexible survey design - Online mission planning hub for waypoint missions 	No survey templates
DJI GS Pro	iOS only	NO	https://www.dji.com/ground-station-pro	Flat or hilly terrain (e.g., coastal platforms, stockpiles, etc.) and tall structures	<ul style="list-style-type: none"> - Flight planning survey templates - Tower mapping feature 	
UGCS Pro	Android Windows	NO	https://www.ugcs.com	All	<ul style="list-style-type: none"> - Spatial data importable for flight planning - Photogrammetry survey templates - Terrain following - Multi-battery management - Supports wide range of UAVs - Supports simultaneous UAV flights 	Laptop and tablet required
Pix4DCapture	iOS Android	YES	https://pix4d.com/product/pix4dcapture	Flat or hilly terrain and tower-shaped structures	<ul style="list-style-type: none"> - Photogrammetry survey templates - Import KML/KMZ (Android only) - Supports wide range of UAVs - Generates project file for photogrammetric processing with Pix4D 	
Dronedeploy	iOS Android	YES	https://www.dronedeploy.com	Flat or hilly terrain (e.g., coastal platforms, stockpiles, etc.)	<ul style="list-style-type: none"> - Real time cloud processing during flight - Flight pattern survey templates 	

Table 1 Selected flight planning apps for UAV photogrammetry

2.2.3 Target definition and sampling resolution

Geologic features in outcrop require sufficient pixel resolution to be distinguished. Therefore identifying the size of geological feature(s) of interest prior to image acquisition is an important early step in photogrammetric survey design. The key parameters are the minimum feature dimension (typically on the order of cm to mm) and the pixel resolution (typically mm to cm per pixel side length) sufficient to characterise the geological feature, which is calculated from GSD (Fig. 2). The significance of GSD is illustrated by the dyke tip zone shown in Figure 4 where the amount and type of geological information depends on the resolution of texture and also whether it is an orthomosaic or point cloud. For reliable feature identification, in practise we find that the GSD should be at least 2–3 times finer than the feature dimensions. For example, if a GSD of 20 mm were used to resolve features such as veins with similar widths, the vein information will only be visible as a single pixel or split across several pixels.

Understanding the minimum required GSD is the basis for planning the survey layout (Fig. 3). Adjusting the distance-to-subject for the camera is the simplest way to control GSD and it is recommended that a lens of fixed focal length and images are acquired at maximum resolution. In practice, the GSD of topographic high areas is smaller than low areas which are farther from the sensor. GSD variations due to topography can, in some cases, be mitigated by terrain-following UAV flights. It is also important to note that GSD describes the ground area captured by each pixel on the camera sensor under ideal conditions, and for many UAV surveys of fixed flight height, the nominal GSD is an average that ignores topography, such that the realised GSD will vary across a scene.

There are several other factors which can compromise image quality and lead to an effective image resolution lower than expected. These include 1) blurring caused by camera motion during exposure, 2) image noise or artefacts due to the selection of high ISO values or highly reflective outcrop surfaces, 3) poorly focused images due to lens vibration or inaccurate focus adjustments. Motion blur and image noise are generally avoidable when camera parameters are taken into account during flight planning, as described in Vollgger and Cruden (2016) and O'Connor et al. (2017). Motion blur is a significant enough factor for some flight planning apps to automatically limit UAV ground speed to prevent this affect. While low quality images are best omitted from SfM-MVS analysis, a small loss of information due to some combination of all three factors is considered normal. To compensate for this minor loss of image fidelity, it is prudent to plan a survey around a GSD that has redundancy, e.g. by being ~20% shorter (i.e. finer sampling resolution) than the required minimal orthomosaic resolution for the project. As an example, for a project requiring an orthomosaic resolution of 6 mm, the field survey would be designed around a GSD of 5 mm.

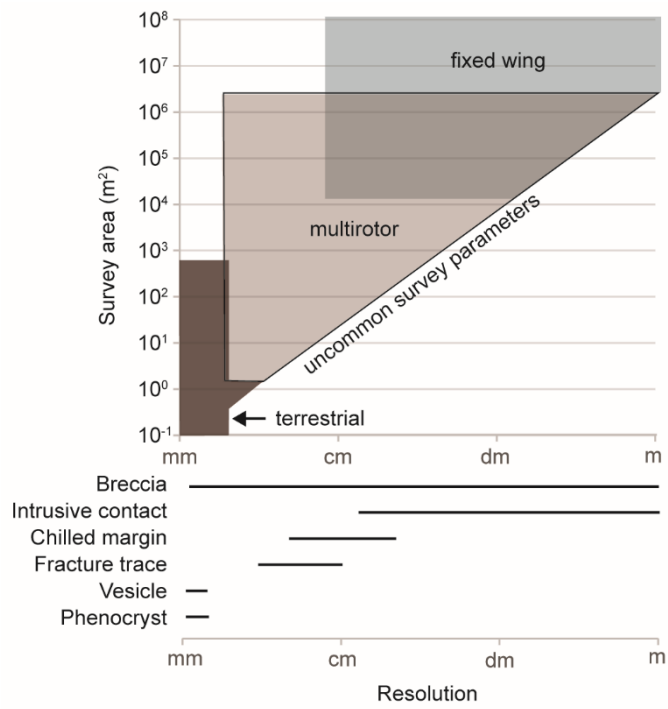


Figure 3 The appropriate camera platform for a photogrammetric survey depends on both the areal extent and required sampling resolution. Some geological features and the approximate resolution requirements that are relevant to dykes are also given.

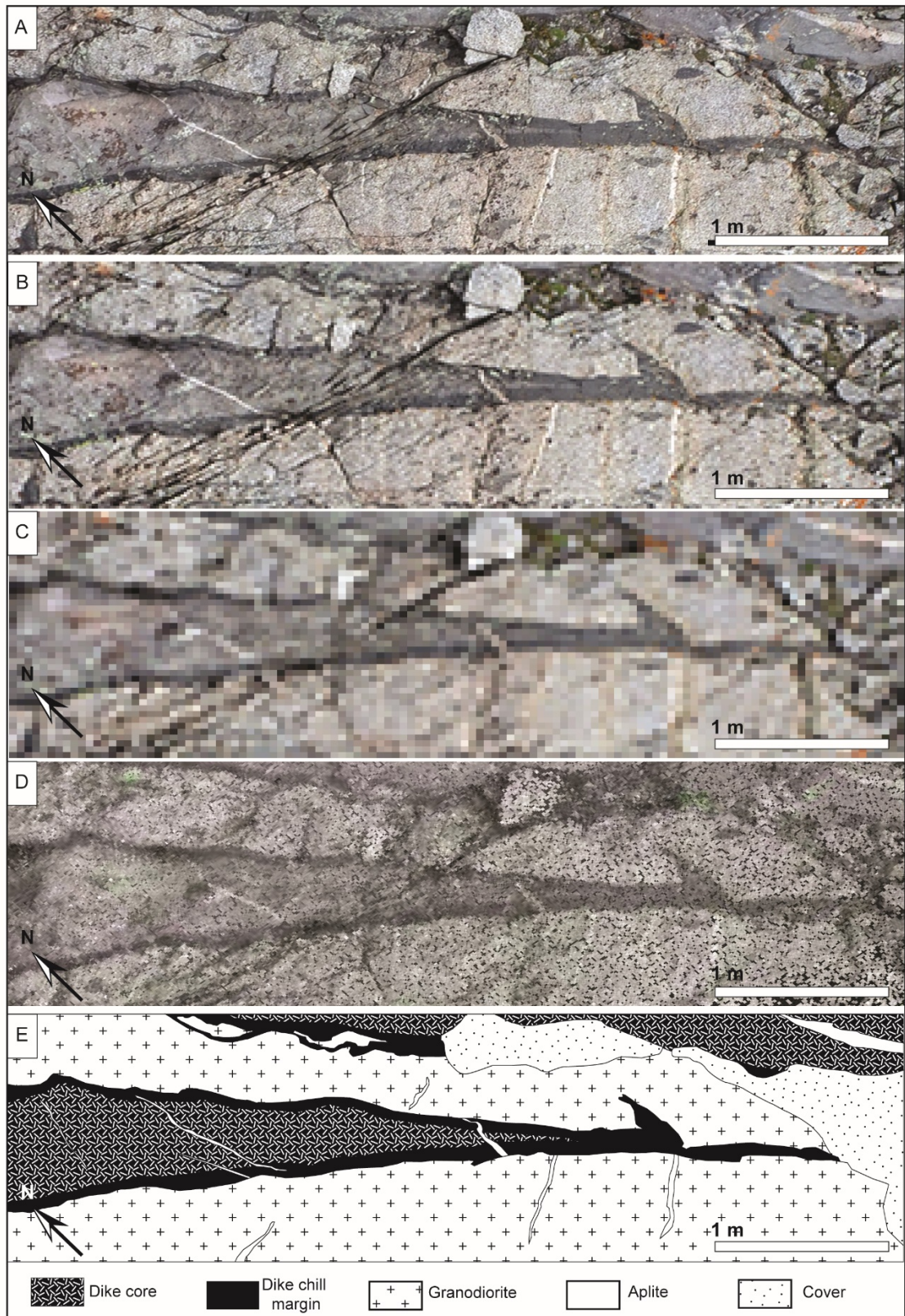


Figure 4 Comparisons of 2D images of an andesite dyke tip illustrate the differences in textural data available for interpretation and analysis. (a) 8 mm resolution orthoimage; (b) 16 mm orthoimages; (c) 80 mm orthoimages; (d) Dense point cloud; (e) Geologic map manually produced using the 8 mm orthoimage.

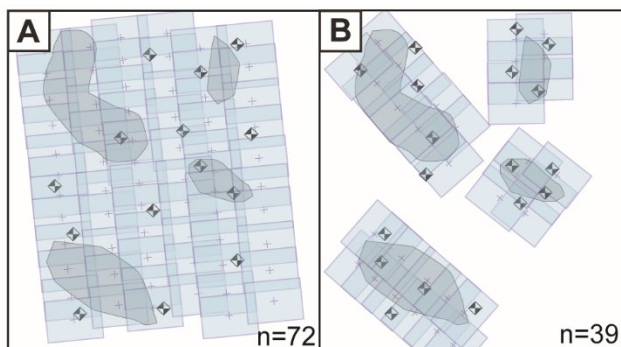


Figure 5 Schematic maps of aerial survey designs illustrate two approaches to mapping of patchy bedrock exposure (gray polygons) and the deployment of ground control points (black and white markers). The downward field of view for each aerial camera location is given by blue rectangles. (a) The continuous approach requires many images that do not contain useful information about the bedrock. (b) Breaking the project into four smaller areas encompasses the same bedrock extent using fewer images with the same field of view. Dividing the area into smaller surveys is computationally more economical, though requires georeferencing of multiple photogrammetric models.

Finally, the computational cost of photogrammetric processing can become prohibitive when dealing with very high resolution or large numbers of images. Strategies to economise processing time that are implemented within photogrammetry software packages include splitting image sets into smaller chunks and reducing the number of pixel pairs sought between images. However, an alternative approach at the survey design stage is to optimise survey extent to minimise processing of images lacking useful geological information. A common example relevant to the study of dyke outcrops is to simply segment a survey area with patchy bedrock exposure into multiple models (Fig. 5).

2.2.4 Use of ground control points

Spatial control on models can be achieved by use of scale bars or an array of surveyed ground control points (GCPs) and/or air control points that reference the camera positions associated with individual images during the UAV flight (e.g. images geotagged by on-board GPS). Control points are typically used to scale and orient the model in a meaningful spatial reference frame, commonly with respect to a geographic coordinate reference system such as Universal Transverse Mercator (UTM), though any type of coordinate reference system could be used. In addition, GCPs can be used to refine camera lens calibration during model generation within photogrammetric software (such as Agisoft Photoscan). The more accurate the survey tool used to constrain the GCPs, the more accurate the lens calibration and subsequent models. We outline here how GCPs can also be used to constrain errors independent of the errors reported by photogrammetric software, using a point-to-raster method.

Reporting of spatial error for SfM-MVS models has become standard practice, however there is presently no consensus among practitioners concerning the density or configuration of GCP arrays (James et al., 2017; Carrivick et al, 2016). We suggest two reasons to use GCPs to evaluate spatial accuracy for high precision outcrop studies, as opposed to relying upon onboard-GPS. Firstly, there are widely accessible ground-based tools for surveying, with centimeter to sub-centimeter precision, such as differential GNSS and total station systems. Secondly, the onboard GPS accuracies of small UAVs tend to have poor precisions of several meters that are often inadequate for high resolution studies of dykes in outcrop. Notwithstanding this, technology is advancing, and onboard GPS is improving rapidly. Likewise, the relatively low precision of air control points can be mitigated using a recent method presented by James et al. (2017), which demonstrates that an optimised best-fit of a large number (>100) air control points can still result in a model of accuracy that approaches the precision of GCPs in the right conditions. However, James et al. (2017) report that where highest precision (i.e. sub-cm) GCPs are available, the accuracy of these models exceeds what has been achieved by georeferencing methods relying solely on air points.

For those surveys where GCPs and high precision GPS equipment are available, establishing the GCP array is commonly the most time-consuming field step in a photogrammetric survey. Indeed, using a large number of GCPs does not necessarily guarantee an increase in the spatial accuracy of SfM-MVS

models (Smith and Vericat, 2015, James et al., 2017), but remains the simplest way to measure model error. A dense point cloud may be georeferenced with as few as three GCPs but this is not recommended as accuracy is compromised in parts of the model that lie far from the GCPs (e.g. Oúedraogo et al., 2014). If GCPs are clustered, or arrayed along an approximate line, the GCPs provide limited rotational constraint and so the model may be erroneously rotated around an axis falling along GCPs.

The point-to-raster workflow, comparing surveyed and modelled ground control points to yield error measurements is as follows:

1. We suggest the distribution of a minimum of 20 GCPs across the survey area as evenly as possible. Based on our experience, 10 GCPs are adequate to georeference a model with the remaining points being used to measure the variance in error.
2. Locations of GCPs are measured to high precision with either a total station or differential GPS.
3. Half of the ground control points are then used to georectify the dense point cloud, whereas the others (referred to here as validation points) are reserved to measure georeferencing errors in the dense point cloud and derived products. In our experience a minimum of 10 GCPs set aside for comparison purposes are necessary to capture error across the model.
4. Root Mean Square error is then used to quantify the difference between predicted and measured locations of validation points in the models.

This is a straight-forward workflow that quantifies the distribution of spatial errors associated with the photogrammetric reconstruction process (Fig. 6), independent of the errors reported in photogrammetric software. As discussed by James et al., (2017), spatial error is introduced at multiple steps in the photogrammetric processing workflow. These will all contribute to the RMS error derived from the point-to-raster technique. In addition, distortions will arise from the fact that rasters (orthomosaic and DEM) are 2D projections of a 3D surface. Therefore, the error measured by the point-to-raster technique represents a maximum error because it is the cumulative error of all the prior processing steps. Accurate photogrammetric models will yield small misfits between the arrays of modelled and measured points. In using this approach, the best models are those where the point-to-raster RMS error is calculated to be less than the measurement error of individual GCPs.

We suggest that any SfM-MVS survey used for quantitative analysis needs to report spatial errors as best practise. Regardless of whether an internal or geographic coordinate system is being used, GCP error reflects the internal precision of the model geometry. Since typical spatial error is on the order of 0.1-1% of total model dimensions (James and Robson, 2014), GCP survey precision should exceed these values.

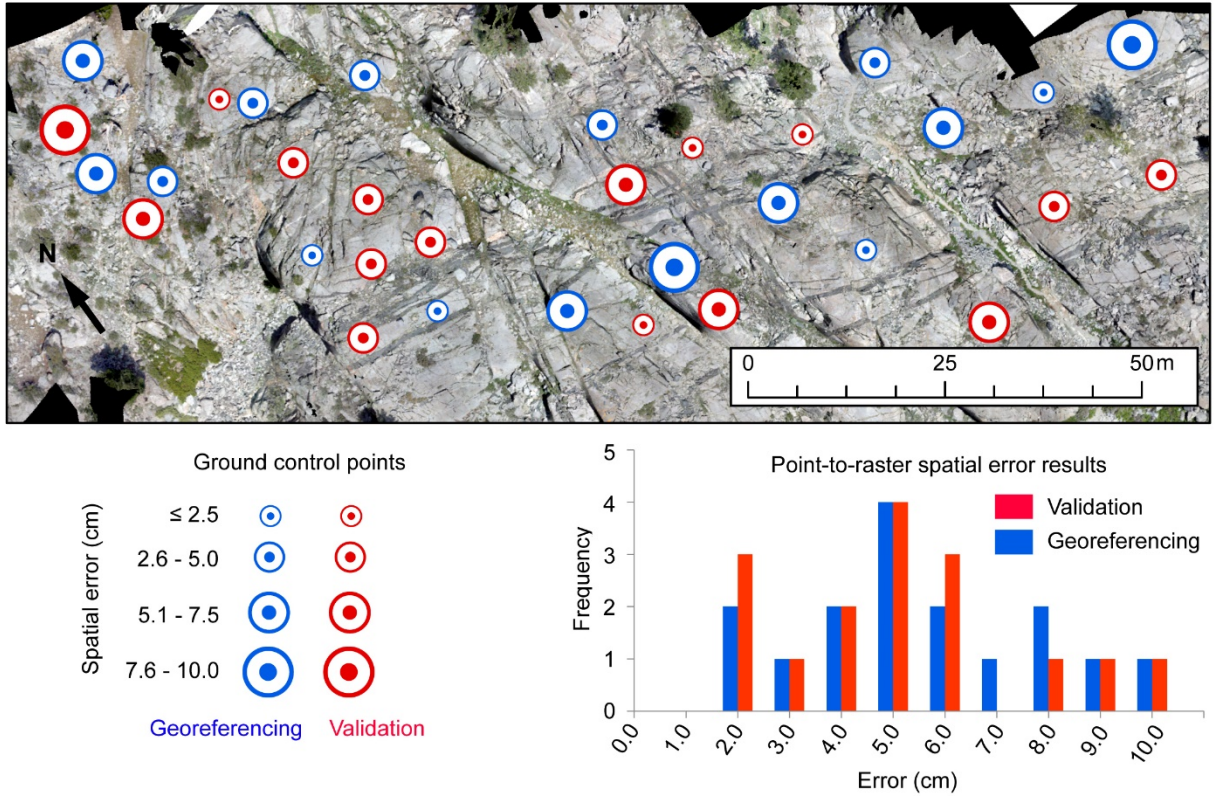


Figure 6 Example of a point-to-raster error analysis that yields root mean square error for ground control points. Validation points (red) have slightly higher overall error as compared with ground control points used in the model building process (blue).

2.3 Case studies

In this section we highlight three case studies that illustrate the advantages that UAV-based photogrammetry brings to field studies of dykes in outcrop, and how the level of structural and textural data obtainable has the potential to lead new insights not previously possible. The errors and appropriate reporting of the survey metrics associated with these studies are reported in section 2.5.2.

2.3.1 Example of mapping dyke-induced deformation

To better understand the distribution and role of brittle deformation associated with dyke emplacement, UAV photogrammetry was used to analyse a swarm of dolerite dykes and cataclasite-bearing faults and joints exceptionally well-exposed in a wave-cut platform on the south coast of Western Australia (Dering et al., 2019). The ultra-high resolution dataset covered a large surface area and made it possible to measure structural spacing and orientation across three orders of magnitude (centimetres to tens of metres). The quality of the dataset permitted proper evaluation of the evidence that host rock brittle deformation played a role in dyke emplacement despite pre-existing fractures in the host rocks introducing a high degree of structural complexity.

The study area comprises a 500 m long swath of continuous bedrock that is approximately 20 m wide and separates a bay from sandy bushland. The dykes are steeply dipping ($>85^\circ$) and have an average strike that is at high angles to the coastline such that the study area exposes a near perpendicular transect across the swarm (Fig. 7). The dykes range from <1 to 5 m wide and cross-cut felsic migmatitic orthogneiss and coarse-grained monzogranite. Both joints and faults occur in the host rock around the dykes and are mainly parallel to dyke margins. Field relations combined with petrography from the fault rocks indicate faulting was coeval with the earliest phase of dyking but preceded the bulk of magma emplacement (Dering et al., 2019).

The UAV flight plan was designed to assess the intensity of dyke-induced fractures across the dyke swarm and in the surrounding host rock domains. In order to resolve fine fracture traces in the host rock across the entire study area, the UAV survey encompassed 13,000 m² with a realised GSD of 4 mm. The photogrammetric model 3D geometry and location was constrained by an array of 30 ground control points surveyed with a Leica TS06 total station. Half of the ground control points were used to georectify the dense point cloud, whereas the other half were reserved to double-check the accuracy of the orthorectified image and DEM derived from the dense point cloud (referred to here as validation points). Ground control locations were measured with a minimum precision of ± 4 cm. The small uncertainty on the precision of the ground control locations arises from the propagation of measurement error to second and third base station locations. These additional base station locations were required due to lack of line-of-sight from a single base station to all 30 ground control points along an outward-curving coastline.

The images were processed with Agisoft Photoscan v.1.2 to produce a dense point cloud, from which a DEM (7.0 mm/pixel) was derived by processing using so-called high quality settings and an even higher resolution orthorectified image (3.5 mm/pixel) derived by processing at maximum quality settings. Traces of planar structures (fractures, faults, dyke walls, gneissic foliation) that intersect the outcrop surface were identified using the orthomosaic and interpolated in 3D using height information from the DEM.

Structural orientation measurements were collected digitally using the planes of best fit for each fracture, fault, and dyke, determined by implementation of a least squares regression analysis in Java, following the methods of Thiele et al. (2015). With these methods, it was possible to make structural measurements at multiple scales, from millimetre to decimetre distances from dyke margins using 1D line sampling methods commonly referred to as scanline mapping (Huang and Angelier, 1989; Bai and Pollard, 2000). A more recent technique enabling structural orientations from point cloud data makes the collection of structural orientation and trace data considerably easier (Thiele et al., 2017b) and is discussed more in Section 2.4.2 of this review.

Key results of the study are summarised in Figure 7 and their implications explored in more detail in Dering et al., (2019). Fault-fracture density increases around the dyke swarm suggesting a causal relationship but this could only be identified when the entire fault-fracture populations was assessed over hundreds of metres. Shear fracture orientations were found to be sub-parallel to Mode I dyke margins (Dering et al., 2019) and this led to the suggestion that dyke-parallel shear fracturing was occurring during emplacement, which has parallels with modern-day seismological observations of dyke intrusion events (White et al., 2011). Importantly, for this review, environmental factors (weather and tide) mean that traditional field techniques would not have been able to achieve the same observations under consistent conditions. The UAV-based photogrammetric approach collected the initial data in consistent light conditions during 4 flights (~ 1 hour total flight time), plus GCP set up (~ 3 hours). The resulting photogrammetric model enabled the entire fracture population to be analysed in its entirety under the same lighting conditions, ensuring a consistency of measurement. Scanlines for fracture density measurement were set digitally to be orthogonal to dyke orientations without being affected by tides. The dataset facilitated field work by providing base maps for metre scale transects to examine the mm-scale fracture density around dykes. Furthermore, because the data is inherently digital it was possible to integrate it with regional geophysical data for a true multi-scale analysis. Recently, other UAV-based approaches to examine structure-dyke relationships in the field were able identify thermomechanical influences on jointing during near-surface dyke emplacement (Townsend et al., 2015). However, the authors are unaware of other studies yet published, which illustrates the opportunity to apply UAV-based photogrammetry to this field of research.

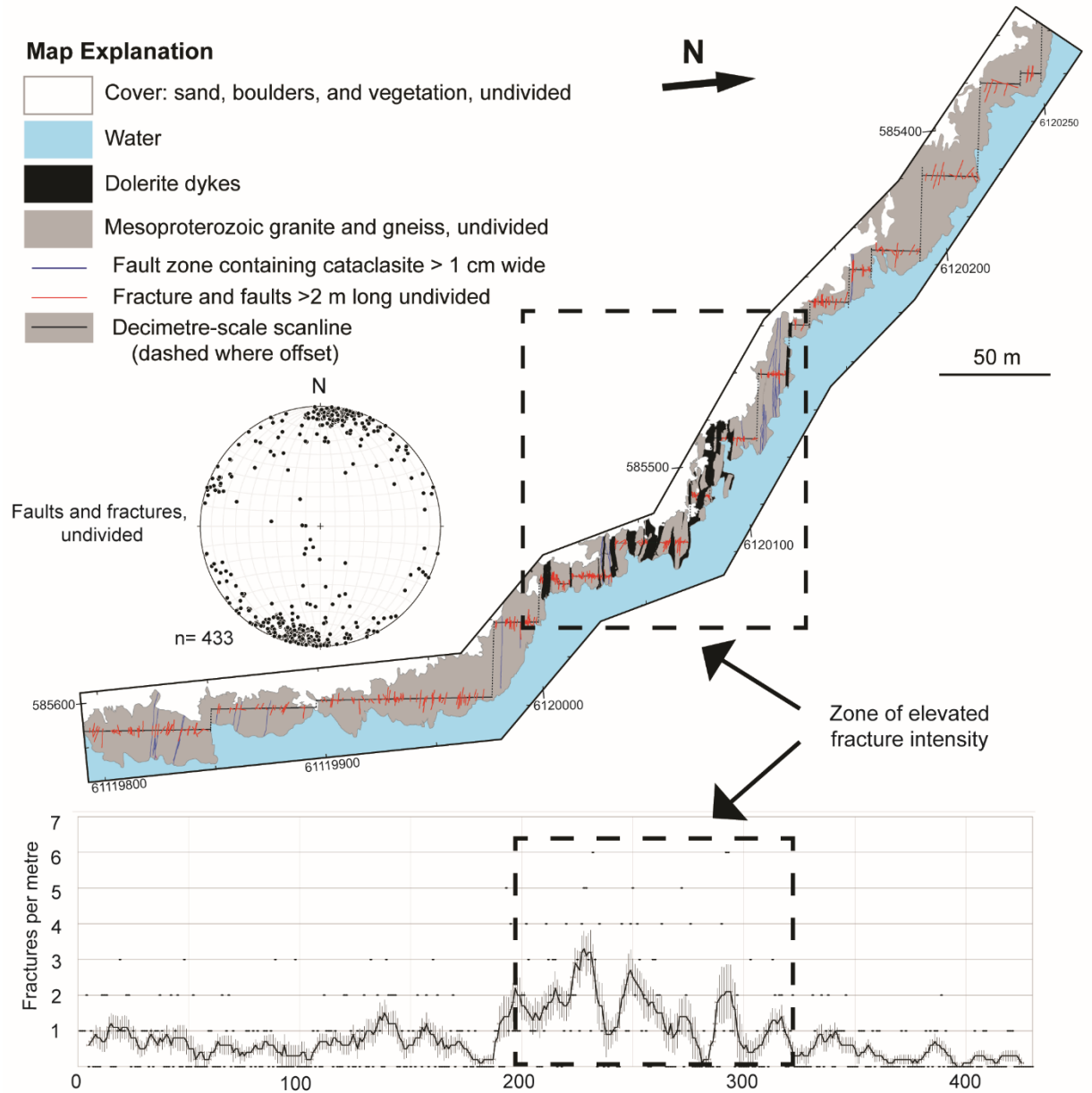


Figure 7 An example of high resolution fracture density data collected using a UAV photogrammetry model from Albany, Western Australia (after Dering et al., 2019). The transect is approximately 0.5 km long and centred around a mafic dyke swarm. The structural data are derived from the 3D outcrop model and projected to a 1D scanline that shows the elevated fracture intensity within a corridor that hosts the dyke swarm that is detected at length scales exceeding 100 m.

2.3.2 Example of high resolution aperture measurements

While dykes are commonly idealised as pressurised fluid-filled cracks, detailed aperture datasets that describe changes within individual dyke segments have found aperture to vary irregularly by 30-50% along dyke strike (Gudmundsson et al., 2012 and references therein). Other aperture studies have demonstrated that many solidified dyke shapes poorly fit the length-width proportions and taper geometries predicted by elastic theory (Daniels et al., 2012; Kavanagh and Sparks, 2011). However, systematic measurement of aperture is time consuming and the precision of field measurements difficult to assess. Here we demonstrate an analysis of dyke aperture that incorporates the outcrop geometry into the aperture measurement. This allows for an exceptionally high density of measurements to be made along the length of a single dyke. A result from a single dyke is provided here to illustrate the technique. A larger dataset encompassing a number of dykes and analysis of the results is currently in preparation.

2.3.2.1 Extraction of dyke aperture data from non-uniform outcrop surfaces

Any dyke whose orientation is not orthogonal to its outcrop surface has an apparent aperture that is not its true aperture, and a collection of measurements are required to obtain the true aperture. As soon as the outcrop is rough and irregular from one wall of the dyke to another it introduces further complications, relative to obtaining true aperture from planar outcrops. At each location where true aperture is extracted, the required outcrop measurements are: 1) orientation of the dyke; 2) apparent dyke aperture (cf. Compton, 1962); 3) orientation of the outcrop surface. The relationship of these measurements to true aperture at a single observation point along a dyke is illustrated in Figure 8a-b. In the field it is time-consuming to make such measurements accurately on irregularly shaped outcrop surfaces and often it is impossible to reach all the outcrop. Indeed, a field geologist might elect not to measure curving or irregularly shaped outcrop surfaces altogether in order to avoid producing a spurious measurement. The exception are dykes that intersect planar outcrop surfaces, where measurement of aperture is a relatively straightforward operation. In contrast, by extracting structural data from dense point clouds that account for outcrop surface geometry, it is possible to make many more measurements than is feasible by hand in the field (e.g. at cm-level intervals) and begin to tease out the subtle information preserved in dyke aperture.

Dense point clouds that accurately reproduce outcrop surfaces enable 3D aperture calculations using alternative methods to those illustrated in Figure 8a-b. First, the trace of each dyke wall is digitised using the CloudCompare plugin Compass (Thiele et al., 2017a). A plane that represents the average dyke orientation is derived from the best fit planes for opposing dyke walls and is referred to here as the *reference plane* (Fig. 8c). The aperture measurement is then made in 3D by first converting the reference plane to a dense array of points with 0.5 mm spacing and then measuring the distance to each dyke wall trace using the cloud-to-cloud comparison plugin, M3C2 (Lague et al., 2013). For a reference plane lying between opposing dyke walls, the aperture of the dyke is simply the sum of the distance to each wall at

the same position along strike. Such aperture measurements can be made at regular, prescribed intervals, along the full extent of dyke exposure. In practise, dyke traces are typically segmented due to a combination of emplacement-related step-overs, post-emplacement faulting, and areas of covered outcrop. Our method assumes that the orientations of the two dyke walls involved in each measurement are not significantly different. For a dyke segment with near-parallel walls, it is sufficient to assign a single reference plane to the entire segment. In the case of a more geometrically complex dyke (i.e. characterised by sharp changes in strike or dip) a single plane may only be representative of the dyke orientation over a short distance, thus requiring many more reference planes.

An important second step is to assess the accuracy of this method by imposing a synthetic dyke with a fixed aperture (e.g. 1 m) on the same point cloud model, with similar orientation to the dykes being measured. The aperture of the synthetic dyke is then quantified across the outcrop using the method described above (Fig. 8c) and a mean aperture and standard deviation are derived and compared to the real aperture. In this way, measurements of the synthetic dyke with known aperture and orientation provide a confidence estimate that is specific to the point cloud being analysed. This method both verifies the accuracy of the point cloud and is used to assign a confidence limit that can be applied to real dykes of similar dimensions and orientation within the same model.

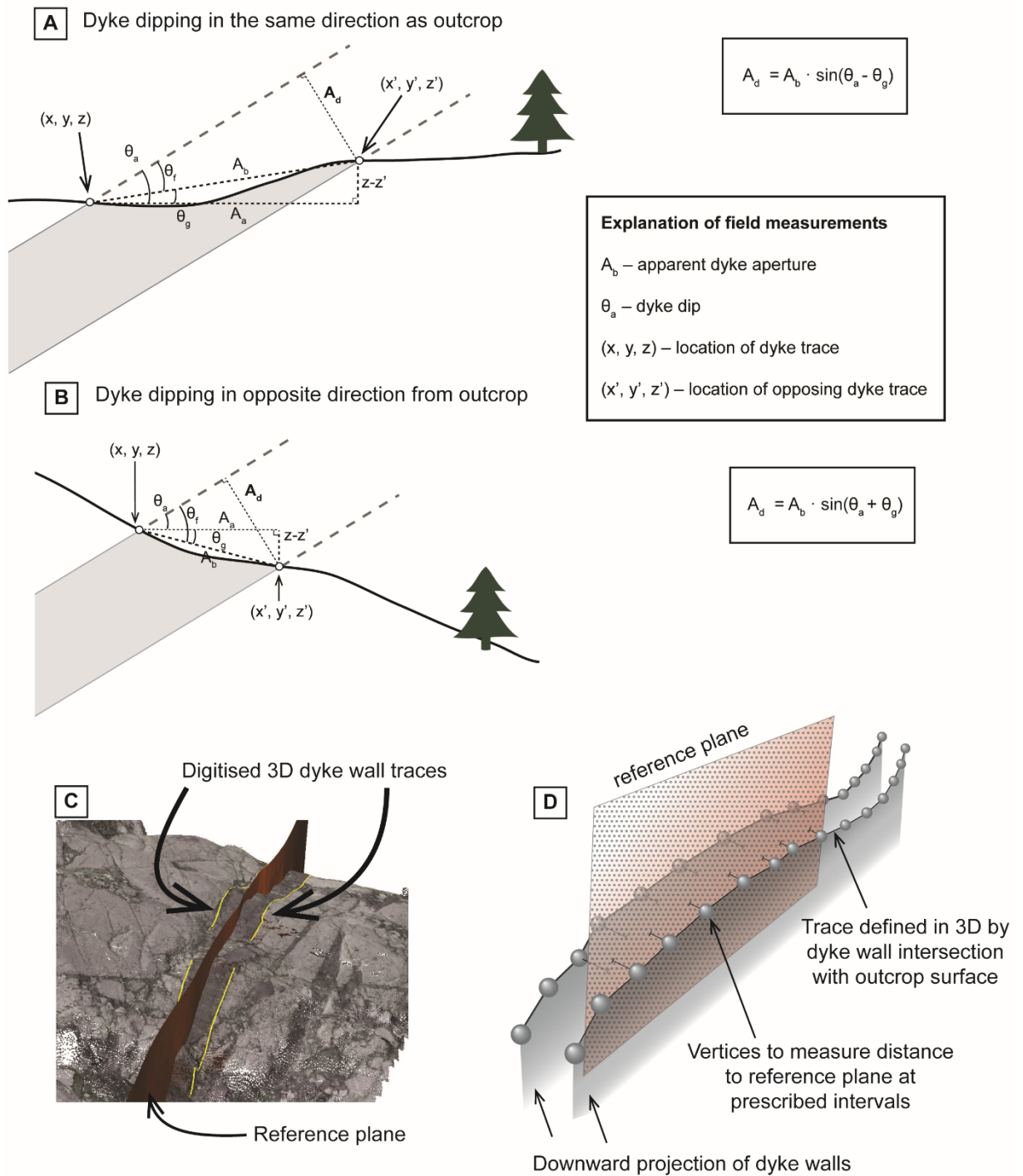


Figure 8 True dyke aperture derived by various methods. (a) Field measurements made on an outcrop dipping the same direction as the dyke; (b) Field measurements made on an outcrop dipping the opposite direction as the dyke; (c) a dense point cloud outcrop reconstruction of an andesite dyke (dark grey) in granodiorite (light grey) with a reference plane imposed in the approximate centre of the dyke. (d) schematic illustration of aperture measurements made using opposing 3D dyke wall traces to a reference plane.

2.3.2.2 Aperture result from an andesite dyke, Sierra Nevada, eastern California

We illustrate the 3D aperture measurement method using data from the Independence Dyke Swarm of eastern California. The dyke swarm extends ~600 km from the Mojave Desert to the central Sierra Nevada, and is a major feature of the Mesozoic Cordilleran magmatic arc (Hopson, 1988). The case study shown here is from a well exposed outcrop in an alpine environment where uplift and erosion combined with Pleistocene glacial denudation has revealed dykes in 3D relief. Within the central Sierra Nevada, the dykes are mainly calc-alkaline gabbros and diorites emplaced into granodiorite plutons of Jurassic age (Chen and Moore, 1979). The depth of emplacement is estimated to be 10-11 km, based on Al-Hornblende geobarometry from nearby plutonic host rocks (Ague and Brimhall, 1988; Mahan et al, 2003). Consistent isotopic composition of mafic dykes throughout the swarm suggests a shared lithospheric source and has led previous workers to propose magma transport was mainly vertical from a relatively homogenous magma reservoir (Glazner et al., 2008). Despite the very broad footprint of the swarm, the maximum aperture of individual dykes is typically between 0.1 and 5 m (Glazner et al., 2008). The lengths of dyke segments that comprise the swarm are typically from tens of metres up to a few kilometres, but this is less well constrained because exposure is discontinuous along strike.

High density aperture data was measured along the strike of a single dyke from the Independence Dyke Swarm. The length over which the dyke is exposed is 95 m, with an average aperture of 1.42 m. In order to check which aperture variations are reliable, a synthetic dyke was imposed upon the model with a 1 m aperture and a dip of 60°. Measurements taken where the angle between the outcrop surface and the synthetic dyke were between 60° and 115°, yielded a mean result of 99.3 cm ($n=835$) with a standard deviation of 0.014 cm (Fig. 9). For outcrop surfaces with angles < 60° and > 115° to the synthetic dyke, the mean aperture result is 95 cm with a standard deviation of 2 cm. Overall, the method tends to underestimate the dyke aperture, with a systematic decrease in accuracy associated with low angles (i.e. both very oblique and very acute angles, Fig. 9) between outcrop and dyke dip. As a result, although aperture measurements with errors of up to 7 cm are not unreasonable, we chose to use measurements taken where the dyke-outcrop angle lay between 60° and 115° for digital aperture measurements of the real dyke. Based on this confidence limit, aperture measurements were made at 10 cm intervals (Fig 10 a). Using this method we were able to collect aperture measurements ($n=298$) over a cumulative 30 m of the dyke length, with gaps in the data as a result of small faults and covered areas (Fig. 10 b). Though neither tip of the segment is exposed, the intervals indicate that the dyke possibly tapers toward the exposure limit in both directions. A maximum aperture of 1.75 m was measured near the middle of the section. Importantly, the data further reveal previously unobserved, subtle aperture variations of up to 20% over wavelengths of a few meters, where the amplitude of the variations are much larger than the errors quantified using the synthetic dyke. The variation in aperture, which occurs over the entire observable length of the dyke, potentially reveals important insights into dyke linkage and propagation,

which will be explored in a future publication. For the purposes of this review, the method demonstrates the quantity and quality of data that can be extracted from digital outcrop models.

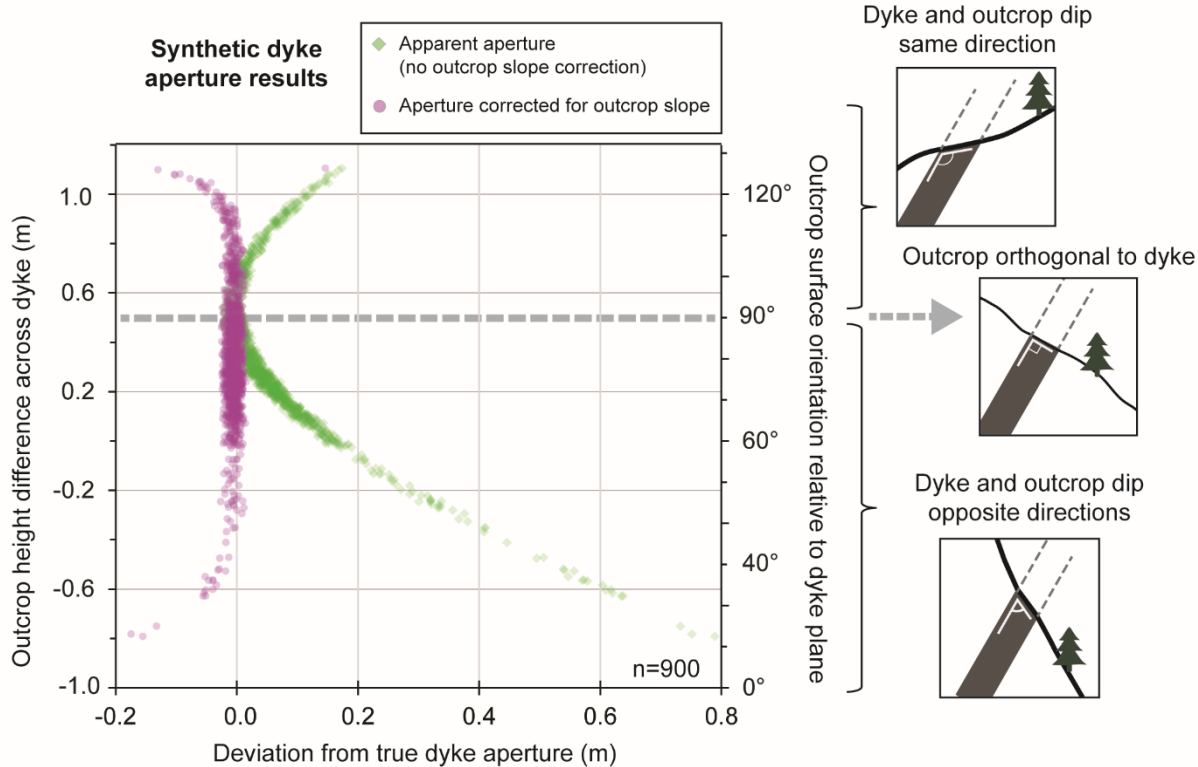


Figure 9 Results of 900 digital aperture measurements for the Sierra Nevada dense point cloud derived from a synthetic dyke of fixed width (1 m), dipping 60° . Aperture corrected for outcrop slope are accurate over a wide range of outcrop dips (plotted on vertical axis at right) are given with respect to the dyke orientation, such that 90° is perpendicular to dyke dip. True aperture measurements (purple circles) are very accurate over a wide range of outcrop dips ($60^\circ - 115^\circ$). For comparison, the same data are plotted without incorporating outcrop orientation (green diamonds) and yield accurate results over a much narrower range of outcrop orientations ($85^\circ - 95^\circ$).

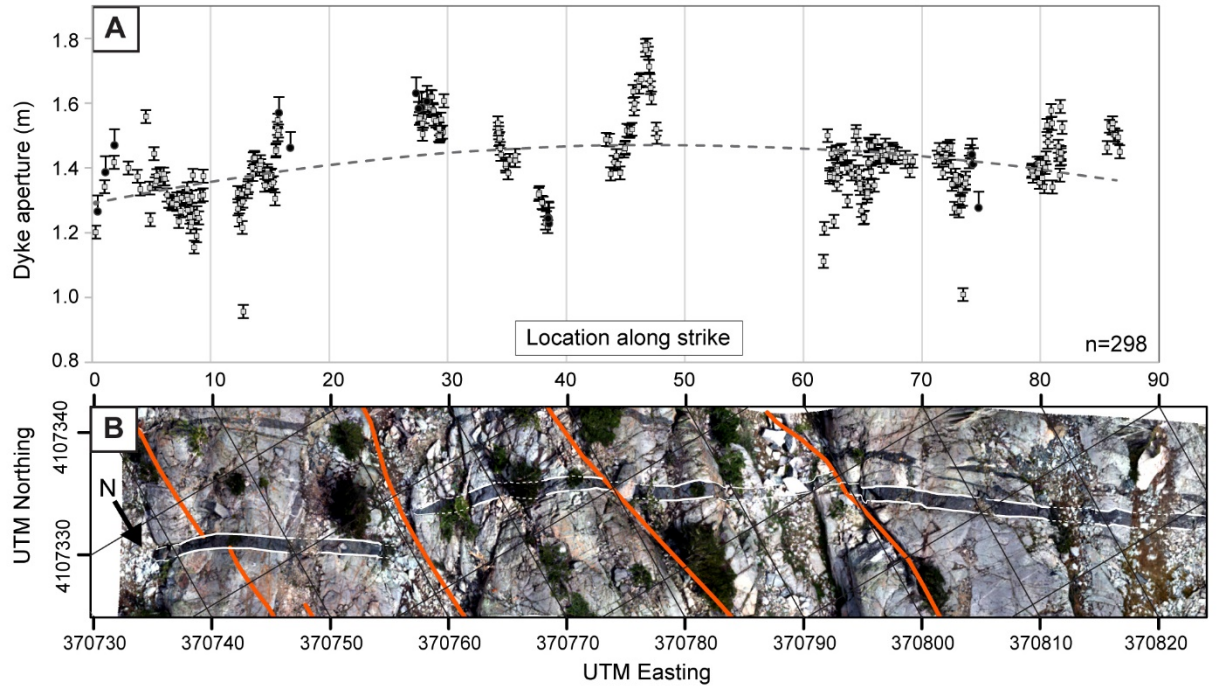


Figure 10 Aperture results for a single dyke from the Independence Dyke Swarm, eastern California, derived from measurement of a 3D dense point cloud. (a) Aperture exhibits variation of up to 20% over distances of up to several metres. Higher quality measurements (open circles) have smaller associated error. Data with higher error that systematically under sample true aperture (black circles) are also shown but represent only 5% of the total results. The first-order geometry of the dyke is described by an ordinary least squares regression (dashed line) fit to the high precision data yields tapered profile that is broadly symmetrical around a maximum of 1.4 m. The data also exhibit a pronounced second-order aperture oscillation. (b) Orthoimage of the studied dyke. The trace of the dyke walls is mapped where well exposed (solid lines). Faults (red lines) mainly cross-cut the dyke, resulting in minor offsets.

2.3.3 Example of subtle lithologic control on dyke geometry

Wave cut rock platforms at Bingie Bingie Point expose a swarm of centimetre to metre wide Cretaceous to Paleogene dolerite and dacite dykes that intrude Devonian aplites, tonalities and gabbrodiorites of the Bingie Bingie Suite (Fig 11). Spectacular magmatic mingling textures and complex sets of veins and joints are also well exposed, which makes it a popular undergraduate field trip location for a number of Australian universities.

A 1 cm resolution orthophotograph and a 2 cm resolution DEM were generated by applying a SfM-MVS workflow to a series of highly overlapping aerial photographs captured by a remotely controlled UAV (Table 2). The survey design (e.g., flight height, horizontal speed, flight line spacing, camera aperture, ISO, shutter speed and shutter interval) was optimised in advance to minimise motion blur and to guarantee a 1 cm resolution orthophotograph (Vollgger & Cruden, 2018). Prior to the acquisition of aerial photographs by UAV, 9 markers were distributed within the area of interest and surveyed using a dual frequency ProMark 500 RTK GPS device with an accuracy of 1-4 cm. Agisoft Photoscan Pro version 1.2.6 was then used to reconstruct the outcrop geometry using 7 GCPs as control points and 2 GCPs as check points in order to produce a geo-referenced data set with total root mean square error of 2.4 cm.

Structural data (e.g., fracture and vein orientation data, intrusive contacts) were semi-automatically extracted from the dense point cloud using the CloudCompare Compass plugin of Thiele et al. (2017b). The orthomosaic derived from the point cloud the lithological contacts to be delineated using conventional Geographic Information System (GIS) tools. The resulting detailed map and orientation data were acquired in a fraction of the time and with higher fidelity compared to traditional field-based techniques. Moreover, we were able to identify subtle lithological/compositional differences that would not have been identified in the field, as the high-resolution orthomosaic allowed rapid viewing of the outcrop at multiple scales and from different perspectives and scales.

This digital mapping and structural analysis demonstrate that the dykes trend 063° , parallel to a major set of joints in the country rock that likely formed contemporaneously with syn-emplacement extension. Subsidiary joint sets trend NNW-SSE, sub-perpendicular to the dykes, N-S and E-W. The dykes display considerable structural complexity such as broken bridges, steps and apophyses (Fig. 11). Significantly, our mapping suggests that dolerite dyke steps occur where dykes crosscut country rock contacts but the dacite dyke steps are not influenced by the lithological changes to the same degree (Fig. 11). In the field this was not very evident because the tonalite-diorite contact was difficult to distinguish. In contrast, the orthomosaic indicates dyke deflections step up towards the N and are associated with concentrations of xenocrysts and xenoliths on their NE sides. Elliptical mafic microgranular enclaves, and magma mingling and magmatic textures are clearly visible in the tonalities and diorites,

demonstrating the utility of UAV-based orthomosaics for mapping internal magmatic textures (not just geometries) over large surface areas.

	Survey detail	Albany	Bingie Bingie	Sierra Nevada
Camera	Image dimensions (pixels)	4928 x 3261	6000 x 4000	4928 x 3261
	Focal Length (mm)	18	16	18
	Lens type	prime	prime	prime
	Sensor type	APS-C (Pentax)	APS-C (Sony)	APS-C (Pentax)
	Sensor dimensions (mm)	23.7 x 15.7	23.7 x 15.7	23.7 x 15.7
	Camera model	Ricoh GR	Sony Nex	Ricoh GR
Survey plan	Nominal altitude above ground (m)	9	50	12
	Area (sq m)	13,000	30,800	8,100
	Image count	1100	297	826
	Camera orientation	nadir	nadir	nadir
	Flight pattern	grid	grid	grid
	Side overlap %	30	85	40
	Front overlap %	50	85	50
	Ground control point (count)	30	9	28
Photogrammetric outputs	Dense point cloud (millions of points)	20	86	27
	Tie point count	77,853	109,601	137,153
Error protocol	GCP survey tool	Total station	RTK-GPS	RTX-GPS
	GCP survey accuracy (cm)	1 - 4	1 - 4	2
	Control point RMSE (cm)	5	2.4	5.5

Table 2 UAV photogrammetry survey and model metrics for the case studies in Section 2.2.4. The specifications and results summarised here are necessary to understand the level of detail and accuracy of UAV photogrammetry projects. Including this information provides credence to research outcomes by enabling robust comparison and reproducibility.

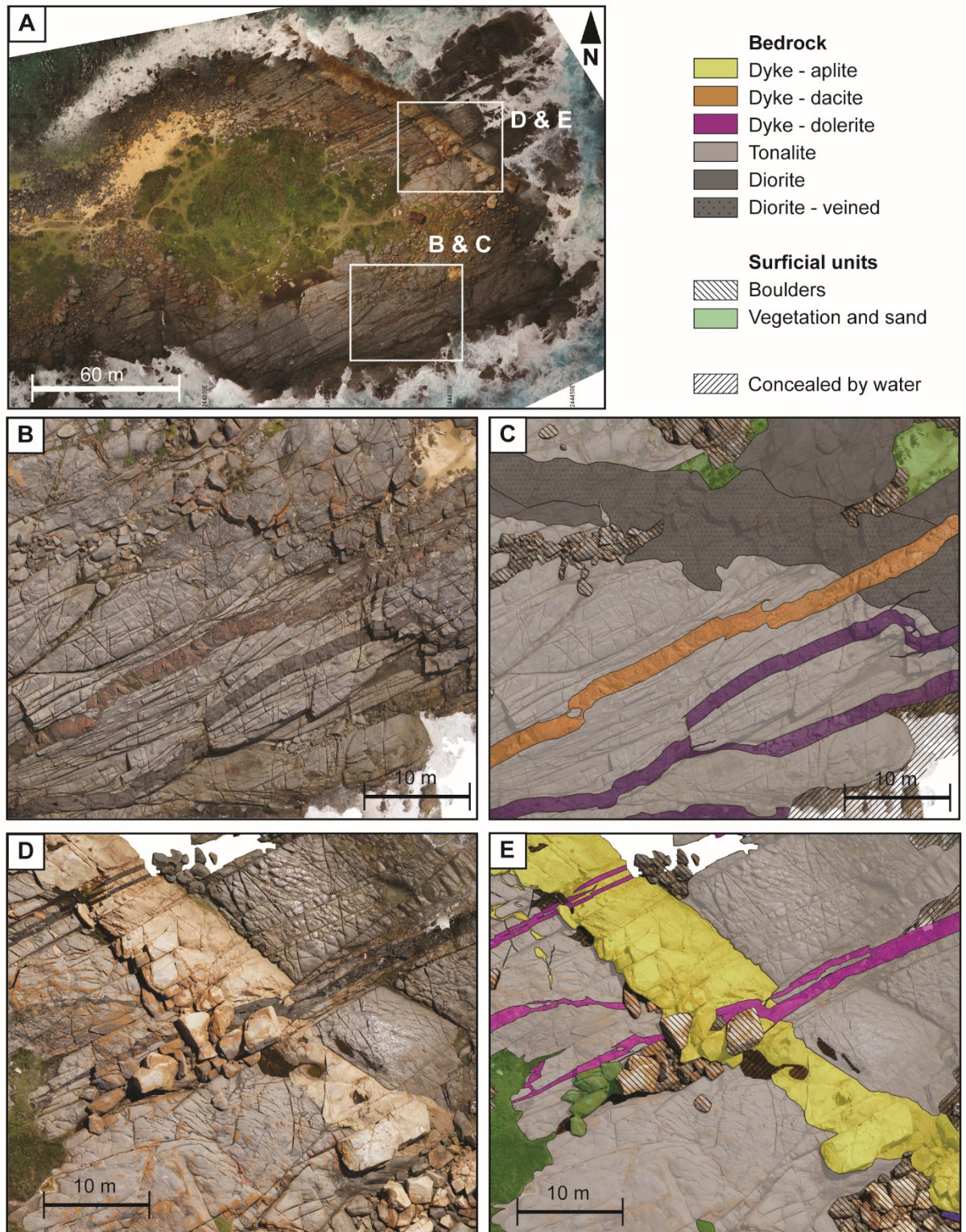


Figure 11 Orthoimages and detailed geologic maps from Bingie Bingie Point, NSW Australia show interaction of late NE-striking dykes with older igneous rocks. (a) Orthoimage of the study area derived from photogrammetric model. Modified from Vollgger et al. (2018). UAV survey and model metrics are in Table 2. (b) Detailed area of dacite and mafic dyke intrusion. Subtle differences in host rock composition correspond with subtle colour differences. (c) Geological map of the outcrop in (b), showing the location of dyke step-overs with respect to changes in host rock composition. (d) Step-overs in the NE-striking mafic dykes appears to be related to a mechanical contrast in the host rock, resulting from emplacement of an older NW-striking felsic dyke. (e) Geological map of the outcrop in (d).

2.3.4 Summary

In summary, the outcomes of these case studies show the advantages of the systematic documentation of the 3D geometry and textures of dyke networks that is now possible with a resolution, accuracy, and continuity of measurement not previously attainable with conventional field techniques. The richness of these datasets requires new digital analysis tools to obtain full value from the data in a timely manner. In Section 2.2.4 we outline some analytical tools now available and document the development of geophysical and other sensor types in addition to digital cameras.

2.4 Emerging techniques and technologies

2.4.1 Sensors

So far, this review has been concerned with UAV-based photogrammetry as a research tool for analysing outcrop exposures of ancient dyke systems. However, the application of other remote sensing and geophysical sensors alongside photogrammetry, is potentially also a significant benefit to the Earth Sciences. In this section we briefly touch on these, and how they could be applied to study intrusions in both outcrop and active volcanic systems.

In active volcanic systems, numerous studies have demonstrated the value of differential interferometric synthetic aperture radar (InSAR) as a geodetic tool for the accurate measurement of ground displacements in the order of millimetres to centimetres (c.f. references in Fernández et al., 2017; Ebmeier et al., 2018). Because InSAR is a satellite-based radar technique it is capable of capturing time-series data across tens of kilometres surface area, revealing vertical changes, which provide insight into subsurface magma movement from reservoirs and through dykes (e.g. Pagli et al., 2012; Wauthier et al. 2015). However, the GSD of typical InSAR measurements is in the order of meters to tens of meters and revisit times are generally several days (Casagli et al., 2017). A further complication is that atmospheric water content negatively impacts upon radar signals, making it difficult to extract meaningful displacement measurements under some conditions. Opportunities therefore exist to apply micro-UAVs to complement InSAR surveys (Sparks et al., 2012), filling the scale-gap between ground and satellite observations by providing higher spatial resolutions (mm – cm GSD) over areas of specific focus within an InSAR survey, and potentially allow more frequent revisit times (hourly to daily).

An immediate and obvious complementary application of UAVs would be to map the near surface grabens and fissure systems that form above shallow dyke intrusions (e.g. Hjartardóttir et al., 2016) and to track near-field displacements using the same time-series techniques developed for UAV monitoring of landslides, glaciers and lava flows (Niethammer et al., 2012; Immerzeel et al., 2014; Carr et al., 2018). Potentially both photogrammetry and emerging micro-UAV based light detection and ranging (UAV-LIDAR; Wallace et al., 2012) techniques are suitable, with LIDAR having significant advantage over photogrammetric approaches when the landscape is covered by vegetation. High resolution maps of the

near surface faults and fractures developing above a dyke will be easily achieved. However, surveys designed to track near-field ground displacements are likely to be affected by the fact that dyke-related ground displacements occur across large distances. Time-series surveys of this type rely on calculating displacement relative to a fixed reference frame, and therefore GCPs will not be appropriate to use because they are likely to be affected by long-wavelength ground motions. In this case, UAVs with onboard RTK GPS or post-processing of GPS data are required.

In addition to LIDAR or photogrammetry, UAVs have an emerging but important capability to conduct geophysical and beyond-visible remote sensing surveys. These include amongst other things thermal infrared, hyperspectral and aeromagnetic capabilities (Funaki et al., 2014; Jakob et al., 2017; Thiele et al., 2017a), but we are yet to realise the application of such sensors from UAVs to the study of intrusive systems.

Magnetometers have been mounted on large fixed wing UAVs for some time (e.g. Funaki et al., 2014) which typically require a clear area to land. However, flux gate aeromagnetic capabilities are now available that can be mounted on multirotor UAVs (e.g. Ameglio et al., 2015) and systems are beginning to emerge, adapted for in-expensive off-the-shelf platforms. Cost effective multirotor UAV-Mag is attractive for high resolution mapping of dyke networks in the subsurface, or where outcrop is limited, both in active and ancient settings. The ability for UAV-Mag to differentiate between dykes of different magnetic remanent properties will be potentially useful for understanding the evolution of intrusive systems. The utility of such instruments is perhaps most evident in the subsurface mapping of dyke networks in volcanic environments where topography can change dramatically, because multirotor UAVs can closely follow topography, which minimises error associated with terrain correction (Dentith and Mudge, 2014). The close line spacing, shorter above-ground levels and stable slow flight velocities that multirotor UAVs can achieve in particular provide a resolution and human safety advantage over conventional aerial surveys. In addition, future deployments of an array or swarm of drones with magnetometers will lead to the potential for adaptive surveys and the ability to return gradiometric data with inexpensive equipment.

Possibly the most important sensor development is the miniaturisation of infrared hyperspectral cameras (Hruska et al., 2012), which have the potential to reveal beyond-visible information about different dyke compositions, alteration or chemical interactions with wall rock, as well as a link between ground and satellite-based hyperspectral surveys (c.f. Jackisch et al., 2018). Sensors are now available in the near infrared (NIR), shortwave infrared (SWIR) and longwave infrared (LWIR) ranges. This technology has been transformative for environmental and agricultural studies. Nonetheless, the processing of hyperspectral data for geological information is far from trivial and corrections are required for sensor distortions, reflectance, atmosphere, high signal-to-noise ratios and topography (Jacob et al., 2017). In the SWIR range, typically used to detect mica and clay content, the cameras are yet to achieve

the spectral resolution necessary to be able to quantify mineral chemistry from the imagery, though they should reveal bulk differences in rocks not detectable in the visible spectrum that are related to composition and texture. A further complication is that cameras capture data by either line-scans or image frames, and line-scan data is affected by the pitch, yaw and roll of the UAV. Line-scan sensors therefore require a sensitive Inertial Measurement Unit (IMU) and ideally ground-control points to aid with corrections. In all cases, ground-truth spectroscopy is recommended to validate results (Jackisch et al., 2018).

2.4.2. Digital outcrop analysis

The extraction and analysis of features, orientations and field relations from UAV acquired imagery is a time-consuming process, often severely restricting the amount of information that can be obtained. These limitations result from: (1) practical considerations when extracting large numbers of measurements from unclassified point-cloud or orthophoto datasets, and; (2) the limited ability of established analytical techniques incorporate the high data density, coverage and dimensionality of the results. Significant research effort in this area is still required to take full advantage of the high-resolution and rapid-acquisition that UAV surveys allow. In the following section we review a few emerging techniques that help tackle these issues.

2.4.2.1. Automated and semi-automated fracture and lithology mapping

A variety of approaches have been developed for efficiently extracting features and structural measurements from UAV derived data. These can be divided into two categories, those that operate on point-clouds and those that work with 2.5D orthomosaic and DEM datasets (Fig. 12c).

Point cloud techniques have become popular in the geotechnical community, where region-growing or clustering algorithms are commonly used to extract planar patches (facets) from photogrammetric and laser-scan data (e.g. Dewez et al., 2016; Lato and Vöge 2012; García-Sellés et al., 2011). The orientation of these facets can then be used to characterise joint characteristics and infer bulk rock-mass properties (García-Sellés et al., 2011). A key assumption of facet-based techniques is that the features of interest correspond directly with surface geometry. Different approaches are required when the features of interest do not strongly influence outcrop geometry or are oriented unfavourably (with respect to the outcrop surface) for direct-exposure. In these situations, it is instead necessary to measure the intersection trace between features (fractures, faults, contacts) and the outcrop surface. This is typically achieved by manual tracing on an orthomosaic in a GIS and extracting associated elevation information from a high-resolution DEM (e.g. Townsend et al., 2015; Dering et al., 2016). Several automated and semi-automated approaches have also been developed to improve the efficiency and objectivity of this task (Vasuki et al., 2014; Seers and Hodgetts, 2016a; Thiele et al., 2017a) by adopting edge-enhancement and detection techniques (e.g. local intensity gradient, phase-congruency) from

computer vision research (Fig. 12). Seers and Hodgetts, (2016a) provide a fully automated method in which feature edges are extracted using a series of thresholds. Other methods adopt a computer-assisted approach in which an initial manual interpretation is automatically refined (Vasuki et al., 2014). Because these two approaches involve a degree of automated feature mapping, it can be argued that the resulting maps are less subjective. An alternative approach, implemented with the Compass plugin of CloudCompare and GeoTrace plugin of QGIS, uses a least-cost path solver to track feature boundaries between manually defined control points (Fig. 12) (Thiele et al., 2017a). This approach enables finer user control of the interpretation process.

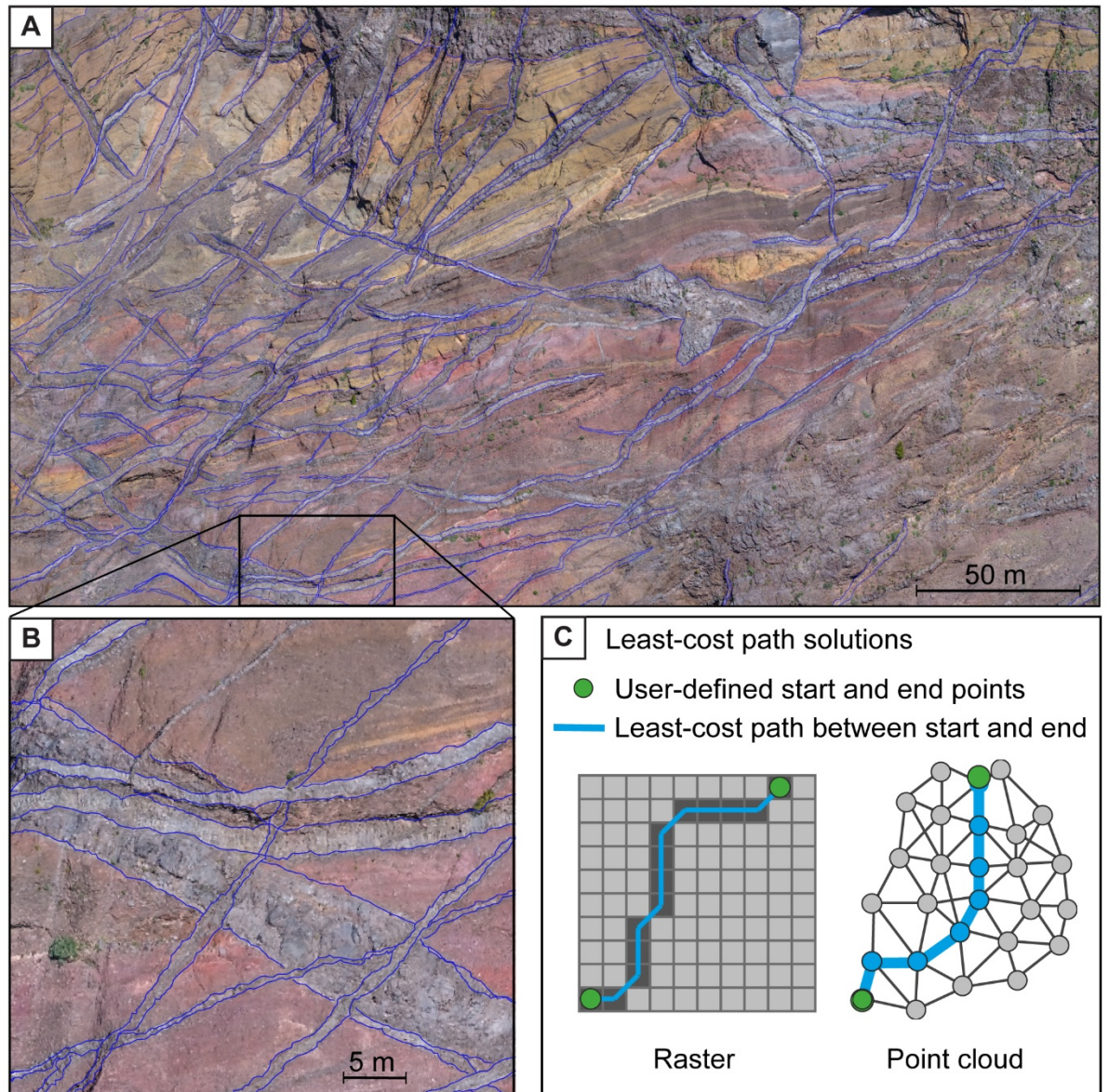


Figure 12 Example of dykes mapped at centimetre scale over distances of hundreds of meters using the semi-automatic least-cost path approach described in Thiele et al., 2017. (a) Multiple generations of mafic dykes exposed in a sub-vertical cliff within Caldera Taburiente (Canary Islands) that were otherwise completely inaccessible. Dyke margins (blue lines) were mapped with a least-cost algorithm paired with a cost function that causes traces to follow areas of large point-brightness gradient, and so picks out the color contrast between dark dykes and the brighter pyroclastic and scoria host rocks. (b) Higher resolution view which highlights the cross-cutting relations and mechanical interactions between different dykes as captured by mapping at cm resolution. (c) Schematic representation of the least-cost path algorithm for detection of dyke edges in a 2D raster dataset (lower) and 3D point cloud dataset (upper). The examples in (a) and (b) were interpreted directly on the dense point cloud.

2.4.2.2. *Structural analysis techniques*

The often-overwhelming detail captured in UAV surveys and the dimensionality of extracted 2.5D or 3D surface or trace data present significant challenges during analysis. Unlike spot-orientations provided by traditional compass-clino methods, facet or trace data extracted from virtual outcrop models can capture the geometry and orientation of a structure across large areas. Although potentially superior in accuracy to spot-orientations (as orientation can be averaged over larger areas), special methods are required to describe structure-geometry from these datasets. Several of these are briefly described in the following section, and their limitations and possible future developments discussed.

Many studies estimate structure orientation by fitting a plane to individual facets or structural traces, and then analyse the results using stereographic methods (e.g. García-Sellés et al., 2011; Thiele et al., 2015; Dering et al., 2016). This technique can be readily applied to facets, where the typically large and co-planar spread of points produces robust estimates for structure orientation (e.g. Fernández, 2005). Structural traces, however, require a little more care as: (1) points along the trace may be co-linear if outcrop geometry is flat; (2) small variations in structure orientation or outlier points can result in the trace being co-planar with the outcrop-surface rather than the structure of interest, and; (3) structures such as faults, fractures and contacts tend not to be perfectly planar over large areas, resulting in scale-dependent orientation estimates.

A variety of software packages are now available for extracting traces and facets from 3D point cloud and textured mesh datasets, including VRGS (Hodgetts et al., 2007), OpenPlot (Tavani et al., 2011), Lime (Buckley et al., 2017) and CloudCompare (cf. Dewez et al., 2016; Thiele et al., 2017a), although for applications involving largely flat outcrops a conventional GIS workflow is sufficient. Algorithms such as least-squares best fit, eigenvector analysis, or random sample and consensus are then typically used to estimate best-fit-planes and hence structural orientations (Fernández, 2005; García-Sellés et al., 2011; Roncella and Forlani, 2005, Thiele et al., 2015). For the set of vertices that define a structural trace, the relative magnitudes of the second and third eigenvalues of the covariance matrix can be used to eliminate highly inaccurate orientation estimates that result from co-linear traces (Fernández, 2005; Thiele et al., 2015). Seers and Hodgetts (2016b) develop a Bayesian framework for the estimation of structural orientation from trace datasets. This technique uses the spread of points along a trace to constrain the rotational degrees-of-freedom of the best fit plane, and hence uncertainty, in the strike and dip directions based on the 3D information contained in the outcrop. For example, a trace defined on a completely planar, horizontal outcrop would yield a well-constrained strike but a dip that is unconstrained and hence highly uncertain.

Finally, the ability of photogrammetric surveys to capture facet and trace geometry over large areas often results in a situation where a single best-fit-plane is no longer a useful description of structure geometry, especially where structures contain steps, segments or large-scale curvatures. While planes

can instead be fitted to subsets of the overall dataset, the results will vary with scale, outcrop geometry and the subjective choice of segment boundaries. Hence, we suggest that to take full advantage of the geometric detail that photogrammetric surveys provide, best-fit-planes are overly simple and more advanced methods for characterising and extrapolating structure geometry are required. Recent developments in 3D implicit modelling, specifically the adaptation of algorithms such as radial-basis and discrete-smooth interpolators for geological applications, provide promising avenues for doing so.

2.5 Discussion

This review has mainly concentrated on the application of UAV-based technology to dykes emplaced into plutonic country rocks that lie at middle to shallow crustal levels. In this discussion we summarise the key points emerging from the case studies and the minimum parameters that need to be reported in any photogrammetric study, so that the quality of model data can be properly assessed. We also highlight broader application of the technology to understand shallow subvolcanic processes and point to the value of the data for educational purposes.

2.5.1 UAV technologies as a step-change in field observation

The case studies in section 2.3 demonstrate that the mapping and quantification of dyke geometries, dyke-related fracture networks, and internal textures, are made possible by analysis of digital models acquired by UAV. Moreover, recent advances in digital mapping tools allow for the rapid and systematic measurement of dyke structure in 3D that is otherwise difficult to capture using conventional field techniques. Indeed, complex outcrop geometries that might have posed a challenge to systematic measurement in the field are now an asset in the context of digital outcrop analysis. The following key points emerge:

1. UAV-based photogrammetry generates models that are useful for multi-scale analysis not easily achieved using traditional field techniques.
2. Multi-scale analysis enables broad wavelength patterns to be identified even when the features contributing to those patterns are fine scale, on the order of millimetres. In the case of the Albany data, fractures with apertures of ~4 mm were shown to increase in density in association with a dyke swarm, distinguished amidst the presence of a background fracture population that introduced significant noise into the data.
3. Multiple angles of intersection yield a more complete 3D sampling of a geological feature. This property provides increased confidence when fitting planes to data to extract orientation information or other characteristics.
4. Dyke characteristics can be measured rapidly and at a resolution that is not practical in the field. In the case study of the Independence Dyke swarm we introduced a method that more accurately measured aperture than traditional techniques and was used to capture aperture data every 10 cm continuously along a dyke, over several hundred metres.

5. Dyke textures and subtle host rock features emerge from UAV-based imagery and photogrammetric models, some of which are not readily evident on the ground. In the case of the Bingie-Bingie dataset, dolerite dyke appear to develop geometric steps in association with a compositional boundary that was not easily distinguished on the ground. Internal dyke textures were also documented over large surface areas. In the Independence dyke swarm, chill margins were mappable and in principle their dimensions quantifiable over many hundreds of metres.

The quantity and quality of data available using the techniques documented in this review, demonstrate that they are now research tools that go beyond qualitative visualisation and that we can measure features over length-scales and at resolutions not previously achievable. As a result UAV-based techniques are set to provide a step-change in field observations and enable us to address many outstanding scientific questions in volcanology. Alternative drone-based sensors, in addition to digital cameras, further extend our capabilities in this regard but remain underutilized. Most immediately these include aeromagnetic and hyperspectral surveys.

2.5.2 Summary of survey quality reporting

It is essential to understand and report the quality of photogrammetric data being used for high precision outcrop measurements. The accuracy of structural analysis derived from photogrammetric models has previously been found to be comparable to 3D datasets generated by laser scanning (Favalli et al., 2012; Thiele et al., 2015, Smith et al., 2016). As UAVs become increasingly used in Earth Science, it is important that practitioners follow best practice and report a standard set of metrics so that the accuracy and resolution of the photogrammetric output can be clearly understood. Suitable error reporting enables researchers to attach confidence limits to the results. Table 2 outlines the essential metrics that we recommend should be reported alongside the results of the three case studies described here.

2.5.3 Insights into broader volcanic processes using UAV-photogrammetry datasets

UAV-based studies employing photogrammetry or other types of remote sensing have immediate application to research on subvolcanic settings and shallow volcanic processes. The geometry and distribution of subvolcanic intrusions reflect the stress state around eruption sites, and hence maps of dyke-orientation have been used to gain insight into volcano-tectonic processes (e.g. Tibaldi et al., 2010; Famin et al., 2017) and flank instabilities (e.g. Delcamp et al., 2012; Berthod et al., 2016). Shallowly emplaced dykes have also been related to landforms such as eruptive fissures to explore the changes in stress associated with active magma chambers (e.g. Browning et al., 2015) and variations in topography (e.g. McGuire and Pullen 1989, Jenness and Clifton 2009). The insights gained from each of these studies could further advanced by achieving the high resolution data over large areas now possible through UAV-based technologies.

At a smaller scale, textural and morphological features preserved within and around shallow intrusions can provide important insights into eruptive processes such as vesiculation, fragmentation, and magma withdrawal. Geshi and Oikawa (2014), for example, mapped the abundance of lithic fragments within feeder dykes exposed in the caldera wall on Miyakejima volcano. By analysing telephoto images of near-vertical exposures with a resolution of approximately 3 cm/pixel, it was possible to correlate the intra-dyke textures with associated eruptive products and styles. Similarly, textural facies on the margins of a feeder-dyke from the Tongariro volcanic field (New Zealand) were documented by Wadsworth et al. (2015) which record magma flow directions during a Strombolian eruptive period and subsequent magma drainback. Key features were described at the outcrop scale, which included ductile shear fabrics, flow folds, autobrecciated margins, and the size distributions of phenocrysts, xenocrysts and vesicles. Wadsworth et al. (2015) document a striking feature that has geometry that resists reduction inherent in conventional field measurements. Although these examples successfully utilised traditional field methods, the integration of UAV-SfM workflows should help gain further valuable insight into subvolcanic processes by providing easy-access to large areas of outcrop and extremely high-resolution quantitative textural and geometrical information.

2.5.4 Educational value

Beyond the research applications outlined in this paper, UAV photogrammetry has immediate educational value for training geoscience students. The proliferation of tablets and other digital tools has been predicted to shift field education toward learning that is driven by hypothesis testing and makes use of pre-existing datasets (McCaffrey et al., 2005), because the map-making process becomes more efficient and consequently there more emphasis on idea generation. The ultrahigh resolution images generated from UAV photogrammetry data are no longer confined to large format paper maps and are ideal for use within a GIS. In addition, in the classroom it is possible to import this data to digital globes (e.g. GoogleEarth), providing a training tool that is richer and more immersive than other available imagery. National digital outcrop libraries already exist in Australia (<http://www.ausgeol.org>) and the UK (<https://www.e-rock.co.uk>; Cawood and Bond, 2018) that are well suited to host 3D scene reconstructions for instructional use. Models available for download from these websites can be viewed using online platforms such as Sketchfab (<https://sketchfab.com>), enabling interaction in 3D and annotation of existing models.

Relevant to the case studies presented here, orthomosaic from the Bingie Bingie locality have been used for undergraduate field exercises by various Australian Universities (freely available here: https://figshare.com/articles/Bingie_Bingie_NSW_orthophotograph_basemap_A3/5950303). Course instructors noted that students could better correlate outcrop observations with map-scale features visible in the orthomosaic and thus were more confident to draw structures on field sheets. As a result, students were more engaged with the task and more independent in their learning. When it comes to grid mapping

techniques, this high resolution type of imagery is irreplaceable. We acknowledge that providing students with such high resolution imagery represents an exceptional field mapping experience that reduces some challenges such as locating oneself on a map sheet or deciphering map-scale structures. On the other hand, using such imagery, we have found that students are able to connect outcrop observations with geological context more readily, accelerating learning outcomes.

2.6 Conclusion

- 1) The quantity and quality of data available using the techniques documented in this review, demonstrate that they are now research tools that go beyond qualitative visualisation and that we can measure features over length-scales and at resolutions not previously achievable. As a result, UAV-based techniques are set to provide a step-change in field observations and enable us to address many outstanding scientific questions in volcanology.
- 2) This paper has outlined UAV and photogrammetric survey workflows. It is essential that model errors are tracked and best-practise is followed in the reporting of model results. Several approaches have been discussed and examples of the type of data that should be reported have been provided by way of illustration.
- 3) The fidelity of texture in 3D photogrammetric models generated is of fundamental importance to studies that aim to map geological bedrock and distinguishes digital outcrop reconstruction from other applications of digital photogrammetry (e.g. time-series analyses of changes in terrain). In some situations, UAV-based imagery enables the observation of subtle textural features that are difficult to track on the ground. Successful survey design depends on identifying the resolution of features being examined in advance, although “exploratory” surveys also have significant value.
- 4) Moreover, the dyke-related features that can be captured by photogrammetric methods range from millimetre to kilometre scales. UAV-based photogrammetric methods are therefore ideal for multi-scale analysis of field data in 2.5D (e.g. GIS analysis of raster orthomosaics and DEMs) and 3D (e.g. point clouds, triangulated meshes and textured 3D models).
- 5) A method is outlined here for near-continuous, high resolution aperture measurement. Digital tools for measuring structural orientations and other characteristics are also discussed. We have shown that we are able to attach a level of measurement precision to the structural data that can be extracted from digital outcrop data that in some cases exceeds that easily attainable using conventional field techniques.
- 6) For the full potential of UAV technology to be realised, advanced applications should involve the use of sensors that collect beyond-visible remote sensing data (visible near infrared to shortwave infrared hyperspectral cameras, thermal infrared), and geophysical data (especially aeromagnetic surveys). These sensors enable mineralogical compositions and subsurface network geometries to be mapped and quantified. The application of photogrammetry to capture

structural and time-series data on active, near-surface dyke intrusive events is also an obvious area for fruitful research.

Acknowledgements

This research was funded by the Mineral Resources Flagship of the Commonwealth Science and Industrial Research Organisation. Dr. Eric Tohver, Dr. Steven J. Barnes, and Michael O'Brien are thanked for field assistance in Western Australia. David Wagner provided support for field work in Eastern California.

2.7 References

- Acocella, V. and Neri, M., 2009. Dike propagation in volcanic edifices: Overview and possible developments. *Tectonophysics*, 471(1): 67-77.
- Ague, J.J. and Brimhall, G.H., 1988. Magmatic Arc Asymmetry and Distribution of Anomalous Plutonic Belts in the Batholiths of California - Effects of Assimilation, Crustal Thickness, and Depth of Crystallization. *Geol Soc Am Bull*, 100(6): 912-927.
- Ameglio, L., Durufle, F., Jacobs, G, Chng, C., 2015. Light airborne platforms for monitoring mines and minerals. Third International Future Mining Conference. Sydney, NSW, November 2015, 11-20.
- Anderson, E., 1939. The dynamics of sheet intrusion, *Proceedings of the Royal Society of Edinburgh*, 58, 242-251. <http://dx.doi:10.1017/S0370164600011159>.
- Anderson, E., 1951. The dynamics of faulting and dyke formation with applications to Britain. Edinburgh: Oliver and Boyd, 206 p.
- Bai, T. and Pollard, D.D., 2000. Fracture spacing in layered rocks: a new explanation based on the stress transition. *J Struct Geol*, 22(1): 43-57.
- Bemis, S. P., Micklethwaite, S., Turner, D., James, M. R. Thiele, S., 2014. Ground-Based and UAV-Based Photogrammetry: A Multi-Scale, High-Resolution Mapping Tool for Structural Geology and Paleoseismology. *J. Struct. Geol.* 69, 163–178. <https://doi.org/10.1016/j.jsg.2014.10.007>.
- Berthod, C., Famin, V., Bascou, J., Michon, L., Ildefonse, B. and Monié, P., 2016. Evidence of sheared sills related to flank destabilization in a basaltic volcano. *Tectonophysics*, 674: 195-209.
- Browning, J., Drymoni, K. and Gudmundsson, A., 2015. Forecasting magma-chamber rupture at Santorini volcano, Greece. *Scientific Reports*, 5: 15785.
- Buckley, S., Ringdal, K., Dolva, B., Naumann, N., & Kurz, T., 2017. LIME: 3D visualisation and interpretation of virtual geoscience models. In EGU General Assembly Conference Abstracts v. 19, 15952.
- Carr, B. B., Clarke, A. B., Arrowsmith, J. R., Vanderkluyzen, L., Dhanu, B. E., 2018. The emplacement of the active lava flow at Sinabung Volcano, Sumatra, Indonesia, documented by structure-from-motion photogrammetry. *J. Volcanol. Geotherm. Res.* <https://doi.org/10.1016/j.jvolgeores.2018.02.00>.
- Carrecedo, J. C., 1994, The Canary Islands: an example of structural control on the growth of large ocean-island volcanoes, *J. Volcanol. Geotherm. Res.* 60, 221-241.

- Carrivick, J. L., Smith, M. W., Quick, J. E., 2016. *Structure from Motion in the Geosciences*. Oxford: Wiley-Blackwell, 208 p.
- Casagli, N., Frodella, W., Morelli, S., Tofani, V., Ciampalini, A., Intrieri, E., Raspini, F., Rossi, G., Tanteri, L., Lu, P., 2017. Spaceborne, UAV and ground-based remote sensing techniques for landslide mapping monitoring and early warning. *Geoenvironmental Disasters* 4, 1-9. <https://doi.org/10.1186/s40677-017-0073-1>.
- Cawood, A. J., Bond, C. E., Howell, J. A., Butler, R. W., Totake, Y., 2017. LiDAR, UAV or compass-clinometer? Accuracy, coverage and the effects on structural models. *J. Struct. Geol.* 98, 67-82. <http://dx.doi.org/10.1016/j.jsg.2017.04.004>.
- Cawood, A. J., Bond, C.E., 2018. eRock: an online, open-access repository of virtual outcrops and geological samples in 3D. *Geophys. Res. Abstracts* 20, EGU2018-18248.
- Cervelli, P.F., Fournier, T., Freymueller, J. and Power, J.A., 2006. Ground deformation associated with the precursory unrest and early phases of the January 2006 eruption of Augustine Volcano, Alaska. *Geophys Res Lett*, 33(18).
- Chaput, M., Famin, V. and Michon, L., 2017. Sheet intrusions and deformation of Piton des Neiges, and their implication for the volcano-tectonics of La Réunion. *Tectonophysics*, 717: 531-546.
- Chen, J.H. and Moore, J.G., 1979. Late Jurassic Independence dike swarm in eastern California. *Geology*, 7(3): 129-133.
- Compton, R., 1985. *Geology in the Field*. Wiley New York, 298 p.
- Daniels, K. A., Kavanagh, J. L., Menand, T. Sparks, R. S. J., 2012. The shapes of dikes: Evidence for the influence of cooling and inelastic deformation. *GSA Bull.* 124, 1102–1112. doi: 10.1130/B30537.1.
- Delaney, P. T., Pollard, D. D., 1981. Deformation of host rocks and flow of magma during growth of Minette dikes and breccia-bearing intrusions near Ship Rock, New Mexico. *USGS Professional Paper* 1202, 69 p.
- Delaney, P. T., Pollard, D. D., Ziony, J. I., Mckee, E. H., 1986. Field relations between dikes and joints: Emplacement processes and paleostress analysis. *J.Geophys. Res. Solid Earth* 91, 4920-4938.
- Delcamp, A., Troll, V.R., de Vries, B.v.W., Carracedo, J.C., Petronis, M., Pérez-Torrado, F. and Deegan, F., 2012. Dykes and structures of the NE rift of Tenerife, Canary Islands: a record of stabilisation and destabilisation of ocean island rift zones. *B Volcanol*, 74(5): 963-980.

- Dentith, M.C., Mudge, S.T., 2014. *Geophysics for the mineral exploration geoscientist*. Cambridge University Press. 438 p.
- Dering, G.M., Micklethwaite, S., Barnes S.J., Fiorentini, M., Cruden, A., Tohver, E., 2016. An elevated perspective: Dyke-related fracture networks analysed with UAV photogrammetry, *Acta Geologica Sinica*, 90 supp. 1: 54-55.
- Dering, G.M., Micklethwaite, S., Cruden, A.R., Barnes, S.J. and Fiorentini, M.L., 2019. Evidence for dyke-parallel shear during syn-intrusion fracturing: *Earth and Planetary Science Letters*, 507, pp.119-130, doi.org/10.1016/j.epsl.2018.10.024.
- Dewez, T. J. B., Girardeau-Montaut, D., Allanic, C., Rohmer, J., 2016. FACETS: A CloudCompare plugin to extract geological planes from unstructured 3D point clouds. *Int. Arch. Photogramm. Remote Sens. Spatial Inf. Sci.*, XLI-B5, 799-804. <https://doi.org/10.5194/isprs-archivesXLI-B5-799-2016>.
- Ebmeier, S. K., Andrews, B. J., Araya, M. C., Arnold, D. W. D., Biggs, J., Cooper, C. and 10 others, 2018. Synthesis of global satellite observations of magmatic and volcanic deformation: implications for volcano monitoring and the lateral extent of magmatic domains. *J. Applied Volc.*, 7. <https://doi.org/10.1186/s13617-018-0071-3>.
- Eisenbeiss, H., 2009. *UAV Photogrammetry*. PhD thesis. ETH Zurich.
- Elsworth, D. and S. J. Day, 1999. Flank collapse triggered by intrusion: the Canarian and Cape Verde Archipelagoes, *J. Volcanol. Geotherm. Res.* 94(1), 323-340.
- Ernst, R. E., Head, J. W., Parfitt, E., Grosfils, E., Wilson, L., 1995. Giant radiating dyke swarms on Earth and Venus. *Earth-Sci. Rev.* 39, 1-58.
- Fernández, O., 2005. Obtaining a best fitting plane through 3D georeferenced data. *J. Struct. Geol.* 27, 855-858.
- Fernández, J., Pepe, A., Poland, M.P., Sigmundsson, F., 2017. Volcano Geodesy: Recent developments and future challenges, *J. Volcanol. Geotherm. Res.* 344, 1-12. <https://doi.org/10.1016/j.jvolgeores.2017.08.006>.
- Funaki, M., Higashino, S-I., Sakanaka, S., Naoyoshi Iwata, N., Nakamura, N., Hirasawa, N., Obara, N., Kuwabara, M., 2014. Small unmanned aerial vehicles for aeromagnetic surveys and their flights in the South Shetland Islands, Antarctica. *Polar Science* 8, 342-356.

- García-Sellés, D., Falivene, O., Arbués, P., Gratacos, O., Tavani, S., Muñoz, J. A., 2011. Supervised identification and reconstruction of near-planar geological surfaces from terrestrial laser scanning, *Comput. Geosci.*, 37, 1584–1594. <https://doi.org/10.1016/j.cageo.2011.03.007>.
- Geshi, N. and Oikawa, T., 2014. The spectrum of basaltic feeder systems from effusive lava eruption to explosive eruption at Miyakejima volcano, Japan. *B Volcanol*, 76(3): 1.
- Glazner, A.F., Carl, B.S., Coleman, D.S., Miller, J.S. and Bartley, J.M., 2008. Chemical variability and the composite nature of dikes from the Jurassic Independence dike swarm, eastern California. *Geological Society of America Special Papers*, 438: 455-480.
- Gudmundsson, A., Kusumoto, S., Simmenes, T. H., Philipp, S. L., Larsen, B. Lotveit, I. F., 2012. Effects of overpressure variations on fracture apertures and fluid transport. *Tectonophysics* 581, 220-230.
- Hjartardóttir, A.R., Einarsson, P., Gudmundsson, M.T., & Högnadóttir, T., 2016. Fracture movements and graben subsidence during the 2014 Bárðarbunga dike intrusion in Iceland. *J. Volcanol. Geotherm.Res.* 310, 242–252.
- Hodgetts, D., Gawthorpe, R. L., Wilson, P., Rarity, F., 2007. Integrating digital and traditional field techniques using Virtual Reality Geological Studio (VRGS). In 69th EAGE Conference and Exhibition incorporating SPE EUROPEC 2007.
- Hopson, C.A., 1988. Independence dike swarm: origin and significance. *EOS*, pp. 1479.
- Hruska, R., Mitchell, J., Anderson, M., Glenn, N.F., 2012. Radiometric and geometric analysis of hyperspectral imagery acquired from an unmanned aerial vehicle. *Remote Sensing* 4, 2736-2752. doi:10.3390/rs4092736.
- Huang, Q. and Angelier, J., 1989. Fracture spacing and its relation to bed thickness. *Geol Mag*, 126(4): 355-362.
- Jackisch, R., Lorenz, S., Zimmermann, R., Möckel, R., Gloaguen, R., 2018. Drone-borne hyperspectral monitoring of acid mine drainage: an example from the Sokolov lignite district. *Remote Sensing* 10, 1-23. doi:10.3390/rs10030385.
- Jakob, S., Zimmermann, R., and Gloaguen, R., 2017. The need for accurate geometric and radiometric corrections of drone-borne hyperspectral data for mineral exploration: MEPHySTo—a toolbox for pre-processing drone-borne hyperspectral data. *Remote Sensing* 9, 1-20. doi:10.3390/rs9010088.

- James M.R., Robson S., 2012. Straightforward reconstruction of 3D surfaces and topography with a camera: accuracy and geoscience application. *J. Geophys. Res.* 117 F03017.
doi:10.1029/2011JF002289.F03017.
- James, M.R. and Robson, S., 2014. Mitigating systematic error in topographic models derived from UAV and ground-based image networks. *Earth Surface Processes and Landforms*, 39(10): 1413-1420.
- James, O.C., Mike, J.S. and Mike, R.J., 2017. Cameras and settings for aerial surveys in the geosciences: Optimising image data. *Progress in Physical Geography*, 41(3): 325-344.
- Jenness, M.H. and Clifton, A.E., 2009. Controls on the geometry of a Holocene crater row: a field study from southwest Iceland. *B Volcanol*, 71(7): 715.
- Jolly, R. J. H., Sanderson, D. J., 1995. Variation in the form and distribution of dykes in the Mull Swarm, Scotland. *J. Struct. Geol.* 17, 1543-1557.
- Jones, R.R., McCaffrey, K.J.W., Wilson, R.W. and Holdsworth, R.E., 2004. Digital field data acquisition: towards increased quantification of uncertainty during geological mapping. Geological Society, London, Special Publications, 239(1): 43-56.
- Kattenhorn, S., Watkeys, M., 1995. Blunt-ended dyke segments. *J. Struct. Geol.* 17, 1535-1542.
- Kavanagh, J. L., Sparks, R. S. J., 2011. Insights of dyke emplacement mechanics from detailed 3D dyke thickness datasets. *J. Geol. Soc., London* 168, 965-978. <https://doi.org/10.1144/0016-76492010-137>.
- Lague D., Brodu N., Leroux J., 2013. Accurate 3D comparison of complex topography with terrestrial laser scanner: application to the Rangitikei Canyon (NZ). *J. Photogrammetry and Remote Sensing* 82, 10–26
doi:10.1016/j.isprsjprs.2013.04.009.
- Lato, M. J.; Vöge, M., 2012. Automated mapping of rock discontinuities in 3D LiDAR and photogrammetry models. *Int. J. Rock Mechanics and Mining Science* 54, 150–158.
doi.org/10.1016/j.ijrmms.2012.06.003.
- Lister, J. R., Kerr, R. C., 1991. Fluid-mechanical models of crack propagation and their application to magma transport in dykes. *J. Geophys. Res. Solid Earth* 96, 10049-10077.
- Magee, C., Muirhead, J. D., Karvelas, A., Holford, S. P., Jackson, C. A. L., Bastow, I. D., Schofield, N., Stevenson, C. T. E., McLean, C., McCarthy, W., 2016. Lateral magma flow in mafic sill complexes. *Geosphere* 12, 809-841.

- Mahan, K.H., Bartley, J.M., Coleman, D.S., Glazner, A.F. and Carl, B.S., 2003. Sheeted intrusion of the synkinematic McDoyle pluton, Sierra Nevada, California. *Geol Soc Am Bull*, 115(12): 1570-1582.
- McCaffrey, K., Jones, R., Holdsworth, R., Wilson, R., Clegg, P., Imber, J., Holliman, N. and Trinks, I., 2005. Unlocking the spatial dimension: digital technologies and the future of geoscience fieldwork. *J Geol Soc London*, 162(6): 927-938.
- McGuire, W.J. and Pullen, A.D., 1989. Location and orientation of eruptive fissures and feederdykes at Mount Etna; influence of gravitational and regional tectonic stress regimes. *Journal of Volcanology and Geothermal Research*, 38(3): 325-344.
- Micheletti, N., Chandler, J. H., Lane, S. N., 2015. Investigating the geomorphological potential of freely available and accessible structure-from-motion photogrammetry using a smartphone. *Earth Surface Processes and Landforms* 40, 473-486.
- Nicholson, R., Pollard, D., 1985. Dilation and linkage of echelon cracks. *J. Struct. Geol.* 7, 583-590.
- O'Connor, J., Smith, M. J., James, M. R., 2017. Cameras and settings for aerial surveys in the geosciences. *Progress in Physical Geography*, 41, 325–344. <https://doi.org/10.1177/0309133317703092>
- Ouédraogo, M. M., Degré, A., Debouche, C., 2014. The high resolution digital terrain model, its errors and their propagation. A review. *Biotechnologie Agronomie Societe Et Environnement* 18, 407-421.
- Pagli, C., Wright, T. J., Ebinger, C. J., Yun, S. H., Cann, J. R., Barnie, T., Ayele, A., 2012. Shallow axial magma chamber at the slow-spreading Erta Ale Ridge. *Nature Geoscience* 5, 284-288.
- Raspini, F., Rossi, G., Tanteri, L., Lu, P., 2017. Spaceborne, UAV and ground-based remote sensing techniques for landslide mapping, monitoring and early warning. *Geoenvironmental Disasters* 4:9. doi 10.1186/s40677-017-0073-1.
- Rippin, D. M., Pomfret, A., King, N., 2015. High resolution mapping of supra-glacial drainage pathways reveals link between micro-channel drainage density, surface roughness and surface reflectance. *Earth Surface Processes and Landforms* 40, 1279-1290.
- Rivalta, E., Taisne, B., Bungler, A.P., Katz, R.F., 2015. A review of mechanical models of dike propagation: Schools of thought, results and future directions. *Tectonophysics* 638, 1-42.
- Roncella, R., Forlani, G., 2005. Extraction of planar patches from point clouds to retrieve dip and dip direction of rock discontinuities, Workshop, Laser Scanning 2005, Enschede, the Netherlands, September 12–14, 162–167.

- Ruch, J., Pepe, S., Casu, F., Solaro, G., Pepe, A., Acocella, V., Neri, M. and Sansosti, E., 2013. Seismotectonic behavior of the Pernicana Fault System (Mt Etna): A gauge for volcano flank instability? *Journal of Geophysical Research: Solid Earth*, 118(8): 4398-4409.
- Seers, T. D., Hodgetts, D. 2016a. Extraction of three-dimensional fracture trace maps from calibrated image sequences. *Geosphere*, 12(4), 1323-1340.
- Seers, T. D., Hodgetts, D, 2016b. Probabilistic constraints on structural lineament best fit plane precision obtained through numerical analysis. *J. Struct. Geol.*, 82, 37-47.
- Sigmundsson, F., Hooper, A., Hreinsdottir, S., Vogfjord, K.S., Ofeigsson, B.G., Heimisson, E.R., Dumont, S., Parks, M., Spaans, K., Gudmundsson, G.B., Drouin, V., Arnadottir, T., Jonsdottir, K., Gudmundsson, M.T., Hognadottir, T., Fridriksdottir, H.M., Hensch, M., Einarsson, P., Magnusson, E., Samsonov, S., Brandsdottir, B., White, R.S., Agustsdottir, T., Greenfield, T., Green, R.G., Hjartardottir, A.R., Pedersen, R., Bennett, R.A., Geirsson, H., La Femina, P.C., Bjornsson, H., Palsson, F., Sturkell, E., Bean, C.J., Mollhoff, M., Braiden, A.K. and Eibl, E.P.S., 2015. Segmented lateral dyke growth in a rifting event at Bardarbunga volcanic system, Iceland. *Nature*, 517(7533): 191-U158.
- Smith, M. W., Vericat, D., 2015. From experimental plots to experimental landscapes: topography, erosion and deposition in sub-humid badlands from structure-from-motion photogrammetry. *Earth Surface Processes and Landforms* 40, 1656-1671.
- Sparks, R., Biggs, J., Neuberg, J., 2012. Monitoring volcanoes. *Science* 335, 1310-1311.
- Tavani, S., Arbues, P., Snidero, M., Carrera, N., Muñoz, J. A., 2011. Open Plot Project: an open-source tool for 3-D structural data analysis. *Solid Earth*, 2(1), 53-63.
- Thiele, S.T., Micklethwaite, S., Bourke, P., Verrall, M., Kovesi, P., 2015. Insights into the mechanics of en-echelon sigmoidal vein formation using ultra-high resolution photogrammetry and computed tomography. *J. Struct. Geol.* 77, 27-44.
- Thiele, S. T., Varley, N., James, M. R., 2017a. Thermal photogrammetric imaging: a new technique for monitoring dome eruptions. *J. Volc. Geotherm. Res.* 337, 140-145.
- Thiele, S. T., Grose, L., Samsu, A., Micklethwaite, S., Vollgger, S. A., Cruden, A. R., 2017b. Rapid, semi-automatic fracture and contact mapping for point clouds, images and geophysical data. *Solid Earth* 8, 1241.
- Tibaldi, A., Rust, D., Corazzato, C. and Merri, A., 2010. Setting the scene for self-destruction: From sheet intrusions to the structural evolution of rifted stratovolcanoes. *Geosphere*, 6(3): 189-210.

- Townsend, M., Pollard, D. D., Johnson, K. Culha, C., 2015. Jointing around magmatic dikes as a precursor to the development of volcanic plugs. *Bull. Volcanol.* 77-92. doi10.1007/s00445-015-0978-z.
- Valentine, G. A., Krogh, K. E. C., 2006. Emplacement of shallow dikes and sills beneath a small basaltic volcanic center - The role of pre-existing structure (Paiute Ridge, southern Nevada, USA). *EPSL* 246, 217-230.
- Vasuki, Y., Holden, E.-J., Kovesi, P., Micklethwaite, S., 2014. Semi-automatic mapping of geological structures using UAV-based photogrammetric data: An image analysis approach. *Computers and Geosciences* 69, 22-32. <http://dx.doi.org/10.1016/j.cageo.2014.04.012>.
- Vollgger, S. A., Cruden, A. R., 2016. Mapping folds and fractures in basement and cover rocks using UAV photogrammetry, Cape Liptrap and Cape Paterson, Victoria, Australia. *J. Struct. Geol.* 85, 168-187.
- Vollgger, S. A., Cruden, A. R. (2018). Bingie Bingie (NSW) orthophotograph basemap A3. Figshare: Figure. <https://doi.org/10.4225/03/5a9dd6bc42910>.
- Wallace, L., Lucieer, A., Watson, C., Turner, D., 2012. Development of a UAV-LiDAR system with application to forest inventory. *Remote Sensing* 4, 1519-1543. doi:10.3390/rs4061519.
- Wadsworth, F.B., Kennedy, B.M., Branney, M.J., von Aulock, F.W., Lavallée, Y. and Menendez, A., 2015. Exhumed conduit records magma ascent and drain-back during a Strombolian eruption at Tongariro volcano, New Zealand. *B Volcanol*, 77(9): 1.
- Wauthier, C., Cayol, V, Smets, B, d'Oreye, N, Kervyn, F., 2015. Magma pathways and their interactions inferred from InSAR and stress modeling at Nyamulagira Volcano, D.R. Congo. *Remote Sensing* 7, 15179-15202. doi:10.3390/rs71115179.
- Weertman, J., 1971. Theory of water-filled crevasses in glaciers applied to vertical magma transport beneath oceanic ridges. *J. Geophys. Res.* 76, 1171–1183.
- White, R.S., Drew, J., Martens, H.R., Key, J., Soosalu, H., Jakobsdóttir, S.S., 2011. Dynamics of dyke intrusion in the mid-crust of Iceland. *EPSL* 304, 300-312.

CHAPTER 3

Evidence for dyke-parallel shear during syn-intrusion fracturing

Accepted for publication in Earth and Planetary Science Letters

Gregory M. Dering¹, Steven Micklethwaite², Alexander R. Cruden², Stephen J. Barnes³, Marco
Fiorentini¹

¹ARC Centre of Excellence for Core to Crust Fluid Systems, School of Earth Science, The University of Western Australia, Crawley, Western Australia 6009, Australia

²School of Earth, Atmosphere, and Environment, Monash University, Clayton, 3800, Australia

³Mineral Resources Flagship, CSIRO, Perth, Western Australia 6151, Australia

Corresponding author: Gregory Dering (gregory.dering@research.uwa.edu.au)

Highlights

- Exceptional exposures show dyke-parallel shear coeval with dyke emplacement
- Outcrop data are compatible the moment tensor solutions from Icelandic seismicity
- Dykes lie within a corridor of fractured host rock about twice the background intensity
- Dyke propagation in a non-coaxial strain field triggers shear on dyke-parallel planes

ABSTRACT

Dyke intrusion is a highly dynamic process with seismicity preceding and accompanying magma emplacement on timescales of hours to days. Recent surveys of microseismicity indicate shear failure along fault planes parallel to the orientation of intruding dykes. However, the precision of earthquake hypocentre locations is typically limited to tens or hundreds of meters and cannot resolve whether the hypocentres relate to strain of wall rock fragments within the dykes, fault damage around the intrusions or peripherally in the country rock. Here we present high-resolution three-dimensional (3D) reconstructions of outstanding coastal exposures of a swarm of 19 dolerite dykes, near Albany, Western Australia using an unmanned aerial vehicle and Structure-from-Motion photogrammetry. It is observed that the number of faults and joints increases towards the dyke swarm, which, alongside mutually overprinting relationships, indicate that dyke emplacement and faulting were coeval. The faults contain cataclasites and are parallel to the dykes. In contrast, Mohr-Coulomb theory predicts shear failure on strike-parallel faults inclined $\sim 30^\circ$ to the dyke plane. The faults and joints form a damage zone associated with the dyke swarm, even though the dykes themselves occupy Mode I extension fractures. These results confirm the recent geophysical evidence for dyke-parallel shear failure that can occur in the host rocks around intruding dykes. We suggest that coeval dyke-parallel seismicity both reactivated existing fracture networks and nucleated new fractures. Based on the premise that host-rock fracturing induces changes in elastic properties, remote stresses can reorientate locally leading to shear failure. This model provides for the first time an explanation for the origin of double-couple failure that is parallel in 3D (strike and dip) to dykes during their emplacement.

3.1 Introduction

Faulting has long been conceptually linked to dyke propagation in the brittle crust. However, increasingly high-resolution monitoring of seismicity during dyke emplacement events reveals patterns of hypocentre locations and inferred fault kinematics that are not easily explained by a linear progression of the dyke tip and deformation front in space and time. While seismological data captures the timing and rate of deformation with precision, analysis of exhumed intrusions and adjacent country rocks resolves the key spatial relationships between dykes and fractures in the country rock.

High strain rates produced by the propagation and inflation of dykes generate seismicity (Toda et al., 2002; Rubin et al., 1998; Hill, 1977). Intrusion events can release large amounts of seismic energy during lateral propagation (Sigmundsson et al., 2015), vertical propagation (Minson et al., 2007; Toda et al., 2002), and dyke inflation (White et al., 2011). In turn, seismicity tracks both the ascent and lateral propagation of dykes through the crust (Aoki et al., 1999; Shelly and Hill, 2011). These studies show that fault damage and fracturing play a crucial role in the magma emplacement process, preceding and accompanying intrusion on timescales of hours and days. Even at mid-crustal depths, typically dominated by ductile deformation, seismicity is closely associated with dyke emplacement (Ukawa and Tsukahara, 1996; White et al., 2011).

Mechanical models of dyke propagation in brittle crust predict shear failure on fault planes oriented $\sim 30^\circ$ to the dyke plane (Rubin and Gillard, 1998). However, White et al. (2011) used moment-tensor solutions to demonstrate that a microseismic swarm at Mount Upptyppingar, Iceland (March 2007-March 2008) was associated with double-couple failure parallel to the plane of an intruding dyke. Throughout this paper ‘parallel’ refers to the co-planar orientation of dykes and fractures in 3D. In order to resolve the conundrum of where such dyke-parallel shear failure occurs, alternative high-resolution datasets are required.

Here we use Structure-from-Motion (SfM) photogrammetric data collected from an Unmanned Aerial Vehicle (UAV) to examine the orientation and timing relationships between fault damage and a basaltic dyke swarm at a resolution not previously achieved. We derive outcrop map data for the dykes and associated fault-joint networks, which resolve the fracture network to centimetre resolution over an area of 10,000 m² within a unified spatial reference frame. Accuracy and precision of the outcrop model and structural data are constrained by high precision survey of ground control points. These ultra-high-quality data enable us to resolve the relative timing and spatial characteristics of dyke-parallel fault slip, and to discuss implications for microseismic studies of dyke intrusion.

3.2 Dyke-induced faulting, fracturing, and seismicity

3.2.1 Mechanical predictions

When idealised as an overpressured, fluid-filled crack, dyke propagation is expected to occur in the plane of maximum principal stress, opening in the direction of least principal stress (Anderson, 1951). Linear elastic fracture mechanics (LEFM) predict that stress singularities at dyke tips allow the propagation of a dyke through elastic rock. The concentration of extensional and shear stress at dyke tips leads to tensile failure not only in the plane of the dyke but also rigid-plastic failure in the surrounding volume of host rock (Delaney et al., 1986).

In addition to tensile failure, which forms joints, the orientation of potential shear fractures out of the plane of the propagating dyke is described by the Coulomb failure criterion in terms of the internal angle of friction and the maximum and minimum principal stress directions. The angle between the maximum principal stress direction and potential shear fractures has been found by rock mechanics experiments to range from $\sim 15^\circ$ – 32° , depending on the shear strength of the rock (Jaeger and Cook, 1979 and references therein). Shear failure along fractures that lie within this range of angles relative to the dyke plane is attributed to a stress change induced by dyke emplacement (Rubin and Pollard, 1988). The potential for shear failure is restricted to the region ahead of the dyke tip where differential stress is increased as a result of dyke inflation. A stress change accompanying dyke inflation that is insufficient to nucleate new faults in solid rock ahead of the dyke may instead result in shear along fractures that are favourably oriented for reactivation (Rubin and Gillard, 1998). The range of fracture orientations with potential for reactivation as shear fractures increases for dykes with high magma pressure relative to regional stress, but does not include fractures parallel to the dyke plane. A notable exception are normal faults that form under exceptionally low confining stress in the uppermost few km of the crust, where they are linked to fissures and slip at angles as low as $\sim 5^\circ$ to the maximum principle stress (e.g. Forslund and Gudmundsson, 1992).

Stress concentrations at dyke tips have also been predicted to result in regions of diffuse fracturing and cataclasis, described as process zones (Delaney et al., 1986; Gudmundsson, 2011a). In this study the dykes are hosted in relatively homogenous host rocks. However, strong mechanical contrasts within host rocks have been shown to affect the local stresses around sheet intrusions and their propagation paths (Gudmundsson et al. 2011b). For mafic magmas, which have relatively low viscosity, dyke-induced fracturing of relatively isotropic host rocks is a balance between the magmatic driving pressure, regional stresses acting on the dyke walls, and elastic moduli of the host rock. For a vertical dyke with uniform internal pressure in the plane of maximum compressive stress, the change in the magnitude of the minimum principal stress induced by dyke dilation is described by LEFM (Delaney et al., 1986) as:

$$\frac{\sigma_{ij} - \sigma_{ij}^r}{P_m - S_h} \cong \frac{C g_{11}(\theta)}{\left(\frac{2r}{A}\right)^{0.5}}$$

(Equation 1)

such that the stress change at any point in response to dilation in the direction with normal vector i and traction vector j is $\sigma_{ij} - \sigma_{ij}^r$, the uniform pressure exerted by the magma on the dyke walls is P_m , the least compressive regional stress is S_h (which is assumed to be parallel to the dyke opening direction), θ is the angular position from the crack tip, r is the distance from the crack tip, A is the dyke half length, g_{11} is the component of magmatic pressure acting normal to the dyke plane, and C is a factor related to stress intensity (Broek, 1986). By this approximation, an increase in tensile stress ($\sigma_{ij} - \sigma_{ij}^r$) is positive and proportional to the driving pressure ($P_m - S_h$). For $\sigma_{ij} - \sigma_{ij}^r$ parallel to S_h , tensile failure may occur at length r away from the dyke where $\sigma_{ij} - \sigma_{ij}^r$ exceeds the tensile strength of the host rock. This describes the formation of dyke-parallel joints around the leading edge of a propagating dyke but does not provide an explanation for dyke-parallel shear failure. This will occur more easily along favourably oriented pre-existing planar discontinuities rather than form new fractures. However, even in such circumstances, pre-existing dyke-parallel discontinuities are not expected to fail under shear if the dyke remains parallel to the maximum principle stress.

The relationship between dyke-induced deformation and tip propagation has been further studied using a viscous fluid mechanics approach. Mériaux et al. (1999) modelled the process zone as a region of zero elastic strength, based on the assumption derived from LEFM that stress and strain intensity increase toward the dyke tip. In this model the dyke tip coincides with the point of failure, after which the damaged volume of host rock retains no strength and the magma passes through it. This process is estimated to result in degradation of the host rock at distances of ~ 1 m from the dyke tip, but does not explain the extent of dyke-induced fracture described by Delaney et al. (1986). Moreover, geophysical observations summarised in the following section are inconsistent with the assumption that dyke-induced deformation is centred on the propagating dyke tip.

3.2.2 Geophysical observations

Deformation is observed indirectly during dyke emplacement events mainly by analysis of seismic signals. Dyke-induced earthquakes occur as swarms that typically migrate over a timeframe that overlaps with the period of dyke inception and growth. In a comprehensive review of dyke-induced seismicity, Rivalta et al. (2015) concluded that hypocentre locations are, at most, loosely associated with the passage of an advancing dyke tip. In detail, the distributions of hypocentres show spatio-temporal patterns not explained by tensile failure at the tip during propagation. Such patterns include the retreat of hypocentres away from the leading edge and back along the margins and/or keel of the dyke during its growth (Segall et al., 2013; Aoki et al. 1999; Sigmundsson et al., 2015). Moreover, dyke-induced

failure of host rock that is critically stressed can result in hypocentre distributions that do not reflect the exact extent or geometry of the dyke (Rubin et al., 1998; Toda et al., 1998). In such instances the migration of seismicity does not show any directional pattern and is instead concentrated in slip patches in the host rock. These data suggest that background stress state affects the pattern of seismicity observed during dyke emplacement.

However, new observations are emerging that dyke parallel fractures can be related to dyke-emplacement. Based on a particularly thorough analysis of dyke-induced seismicity from Mount Upptyppingar, Iceland, comprising >200 focal mechanisms and fault-plane solutions, White et al. (2011) described magma injection accompanied by shear failure on planes uniformly parallel to the inflating dyke plane. During a two-week period in 2007 ~500 microseismic events were recorded at depths from 13-18 km. Moment tensor solutions show that fault mechanisms switched frequently between normal and reverse failure on planes parallel to the dyke. Focal mechanisms were observed to migrate initially up-dip, but also down-dip and laterally through a tabular volume of crust. The host rock envelope in which seismicity was concentrated was inferred to contain also the inflating dyke. The total thickness of the dyke was estimated to be 1 m, as determined by geodetic measurements of surface deformation.

However, the relative lack of precision of focal mechanism locations could only constrain seismicity to a tabular volume of crust c. 100 m thick in the vicinity of the dyke. Since the dyke aperture is less than the spatial error associated with the hypocentre locations, the locus of seismic strain with respect to the dyke margins remains unclear. Working within the bounds of this uncertainty, three deformation mechanisms have been proposed by White et al. (2011) to explain seismic observations from the Upptyppingar event. The first is, rupture of chilled margins formed by solidified plugs within the dyke against the dyke walls (Fig. 1a). This mechanism accounts for the migration of hypocentres away from an inferred leading edge of the dyke. A second proposed mechanism is shear failure in the plane of magma injection (Fig. 1b). This is made possible by the moderate dip (40°) of the dyke within a regional stress field where the maximum principal stress is vertical. Although dyke propagation out of the plane of principal stress is rare, the asymmetric stress field around the dyke tip could promote Mode II shear failure over Mode I opening. A third possible explanation is microseismicity within a process zone that is active during dyke tip propagation as well as during inflation of the dyke away from the tip zone (Fig. 1c). In light of the gap between mechanical models and geophysical observations, this study addresses the development of dyke-induced macrofracture networks and their role in dyke propagation by direct observation of an exhumed dyke swarm and surrounding fracture network.

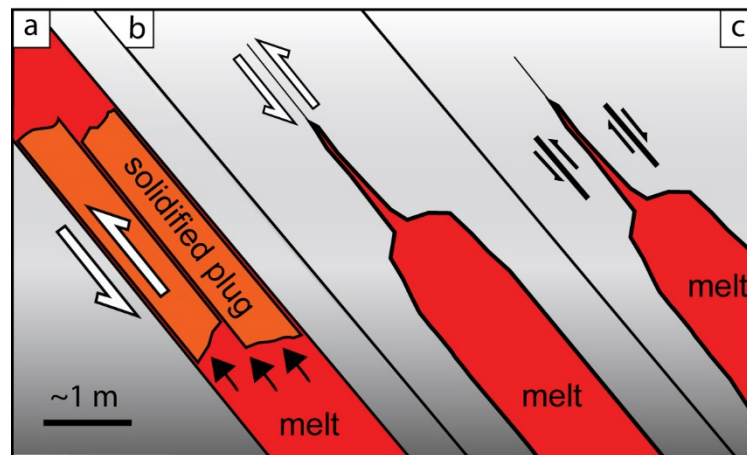


Figure 1 Schematic diagrams of possible dyke-parallel fault mechanisms after the scenarios proposed by White et al. (2011) for an inclined dyke. (a) Faulting along dyke margin accommodated by movement of solidified plug. Failure along the chilled margin results from magmatic overpressure. Sense of shear can be normal, reverse (shown), or oblique. (b) Shear failure mechanisms peripheral to the tip of a propagating dyke include faulting in the plane of magma propagation and (c) to either side of the dyke.

3.3 Geological setting

3.3.1 Albany-Fraser Orogen

The study area is located 3 km south of Albany, Western Australia on the Vancouver Peninsula. The geology of the site, including the mafic dyke swarm, was first described in the field notes of Charles Darwin on the homeward journey of the *Beagle* in 1836, as a “Granite promontory penetrated by a very great number of veins [...] composed of bright green greenstone,” (Armstrong, 1985). The ‘granite’ host rocks described by Darwin comprise Mesoproterozoic granulite facies metamorphic rocks and syn-orogenic felsic intrusions of the Western Nornalup Zones of the Albany-Fraser orogenic belt, a long-lived Proterozoic craton margin (Spaggiari et al., 2015). The host rocks are dominated by granitic and dioritic intrusions emplaced into garnet-sillimanite paragneiss (Fig. 2) that have been exhumed since ca. 1159 Ma (Scibiorski et al., 2015). The granulite facies basement rocks which host the dyke swarm are non-conformably overlain by Eocene marine sandstone and limestone and Quaternary dune deposits.

3.3.2 Post-Albany-Fraser Orogen mafic intrusions

The metamorphic basement rocks are crosscut by dolerite dykes and sills that are undeformed and not metamorphosed. Steeply dipping dolerite dykes occur in swarms that are sparsely distributed over 250 km along the coast westward from Albany and mainly strike WNW (Harris and Li, 1995). Individual dykes are typically 1 m to 5 m wide (Brenna and Gee, 2014). Compositions are dominantly basaltic, characterised by intergranular plagioclase and ophitic clinopyroxene with plagioclase phenocrysts up to 1 cm. The extent and geometry of post Albany-Fraser Orogen intrusions is known from coastal outcrop mapping and aeromagnetic data interpretation. However, the resolution of aeromagnetic data (40 m cell size) is coarse compared to the size of individual dyke segments, and a dense swarm of small dykes is typically indistinguishable from a single continuous dyke both horizontally and vertically over length scales of tens of metres.

The ages of post-orogenic dolerite dykes and sills distributed along the south coast of Western Australia were estimated by Harris and Li (1995) using paleomagnetic methods, but not specifically for the Albany dyke swarm. Remnant paleomagnetic poles from 14 mafic intrusions were correlated with the apparent polar wander path of Australia. The resulting data yield a principal cluster of Cambrian age correlations. A second cluster of mid-Carboniferous age is interpreted from four of the sites. Multiple samples were analysed from each study site but yielded at most a single age correlation. The spatial segregation of age correlations between sites suggests that the Cambrian and mid-Carboniferous intrusions occupy separate dyke swarms. We assume the dykes that comprise the swarm within the Albany study area all to be of the same age, consistent with the findings of Harris and Li (1995) from the surrounding region. This assumption is also supported by the compositional homogeneity of the

dykes within the study area. There are no published radiogenic age data of mafic dykes cross-cutting the western Albany-Fraser Orogen. In the absence of radiogenic ages, and the scatter of paleomagnetic results, the age of the Albany dykes remains unresolved.

3.3.3 Vancouver Peninsula locality

The host rock of the Vancouver Peninsula is dominated by granoblastic monzogranite emplaced into migmatitic orthogneiss. Metamorphic foliation strikes ENE, parallel to the axis of the Albany-Fraser Orogen. The study area is located on the east side of the peninsula where a subvertical dyke swarm with 20 discrete segments is exposed in a subhorizontal wave-polished outcrop. From here on we refer to the zone of granite-gneiss host rock and dykes occupied by the swarm as the 'dyke corridor'. The geometry of the dykes means that the study locality effectively exposes a cross section perpendicular to the dyke swarm (Fig. 3).

Dolerite dykes and brittle fault zones on the peninsula dominantly strike WNW and crosscut pre-existing intrusive contacts and metamorphic foliation. The swarm is dominated by overlapping planar dyke segments ranging in aperture from 10 cm to 5 m, dipping $>85^\circ$, and striking $279^\circ \pm 6^\circ$. Non-planar, <20 cm wide dyke apophyses exhibit rotations in strike up to 90° from the mean swarm orientation. Dykes within the study area are tholeiitic dolerites. Groundmass crystal size and phenocryst abundance increase with distance from the dyke margin and with dyke thickness. The dyke cores comprise a fine-grained matrix of plagioclase, ophitic clinopyroxene, and late-crystallising Fe-Ti-oxides. The margins of the dykes are chilled against the host rock.

Evidence of thermo-mechanical erosion of host rock during dyke emplacement is uncommon and isolated. Examples are restricted to decimetre-scale buds (cf. Delaney and Pollard, 1981) on the margins of a few >2 m wide dyke segments, which intersect pre-existing cataclasite zones that were presumably weaker than the host rock. Where dykes exhibit jogs and steps, the opposing walls are symmetrical such that the host rock can be restored to a pre-dyke configuration. Host rock features displaced by dyke inflation include pegmatite pods and veins. These features are offset markers that can also be restored to pre-dyke geometries, which demonstrate that the wall rock is completely preserved on the dyke margins. The ubiquity of chilled margins, aligned piercing points and symmetrical steps in dyke margin geometries demonstrates that the dykes opened and solidified without removing significant wall rock.

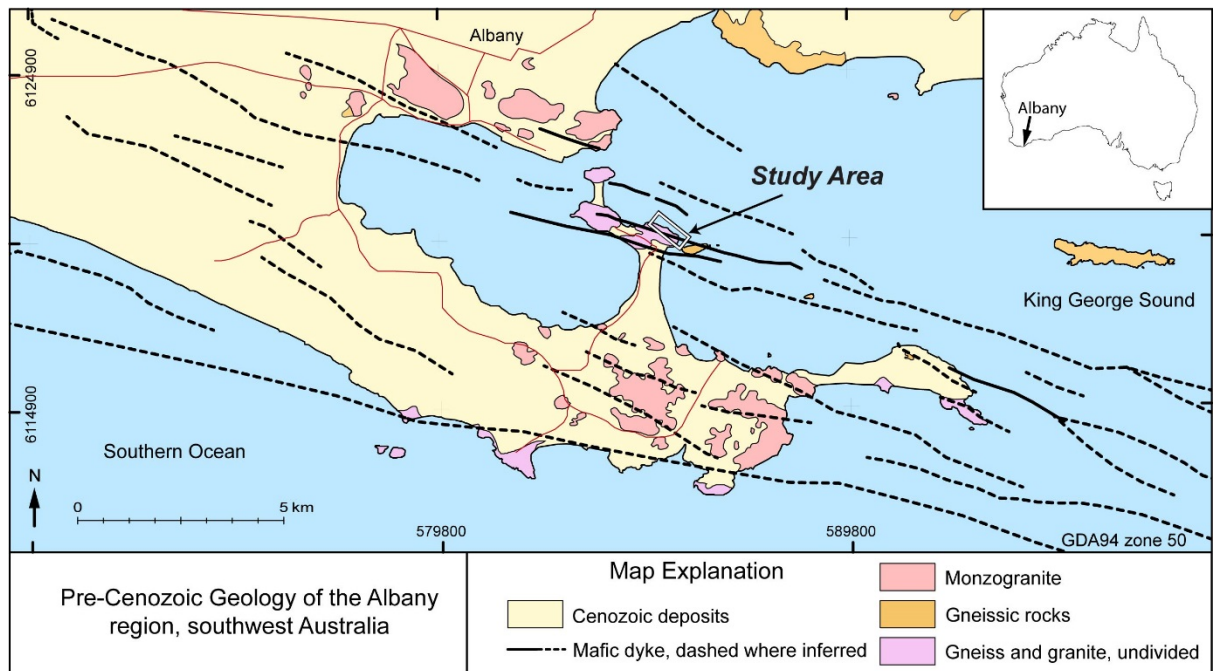


Figure 2 Dykes near Albany, Western Australia, occur in a WNW-trending swarm 6 km wide and at least 40 km long. Dyke traces are mostly interpreted from reduced to pole aeromagnetic data. Exposed dykes are all associated with linear magnetic anomalies, shown as solid black lines. However, not all magnetic lows that intersect bedrock exposure reveal dykes. Bedrock geology modified from Fitzsimons and Buchan (2005).

3.4 Fracture and dyke mapping

3.4.1 UAV-assisted photogrammetry

Digital photogrammetry involves processing a set of images acquired from a camera in order to reconstruct a 3D scene in the form of a point cloud, as well as derivative datasets such as textured wireframe models, digital elevation models (DEMs) and orthoimages. A key advancement of SfM photogrammetry is the ability to process images from unconstrained camera positions, without the need for highly calibrated *a priori* camera models. As a result, there is greater flexibility in image overlap, camera orientation, and distance to subject to generate a 3D model. These attributes lend themselves well to UAV deployment and structural analysis (Bemis et al., 2014; Vollgger and Cruden, 2016). Using UAV photogrammetry, we surveyed and digitally reconstructed a coastal outcrop at Vancouver Peninsula that covers a 13,000 m² swath of continuous bedrock exposure of Albany dykes and their country rocks (Fig. 4a). The accuracy of structural analysis derived from photogrammetric models has been found to be comparable to 3D datasets generated by laser scanning (Favalli et al, 2012; Thiele et al., 2015, Smith et al., 2016). Photogrammetric model metrics and error analysis methods are provided in Electronic Supplement 1.

The 3D traces of planar structures (fractures, faults, dyke walls, gneissic foliation) intersecting the outcrop surface were mapped from an ultra-high resolution orthorectified image (3.5 mm/pixel) and DEM (7.0 mm/pixel) derived from the dense point cloud. The planes of best fit for each joint, fault, and dyke margin were determined by implementation of a least squares regression analysis in Java, following the methods of Thiele et al. (2015). We compared the digitally extracted strike data with field data measured from 67 sites using a compass clinometer (Fig. 4c), which yielded a small standard deviation of 4°. This difference is within the measurement error of a field compass and demonstrates that the digital strike data are reliable. Dip information extracted by the plane-fitting method were found to be less accurate, due to false dip measurements for structures defined by points with high collinearity. Corrections to false dip measurements were applied manually using the open-source point cloud editing program CloudCompare (<http://www.cloudcompare.org>).

We evaluated the fossil evidence for off-dyke brittle deformation by measuring joint and fault intensity at multiple scales, from millimetre to decametre distances from dyke margins. Spacing and orientation data across 5 orders of magnitude were measured with 1D line sampling methods commonly referred to as scanline mapping (Huang and Angelier, 1989; Bai and Pollard, 2000). A scanline at the decametre scale, using the digital data, captured the fault, joint, and dyke spacing across the entire dyke swarm and surrounding bedrock over a distance of 435 m (Fig. 4a). To measure the intensity of brittle deformation surrounding dyke tips, a second set of fracture data was directly recorded in the field along eight 1D scanlines. Hereafter we refer to these as metre-scale scanlines that capture structural data at 1

mm resolution over lengths of 8 – 13 m, depending on the extent of the outcrop with respect to dyke margins.

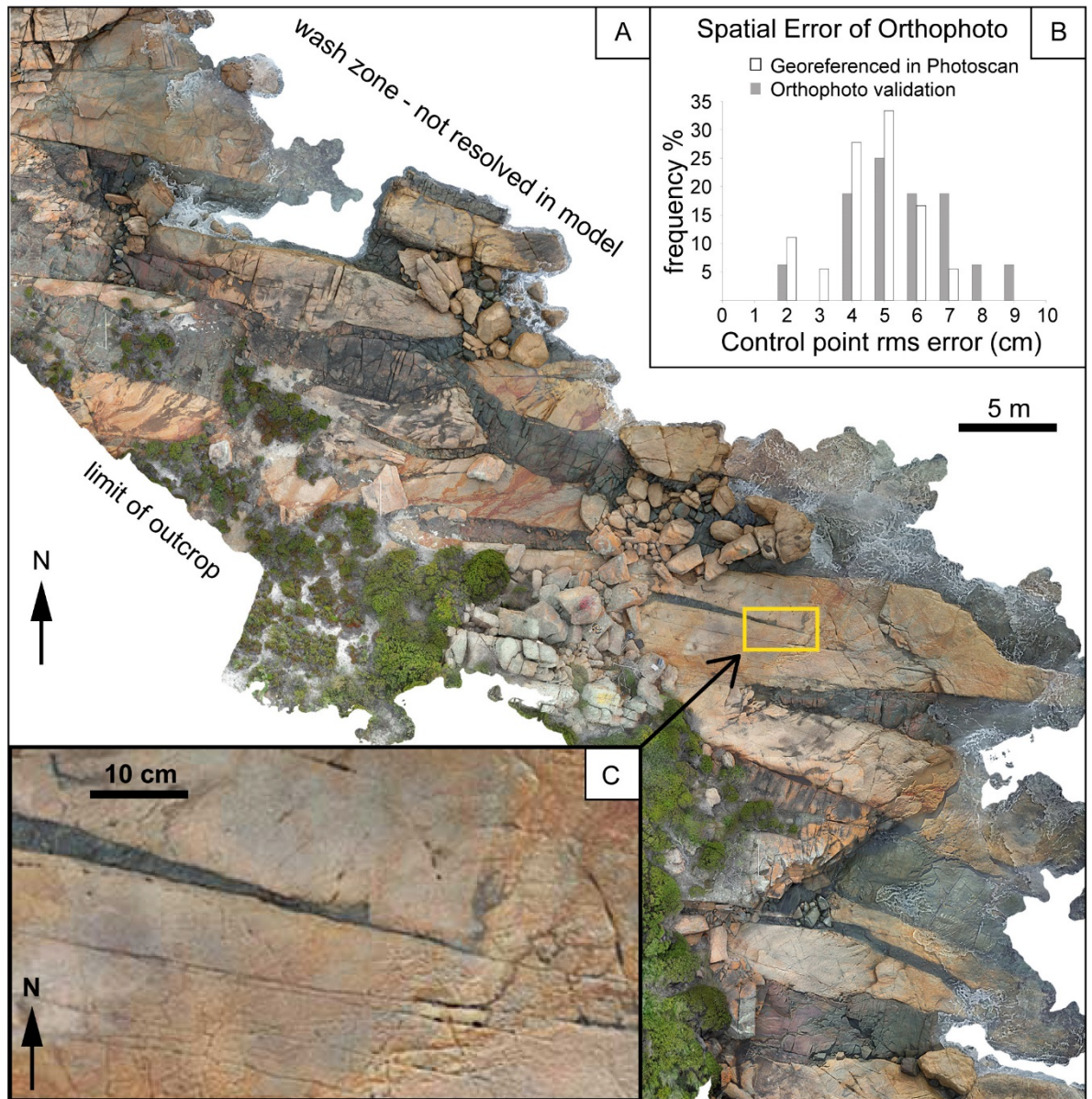


Figure 3 Photogrammetry outputs from within the dyke corridor and error analysis of modelled outcrop geometry. (a) Orthorectified image of dolerite dykes in coastal outcrop generated from Agisoft Photoscan. (b) Root-mean-square error of ground control points projected to orthorectified image and DEM versus total station field survey. (c) Orthorectified image of dyke tip and adjacent fractures in host rock.

3.5 Brittle deformation around dykes

3.5.1 Fracture populations

The scanline data from both the metre- and decametre-scale transects reveal that the dominant fracture set is a WNW-striking, steeply-dipping set of joints and faults, parallel to the dyke swarm (Fig. 4b). Offset markers are rare within the host rock. Therefore, narrow faults are not reliably distinguished from joints within the dominant fault-joint population (Figs. 6 and 7), but probably represent $\geq 10\%$ of the fractures based on the presence or absence of cataclasite as discussed in Section 3.5.2 below. Fractures that exist over a range of other orientations post-date the emplacement process entirely or do not play any significant role in the development of the dyke swarm. NNW- and NNE-striking joint populations are distinguished in detailed outcrop maps (Fig. 5a). These northerly striking joint sets are shown to abut the dominant WNW fault-joint population (Fig. 5) and therefore post-date it. Where NNW-striking joints interact with dyke margins, strain is dispersed within dense networks of cooling joints in dolerite (Fig. 5b). The northerly-striking joint populations are poorly resolved and underrepresented in the decametre-scanline data because of sampling bias along the NNE-trending scanline and also because most segments are shorter than the trace length sampling threshold of 2 m. No correction has been applied, as the northerly-striking joints have been shown to post-date the dykes. Fractures that are shallowly N and E-dipping (Fig. 4b) are attributed to exfoliation joints within the granite and are consistent with the overall moderate to shallow eastward dip of the outcrop surface into King George Sound (Fig. 2). A steeply dipping foliation within host rock gneissic domains strikes NNE to ENE and appears to have played no significant role in the evolution of the dyke swarm.

3.5.2 Pre- and syn-emplacement dyke-parallel shear

Field relations and microstructural features show that dyke-parallel fault-joint networks were active prior to and during the earliest phases of dyke emplacement. Where dykes interact with fault rocks they have magmatic margins that are chilled against indurated cataclasite zones, as shown by an intact centimetre-scale dyke tip in Figure 6a. At such localities, the solidified magma is undeformed and invades the pre-existing cataclasite. However, in addition to pre-emplacement shear, offset relations show that some faulting occurred during at least the earliest phases of dyke development. An early-emplaced dyke within the swarm is offset by small faults that are in turn truncated by a later dyke (Fig. 6b).

Cataclasites comprise material derived entirely from granitic host rocks, including microcline, quartz, and biotite. Particle sizes within the cataclasite zones range from 10 μm to 5 mm and locally show weak segregation according to grain size (Fig. 7). Grain size layering within the faults suggests that grain size reduction and sorting occurred during shear (Fig. 7a). Along the cataclasite margins, rigid microcline and quartz fragments are rotated and sub-rounded to angular. Grain rotation and mismatched wall rock asperities are further evidence for cataclasis. These observations demonstrate that some of the

structures associated with the dykes accumulated shear displacement and do not represent opening Mode I fractures (i.e. joints), despite being parallel to the dykes.

3.5.3 Decametre scanline results

There is a spatial relationship between fracture density and the location of the Vancouver Peninsula dyke swarm. The 450 m scanline, oriented perpendicular to the dyke swarm and dominant structural fabric, reveals a change in fault-joint intensity between the dyke corridor and the non-intruded host rock to the north and south of the swarm. Analysis of fracture intensity excludes the post-intrusion northerly-striking joint set (Figs. 5a and 8a rose diagram). The exclusion of these data makes little difference to the result, as the late joints occur with similar frequency across the entire study area (Electronic Supplement 2). Though the late northerly trending joints differ markedly in length and morphology from the dominant dyke-parallel population, it cannot be ruled out that some WNW-striking fractures (Fig. 5) also developed after dyke emplacement. In order to report fracture intensity, we normalised fracture spacing results over one-metre intervals, following the convention of Ortega et al. (2006). The cumulative thickness of the dyke swarm is 33 m, occupying a corridor 90 m wide. Because there is no offset in geological markers across dykes, and the morphology of opposing margins match across each dyke, no significant amount of host rock has been lost in the course of dyke emplacement. As a result, the scanline length has been corrected for the 33 m of dyke inflation to a total length of 427 m.

The positions and apertures of 14 individual dyke segments intercepted along the decametre scanline are compared with fracture intensity in Fig. 8. The principal result to emerge from this analysis is that fracture density is 2.2 ± 0.7 times higher within the dyke swarm corridor than in adjacent country rocks. Intriguingly, within the swarm, peak fracture intensities are not co-located with the margins of individual dyke segments. There is also no detectable correlation between dyke aperture and fracture intensity within the swarm (see section 3.5.4; Fig. 8a and b). Variation in fracture intensity within the dyke corridor is large, jumping from minimum (0) to maximum (6) values over distances of 1 – 2 m. To analyse swarm-wide trends at the 10- to 100-metre scale, the data were reduced to a moving average of 5 consecutive fracture intensity intervals. This moving average reveals a roughly symmetrical decrease in fracture intensity away from the dyke swarm to the north and south. The average background fracture intensity away from the dyke swarm is 0.9 ± 0.2 .

3.5.4 Metre-scale scanline results

Fracture intensity with respect to the margins of 4 dyke segments are reported for 0.5 m sample intervals along with the locations of individual faults and joints, and their apertures (Fig. 9). Due to the scarcity of offset markers, the presence of cataclasite fracture fill was used as a proxy to distinguish faults from joints. Fracture intensity and aperture data derived from direct outcrop measurements highlight three results:

- 1) Although there is a clear increase in fracture intensity relative to host rock outside the dyke swarm the relationship between fracture intensity and individual dykes within the swarm is less clear.
- 2) There is an asymmetric distribution of fracture intensity with respect to dyke margins.
- 3) There is no consistent correlation between fracture spacing and proximity to individual dyke margins.

Poles to planes in equal area stereonet projection show that the major fracture populations for each scanline are parallel to the dyke margins. Within the WNW-striking fault-joint population, the mean angular difference to the adjacent dyke walls is 10° with a standard deviation of 4° . Northerly-striking joint populations that post-date dyke emplacement (Fig. 5) are withheld from the fault-joint intensity analysis.

To understand the distribution of fault-joint data in the context of predictions from LEFM, we calculated the minimum horizontal stress change with respect to dyke margins over the distances of the scanlines (Fig. 9). Tensile failure around a vertical, dilatant dyke tip during propagation, as described by Equation 1, is characterised by a reduction in S_h . Here the change in S_h normal to the dyke plane at the level of the dyke tip is calculated according to the approximation of Delaney et al. (1986; Eqn. 4). The key observation is that variations in brittle deformation do not match the symmetrical, asymptotic change in S_h over the same distance, as predicted by LEFM (Eqn. 1) for an opening Mode I magma-filled fracture.

Those fractures with measurable aperture that contained cataclasite were identified as faults, despite the absence of measureable displacement indicators. The width of cataclasite zones can be treated as a rough proxy for displacement, since fault thickness is positively correlated with displacement (Childs et al., 2009 and references therein). The range of values for fault thickness shown in Figure 9, indicates that the maximum displacements for the faults within the dyke swarm is expected to be on the order of 0.01-1.0 m. Discounting the post-intrusion joint sets, cataclasite-bearing faults make up ~12% of fractures along the metre-scale scanlines. There is no evidence that aqueous fluids flowed through the fault-joint network in the form of mineral fill or alteration selvages around fractures. The distances between cataclasite-bearing fractures and dyke margins are mostly asymmetric and highly variable. An exception is the pair of 3 cm wide cataclasite zones that are symmetrically located to either side of the dyke, as shown in Figure 9b. These cataclasite zones lie ~30 cm to either side of the dyke and were not intruded by magma.

The metre-scale scanline results show a more pronounced contrast in fracture intensity than the decametre scanline data, due to a proportion of the fracture population being below the resolution of the digital data. The results show 3.5 times higher average fracture intensity within the dyke swarm corridor than on the northern and southern margins of the study area (Fig. 4). The average fault-joint intensity for

host rock measured within the dyke swarm corridor is 5.7 fractures per metre. Along scanlines of the same orientation outside the dyke swarm corridor, fracture intensity is 1.7 fractures per metre.

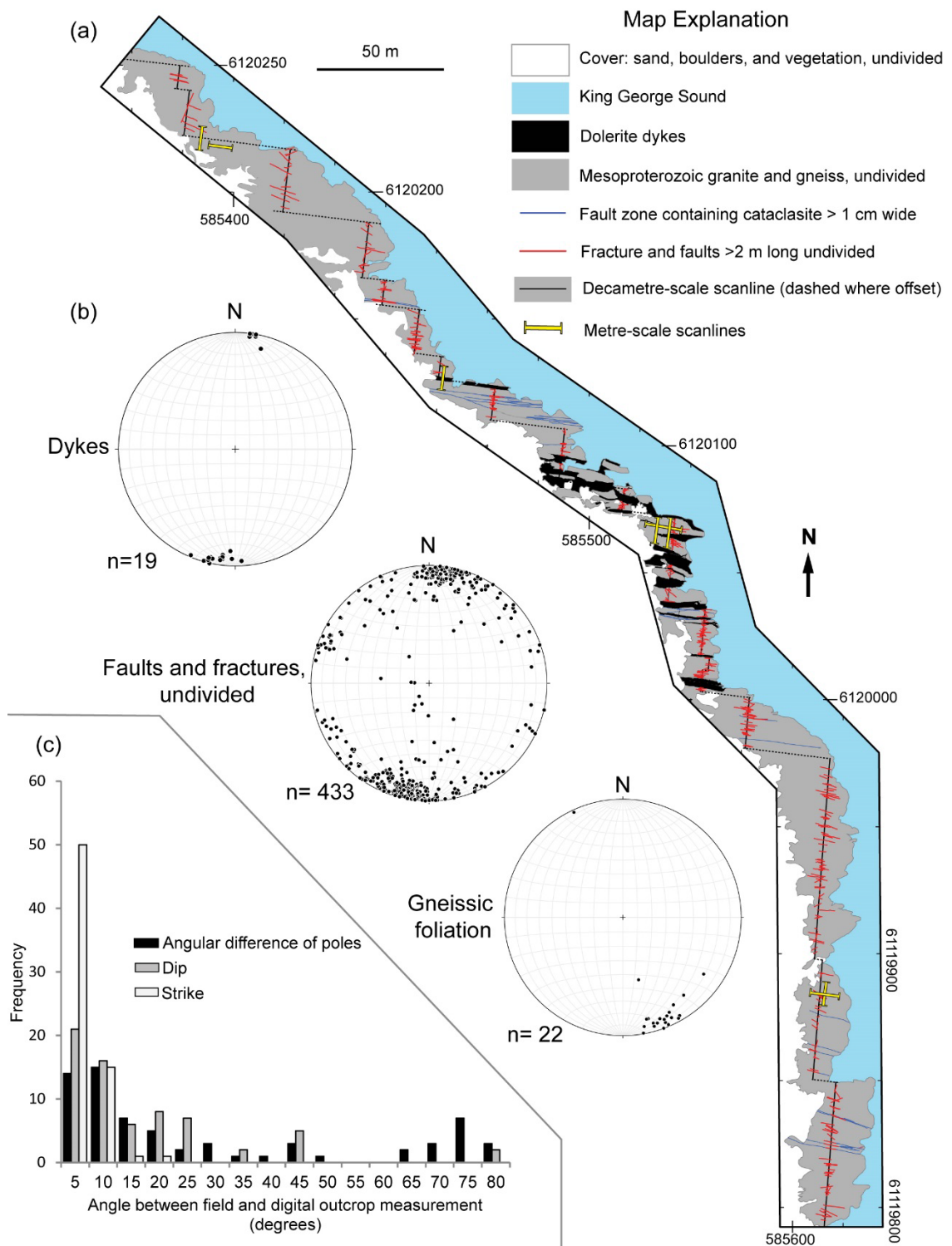


Figure 4 Scanline configuration and structural data derived from the photogrammetric model. (a) Simplified map of Vancouver Peninsula study area, showing fracture network, dykes, and locations of both decametre- and metre-scale scanlines. (b) Equal area lower hemisphere stereonet of poles to planes extracted from the digital outcrop model along decametre-scale scanline. The data show a main population cluster of WNW-striking, steeply-dipping fractures which are parallel to the dyke swarm. Within the fracture data, the girdle distribution that plunges steeply SW is defined by shallow-dipping exfoliation joints. Foliation within gneissic host rock domains is SW-striking and steeply dipping. (c) Histogram comparison of compass-clinometer measurements with digital outcrop measurements of individual structures (n=67), showing 1) The angular difference between poles to planes (black), 2) Difference in the dip component (dark grey), 3) Difference in the strike component (light grey). Strike measurements lie within measurement error whereas dip measurements have much larger discrepancies. This poor agreement results from false dip measurements for structures defined by points with high collinearity.

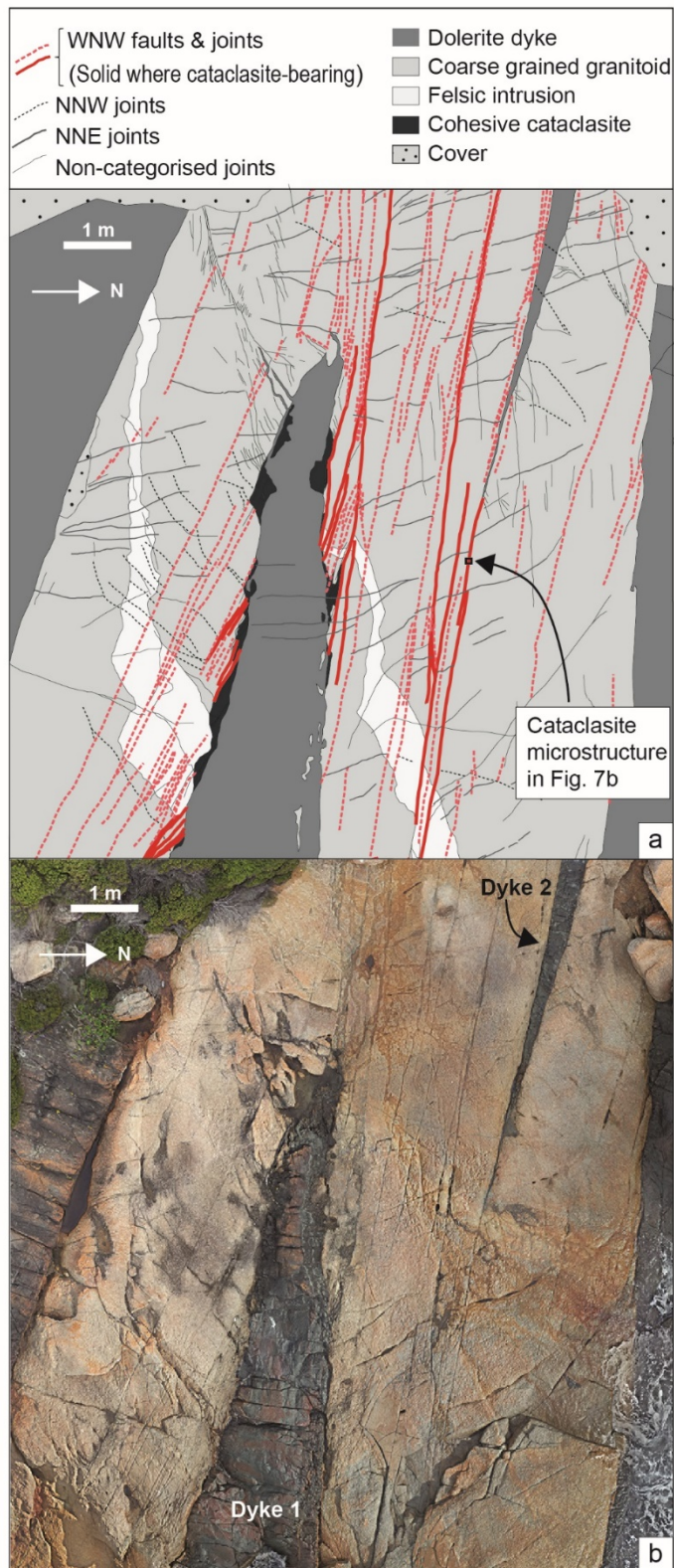


Figure 5 Representative geological map and orthorectified image of the same area, showing the distribution of faults and joints around the tips and margins of several dykes. (a) Dykes labelled 1 and 2 both intrude along pre-existing faults with up to ~4 metres of sinistral displacement. Faults were distinguished in the field on the basis of cataclasite fill. WNW-striking faults and joints comprise the earliest fracture population. Northerly striking joints are younger than the dykes and locally abut WNW-striking fractures (b) The orthoimage shows the density of fracture and amount of comminuted material adjacent to dykes and at the tips is highly variable. Notably absent are zones of finely comminuted material predicted by fluid mechanical models of dyke-induced damage (e.g. Mériaux et al., 1999).

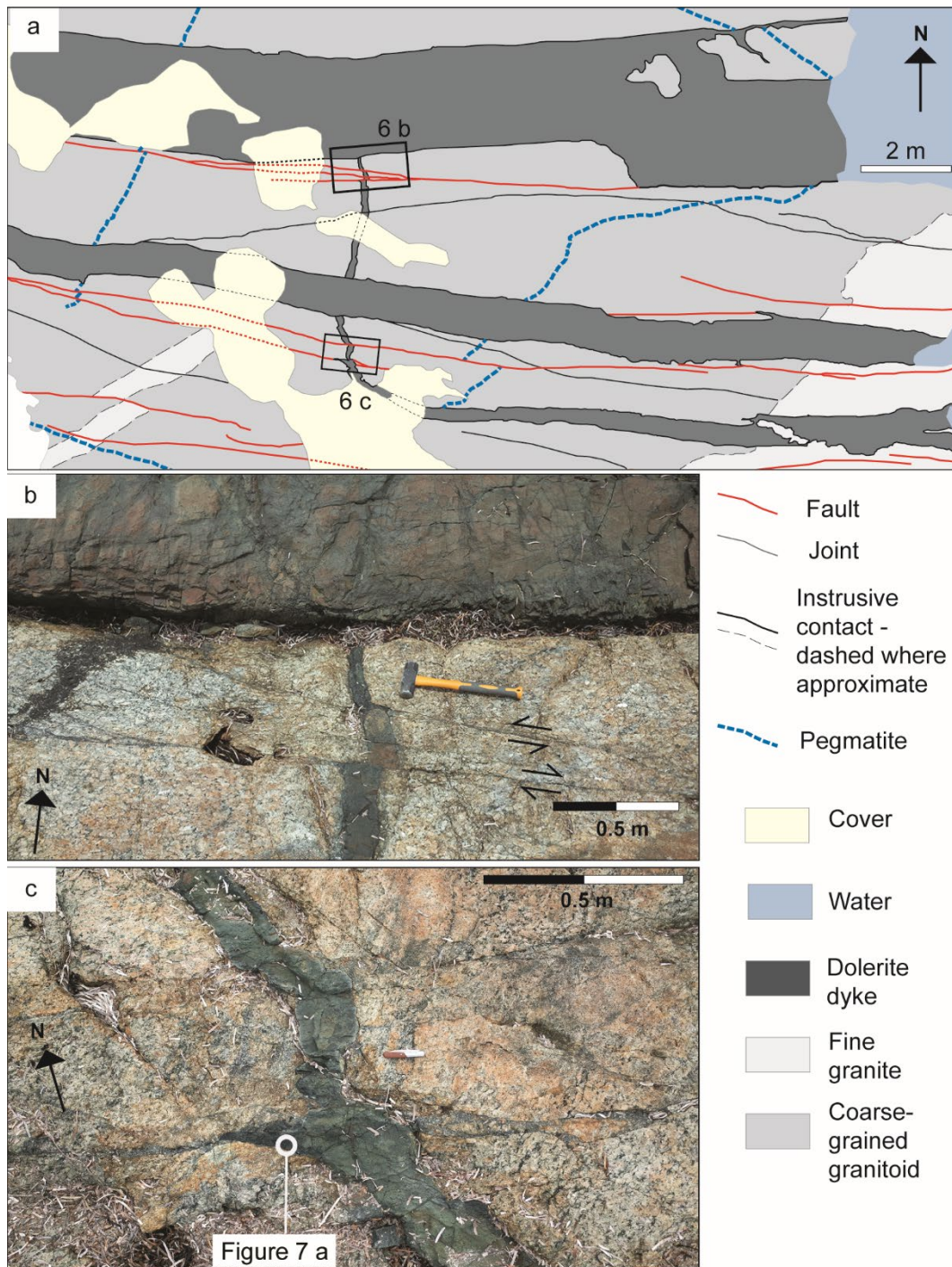


Figure 6 Cross-cutting relations show that faulting is coeval with dyke emplacement, preceding and accompanying at least the early stages of intrusion in this example. (a) Detailed geologic map showing WNW-striking faults that are near parallel to the main strike of the dyke swarm and which cross cut the tip of an early-formed dyke that curves north. This same fault set appears to be later intruded by the thick dyke at the top of the map. (b) Photo of the cross cutting relationship in outcrop. (c) The same north-curving dolerite dyke intrudes a cataclasite lens along a WNW-striking fault, demonstrating the opposite fault-dyke timing relationship to that in (b).

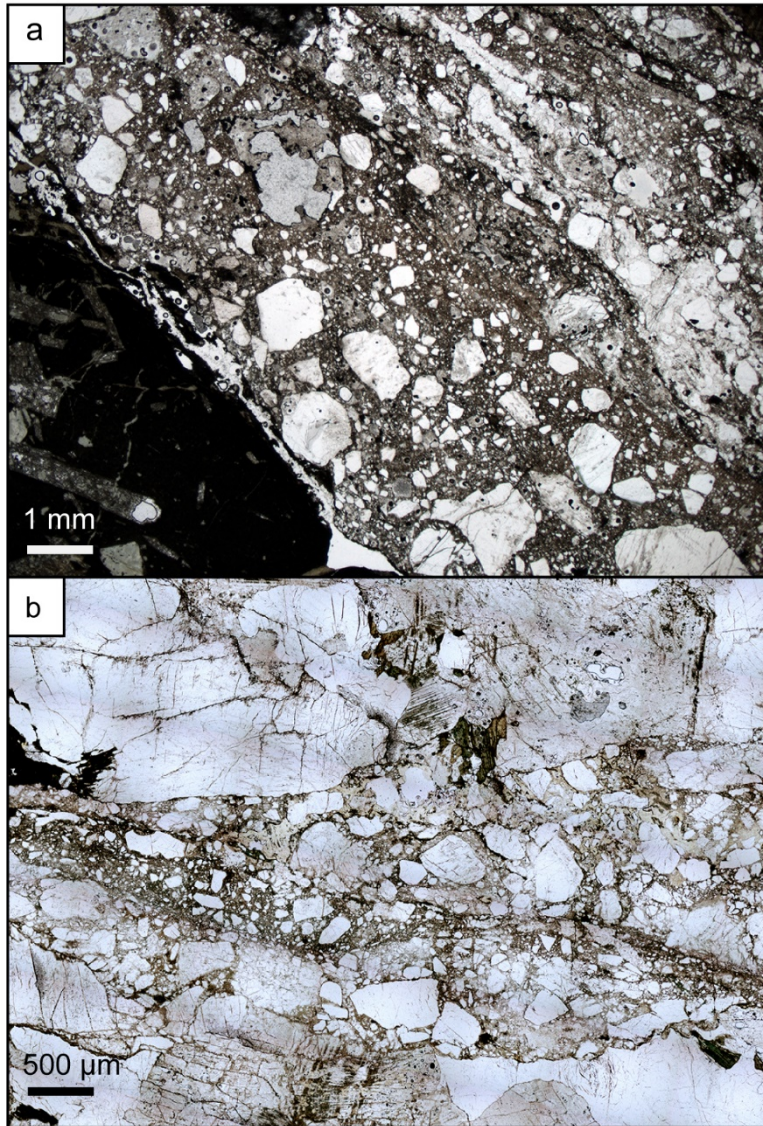


Figure 7 Cataclasite with clasts comprised of orthoclase and quartz. Bands of comminuted cataclasite and rotated wall rock fragments indicate that fractures in the host rock can accommodate shear. (a) Porphyritic dolerite chilled against cataclasite consisting entirely of wall rock fragments. Sample location shown in Figure 6 c (b) Narrow fault zone sampled ahead of the blade shaped dyke shown in Figure 5 a. Gouge and ultracataclasite occur in a narrow band at the core of the fault zone.

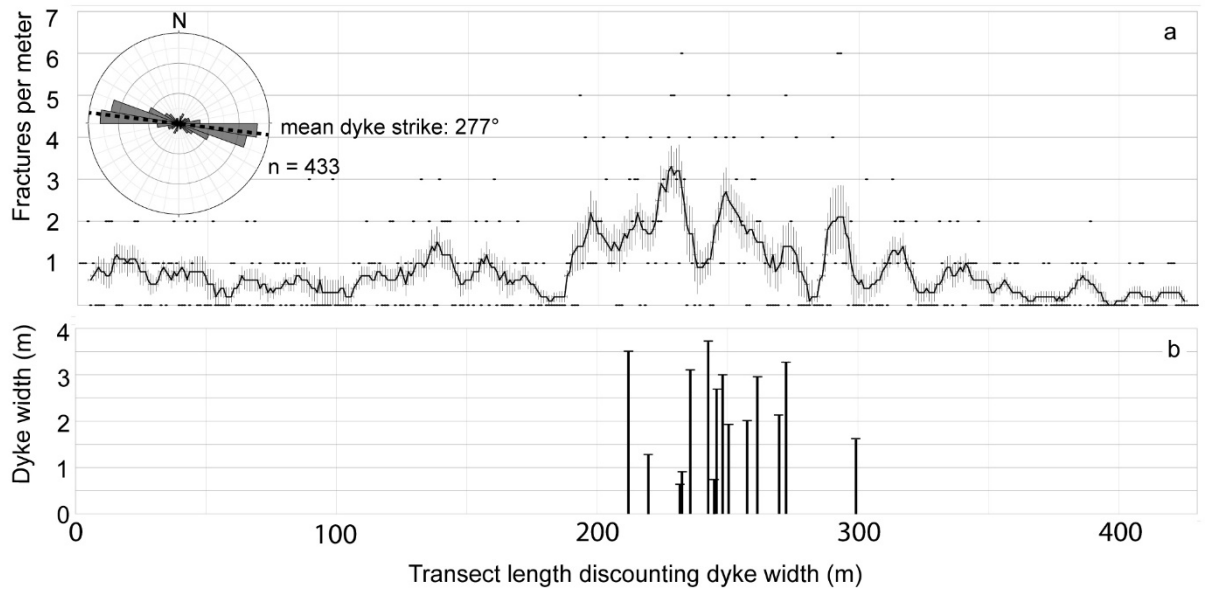


Figure 8 Swarm-wide fault-fracture intensity relative to dyke segment position. The scanline positions are plotted on the horizontal axes in (a) and (b) with respect to total host rock length. The aperture of each dyke segment has been removed from the scanline in order to analyse pre-dyke fracture intensity in the host rock. (a) Fractures per meter (black dots) for fractures and faults striking between 080° and 120°, moving average of fracture intensity over 5 m intervals (black line), showing variance (grey vertical lines). The rose diagram shows a subset of fractures used in fracture intensity analysis (grey petals), the young abutting joint set not analysed (white petals) and the mean dyke strike (black dashed line). (b) Positions of dyke segments (x axis) plotted against aperture (y axis) show the swarm to be comprised of similarly-sized dykes occupying a 90 m wide corridor.

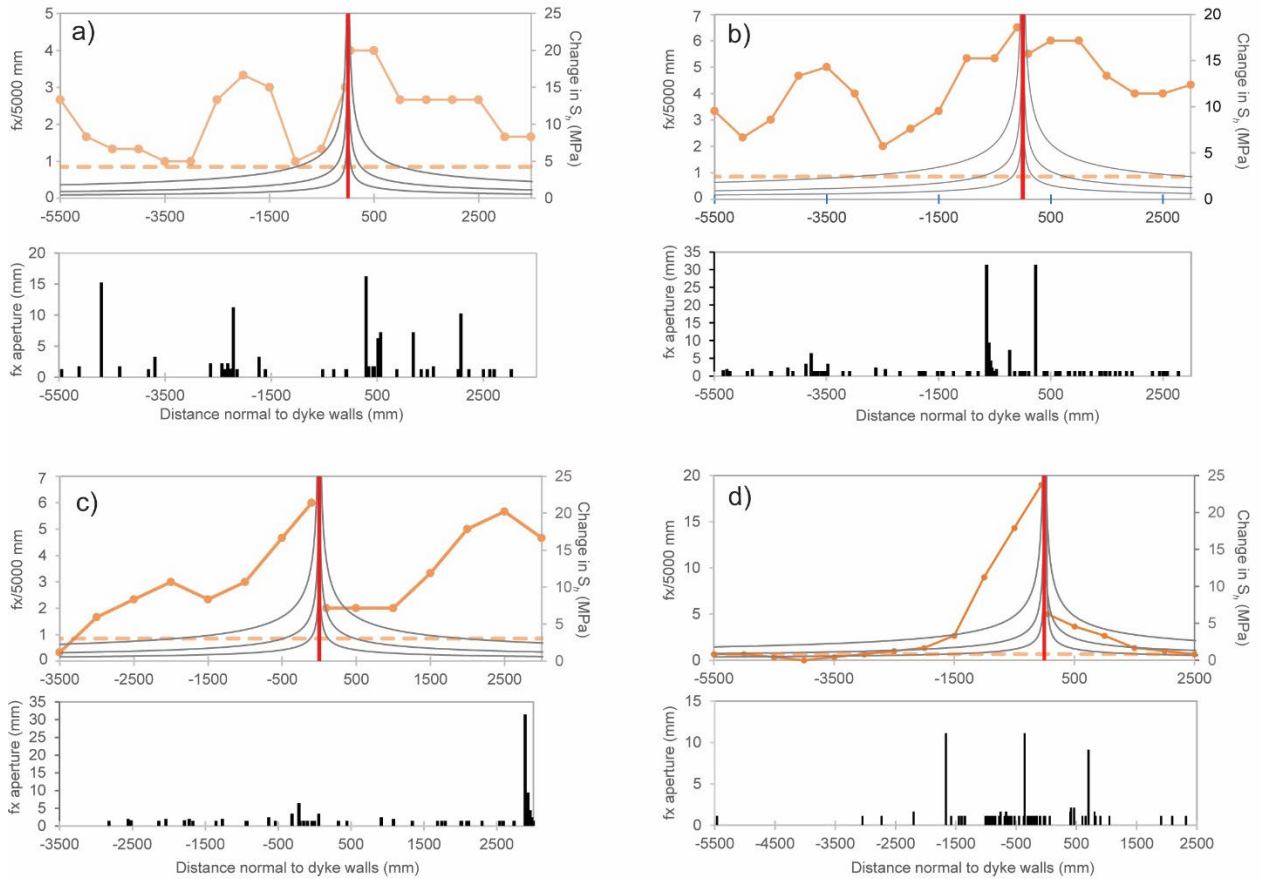


Figure 9 Metre-scale scanline results, showing fault-joint intensity (orange lines) and aperture data (black bars) with respect to dyke position (red line). The background fracture intensity (orange dashed line) is derived from similarly-oriented scanlines outside the dyke swarm corridor. The predicted increase in horizontal tensile stress normal to the dyke plane for net driving pressures of 1, 2, and 4 Mpa are computed according to Equation 1. Dyke-induced joints are predicted to occur adjacent to dyke walls within the region for with the stress change exceeds the tensile strength of the host rock, which ranges from 3 – 39 for granite (Bieniawski, 1984). The distribution of brittle deformation around the dykes, as indicated by the fracture intensity and aperture data, are a poor fit to the changes in tensile stress predicted by LEFM.

3.6 Discussion

Our results demonstrate that dyke parallel shear fracturing was a critical component of the dyke-emplacment process at the Vancouver Peninsula locality. In this discussion, we first outline the importance of our observations for models of fracture zone development around dykes, before highlighting the implications for dyke emplacement mechanisms in relation to recent geophysical observations of dyke-related seismicity at Upptyppingar, Iceland.

3.6.1 *Dyke-induced fracture zones*

The spatial and geometric distribution of fracture in the Albany dyke corridor is unlike the fracture networks which comprise so-called damage zones developed around faults that are not associated with dyke intrusion. Fault-induced damage is commonly organised around a zone of highest strain, typically dominated by gouge or cataclasite and referred to as the fault core (Cowie and Scholz, 1992). The intensity of macro- and microfractures that comprise the damage zone, is highest adjacent to the fault core, decaying exponentially with distance away from it (Scholz et al., 1993; Mitchell and Faulkner, 2009). In contrast, the distribution of macrofracture intensity across the Albany dyke corridor lacks comparable organisation around high strain zones (Fig. 8). Nor is there evidence for a large fault that could be responsible for the broad zone of damage. Instead, we suggest the relatively broad (90 m) corridor of elevated fracture intensity is related to the emplacement of the dyke swarm itself.

The results suggest that deformation associated with the passage of individual dyke tips was accommodated by a precursor network of faults and joints. Key evidence for this timing relationship is the ubiquitous presence of chilled margins developed within dykes in contact with fault rocks and the absence of comminuted mafic material within fault zones. Furthermore, it is argued that cataclasite zones along which dykes have intruded were consolidated enough to resist significant thermo-mechanical erosion at the time of magma emplacement. For these reasons, the formation of cataclasites within the dyke swarm corridor cannot be attributed to the passage of individual dyke tips. The dyke swarm corridor is characterised by many small faults, parallel with the dykes, with thin, well-consolidated cataclastic cores that are mostly not infiltrated by magma. This implies an increase in yield strength following failure (strain hardening), such that subsequent deformation is accommodated by the formation of new faults rather than reactivation. These findings call into question the assumption of Mériaux et al. (1999) that dyke tips propagate through process zones with zero elastic strength. Instead of centering on individual dykes, the distribution of fractures and intense host rock degradation shows a relationship to the dyke swarm as a whole. These observations require a reassessment of models of dyke-induced fracture to better understand swarm emplacement.

3.6.2 *Conceptual model of dyke-related damage corridors*

The LEFM model of Delaney et al. (1986) predicts the opening of tensile fractures ahead of, and to either side of propagating dyke tips. While this model could partly explain the anomalous dyke-parallel joint density observed across the Albany dyke corridor, it does not predict the dyke-parallel shear observed in this outcrop study and in the seismological study of White et al. (2011).

One potential explanation for dyke-parallel shear arises from recent insights derived from damage mechanics that address the non-linear elastic response of a fractured volume of rock to remotely applied stress. Changes in bulk elastic properties of rock accompany damage zone development in the form of macro- and microfractures (e.g. Scholz et al., 1993). In particular, there is a reduction of Young's modulus accompanied by an increase in Poisson's ratio, as compared with rock outside the damage zone. These changes in bulk elastic properties can result in local reorientation of remotely applied stress within the damage zone, as modelled by Faulkner et al. (2006) for a damage zone with increasing fracture density toward a fault core.

Here we present a model for dyke-parallel shear that is initiated by tensile failure and is then reactivated and repeatedly modified during dyke propagation and emplacement. Early fractures within the Albany dyke corridor formed by a slightly different mechanism than the fault-induced fractures described by Faulkner et al. (2006), but the effect on the bulk elastic properties of the rock will nevertheless be similar (Fig. 10a). Within the Albany dyke corridor, dyke-induced remote tensile failure leads to elevated fracture intensity, consistent with the mechanism of Delaney et al. (1986). We suggest that repeated cycles of loading, resulting from the successive emplacement of dykes and related episodes of joint development, had a cumulative effect on the elastic properties of the dyke corridor.

The increase in fracture intensity and widening of the dyke swarm corridor are the result of multiple phases of intrusion (Fig. 10b), with dyke-parallel shear becoming possible in the later phases. Following Faulkner et al. (2006) the far field principle stresses would undergo local rotation within the densely fractured rocks of the Albany dyke corridor (Fig. 10a). Working on the assumption that both dykes and dyke-related joints should lie in the plane of maximum regional stress and open in the direction of minimum regional stress, a rotation of only $\sim 15^\circ$ of the principal stress directions could lead to a switch from tensile to shear failure along the joint planes (Jaeger & Cook, 1979). The observation that the propagation paths of some dyke tips were captured by the pre-existing faults suggests an advanced phase of dyke corridor development, depicted in the fourth panel of Figure 10b that is consistent with field observations (Figs. 5 and 6a). In summary, we suggest that fractures ahead of propagating dykes are first initiated by tensile failure and are then reactivated under shear failure due to the concomitant change in host rock elastic properties that results in local stress rotation.

3.6.3 Implications for interpretation of dyke-induced seismicity

We can link the observations of the exhumed fault-joint corridor at Albany to concepts proposed based on seismological observations from 2007-2008 Upptyppingar dyke emplacement event. We

suggest that the migration of dyke-parallel seismicity both up-dip and down-dip, along with the remarkably consistent fault plane solutions during the Upptyppingar event, result from reactivation of dyke-parallel fractures in the host rocks. Despite probable significant differences in emplacement depth and orientation within the regional stress field, the seismological observations can be understood in similar terms to dyke-proximal deformation proposed for the Albany dyke swarm (Fig. 10). Of the three mechanisms proposed by White et al. (2011), the outcrop observations from the Albany study area confirm that dyke-parallel faults can form in the host rocks of intruding dykes, whereas we found no evidence for the alternative mechanisms of rupture of solidified plugs, or shear failure in the plane of magma injection. We infer that the Upptyppingar dyke was emplaced into a pre-existing fracture corridor possibly originating from Mode I failure during previous dyke emplacement events. The emplacement of a relatively narrow dyke into a comparatively broad, pre-existing fracture corridor further explains the cloud of seismicity that defines an inclined tabular zone (White et al. 2011).

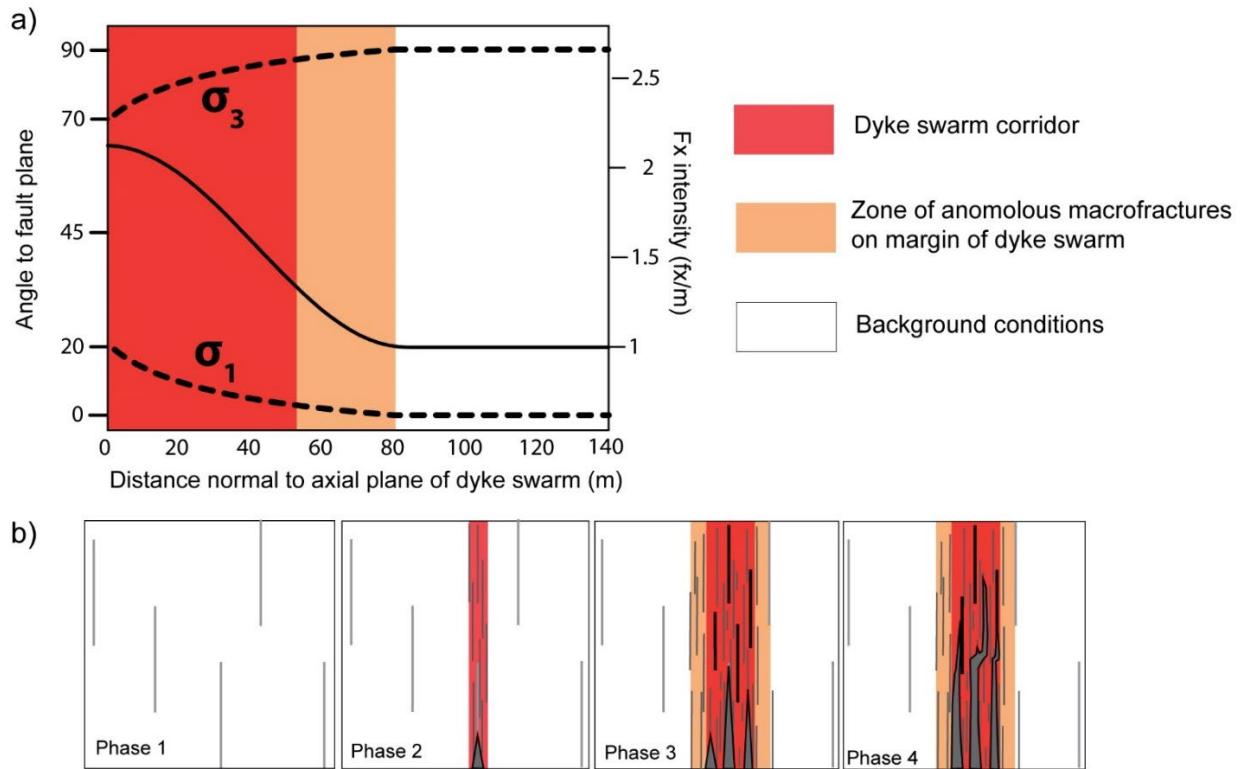


Figure 10 Conceptual model of stress rotation leading to dyke-parallel shear within the zone of intense macrofracturing and decreased elastic strength. a) Plot of the suggested relationship between stress orientation and fracture intensity in terms of distance normal to the axial plane of the dyke swarm (x-axis). The trajectories of the maximum (σ_1) and minimum (σ_3) principle regional stresses (heavy dashed lines) are plotted on the left-hand Y axis. Fracture intensity is plotted on the right-hand Y-axis (solid black line). This model assumes maximum fracture intensity and minimum elastic strength occur at the middle of the dyke swarm. Following the findings of Faulkner et al. (2006), rotation of remotely applied stress increases toward this region of lowest elastic strength, corresponding to $x=0$. b) Schematic illustration of dyke-induced jointing and formation of a dyke swarm corridor. Dyke propagation direction is toward the top of the figure. Phase 1 is the background condition with sparsely distributed joints (gray lines). In Phase 2, dyke-induced tensile failure occurs ahead of the propagating tip, as described by Delaney et al. (1986). Phase 3 correlates with the conditions shown in (a), such that the dyke swarm corridor and adjacent region has become sufficiently weakened by repeated cycles of dyke-induced tensile failure to result in stress rotation and the reactivation of some pre-existing joints as faults (heavy black lines). In Phase 4 magma invades the established fault-joint network, resulting in the existing relationships observed by this study.

3.7 Conclusion

This study provides high-resolution spatial constraints on macrofracture development around dykes and provides a potential analogue for dyke-related deformation. Fracture intensity data from the exhumed Albany dyke swarm reveal that fault-joint intensity, characterised by distributed small faults and joints, increases toward the dyke swarm and is 2.2 ± 0.7 times greater than the background fracture intensity. However, at the metre-scale, fault-joint intensity within the dyke swarm corridor is not clearly organised around individual dykes. Strain hardening has resulted in widely distributed faults that have only small displacements. In this manner, the fracturing and faulting associated with intrusions differs from the development of damage around amagmatic faults, which normally involves a clear increase in fracture intensity toward a fault core.

Fracturing precedes and accompanies dyke swarm formation, both as opening mode tensile failure and shear failure on planes that are parallel to the orientation of the dykes, within the host rocks around the dykes. We suggest that tensile failure occurs ahead of propagating dykes, as joints, which are then reactivated under shear as the dykes continue to propagate due to changing host rock elastic properties and local stress reorientation. Our outcrop observations and this model of dyke parallel faulting contrast with conventional understanding of dyke-fault interactions, which normally invokes a fault angle of $\sim 30^\circ$ to the dyke plane.

Our finding that rupture occurs on faults parallel to the dykes and that host rock damage preceded magma intrusion is consistent with seismological and geodetic observations from dyke emplacement events in Iceland in 2006-2007 and 2014-2015. Our high-resolution outcrop study demonstrates that shear failure occurs in the host rocks around a dyke swarm, rather than by rupture of solidified plugs within dykes.

Acknowledgements

This work was funded by a CSIRO Top Up Scholarship awarded to G. Dering. We are grateful to Dr. Eric Tohver for his assistance in the field. The manuscript was significantly strengthened by excellent reviews from Robert White and one anonymous reviewer. The authors acknowledge the financial support of the ARC grants CE110001017, FT110100241, and LP120100668. This is contribution 1210 from the ARC Centre of Excellence for Core to Crust Fluid Systems (<http://www.ccfs.mq.edu.au>).

8. References

- Anderson, E., 1951. *The Dynamics of Faulting and Dyke Formation with Applications to Britain*. Oliver and Boyd, Edinburgh.
- Aoki, Y., Segall, P., Kato, T., Cervelli, P., Shimada, S., 1999. Imaging magma transport during the 1997 seismic swarm off the Izu Peninsula, Japan. *Science* 286, 927-930.
- Armstrong, P., 1985. *Charles Darwin in Western Australia*. Univ. of Western Australia Press, Nedlands.
- Bai, T., Pollard, D.D., 2000. Fracture spacing in layered rocks: a new explanation based on the stress transition. *J. Struct. Geol.* 22, 43-57.
- Bemis S.P., Micklethwaite S., Turner D., James M.R., Akciz S., Thiele S.T., Bangash H.A., 2014. Ground-based and UAV-based photogrammetry: A multi-scale, high-resolution mapping tool for structural geology and paleoseismology. *J. Struct. Geol.* 69, 163-78.
- Brenna, M., Gee, M.A.M., 2014. Dyke-diatreme transition in monogenetic volcanoes: insights from the Hillier Bay volcanic complex, Western Australia. *Bull. Volcanology* 76, 853-866.
- Broek, D., 1986. *Elementary engineering fracture mechanics*, Martinus Nijhoff, Dordrecht.
- CloudCompare (version 2.9beta) [GPL software]. (2017). Retrieved from <http://www.cloudcompare.org/>
- Cowie, P.A., Scholz, C.H., 1992. Displacement-length scaling relationship for faults: Data synthesis and discussion. *J. Struct. Geol.* 14, 1149-1156.
- Delaney, P.T., Pollard, D.D., 1981. Deformation of host rocks and flow of magma during growth of Minette dikes and breccia-bearing intrusions near Ship Rock, New Mexico, *Geological Survey Professional Paper* 1202.
- Delaney, P.T., Pollard, D.D., Ziony, J.I., McKee, E.H., 1986. Field relations between dikes and joints - emplacement processes and paleostress analysis. *J. Geophys. Res., Solid Earth* 91, 4920-4938.
- Eisenbeiss, H., 2009. *UAV photogrammetry*, PhD Dissertation, Institut für Geodesie und Photogrammetrie. ETH-Zürich, Zürich, Switzerland.

- Faulkner D.R., Mitchell T.M., Healy D., Heap M.J., 2006. Slip on 'weak' faults by the rotation of regional stress in the fracture damage zone. *Nature* 444 (7121), 922-925.
- Favalli, M., Fornaciai, A., Isola, I., Tarquini, S., Nannipieri, L., 2012. Multiview 3D reconstruction in geosciences. *Computers & Geosciences* 44, 168-176.
- Forslund, T. and Gudmundsson, A., 1992. Structure of Tertiary and Pleistocene normal faults in Iceland. *Tectonics*, 11(1), 57-68.
- Gudmundsson, A., 2011a. *Rock fractures in geological processes*. Cambridge University Press.
- Gudmundsson, A., 2011b. Deflection of dykes into sills at discontinuities and magma-chamber formation. *Tectonophysics* 500, 14.
- Harris, L.B., Li, Z.X., 1995. Paleomagnetic dating and tectonic significance of dolerite intrusions in the Albany Mobile Belt, Western-Australia. *Earth Planet. Sci. Lett.* 131, 143-164.
- Hill, D.P., 1977. A model for earthquake swarms. *J. Geophys. Res.* 82, 1347-1352.
- Huang, Q., Angelier, J., 1989. Fracture spacing and its relation to bed thickness. *Geological Magazine* 126, 355-362.
- Jaeger, J.C., Cook, N.G.W., 1979. *Fundamentals of rock mechanics*, Chapman and Hall, New York.
- Mériaux, C., Lister, J.R., Lyakhovsky, V., Agnon, A., 1999. Dyke propagation with distributed damage of the host rock. *Earth Planet. Sci. Lett.* 165, 177-185.
- Minson, S.E., Dreger, D.S., Bürgmann, R., Kanamori, H., Larson, K.M., 2007. Seismically and geodetically determined non-double-couple source mechanisms from the 2000 Miyakejima volcanic earthquake swarm. *J. Geophys. Res., Solid Earth* 112 (B10308).
- Mitchell, T., Faulkner, D., 2009. The nature and origin of off-fault damage surrounding strike-slip fault zones with a wide range of displacements: a field study from the Atacama fault system, northern Chile. *J. Struct. Geol.* 31, 802-816.
- Ortega, O.J., Marrett, R.A., Laubach, S.E., 2006. A scale-independent approach to fracture intensity and average spacing measurement. *AAPG Bulletin* 90, 193-208.
- Passarelli, L., Rivalta, E., Cesca, S., Aoki, Y., 2015. Stress changes, focal mechanisms, and earthquake scaling laws for the 2000 dike at Miyakejima (Japan). *J. Geophys. Res., Solid Earth* 120, 4130-4145.

- Rivalta, E., Taisne, B., Bungler, A.P., Katz, R.F., 2015. A review of mechanical models of dike propagation: Schools of thought, results and future directions. *Tectonophysics* 638, 1-42.
- Roman, D.C., Cashman, K.V., 2006. The origin of volcano-tectonic earthquake swarms. *Geology* 34 (6), 457-460.
- Rubin, A.M., Gillard, D., 1998. Dike-induced earthquakes: Theoretical considerations. *J. Geophys. Res., Solid Earth* 103, 10017-10030.
- Rubin, A.M., Gillard, D., Got, J.L., 1998. A reinterpretation of seismicity associated with the January 1983 dike intrusion at Kilauea Volcano, Hawaii. *J. Geophys. Res., Solid Earth* 103, 10003-10015.
- Rubin, A.M., Pollard, D.D., 1988. Dike-induced faulting in rift zones of Iceland and Afar. *Geology* 16 (5), 413-417.
- Scholz, C.H., Dawers, N.H., Yu, J.Z., Anders, M.H., Cowie, P.A., 1993. Fault growth and fault scaling laws: Preliminary results. *J. Geophys. Res., Solid Earth* 98, 21951-21961.
- Scibiorski, E., Tohver, E., Jourdan, F., 2015. Rapid cooling and exhumation in the western part of the Mesoproterozoic Albany-Fraser Orogen, Western Australia. *Precambrian Res.* 265, 232-248.
- Segall, P., 2013. *Volcano deformation and eruption forecasting*. Geological Society, London, Special Publications 380 (1), 85-106.
- Shelly, D.R., Hill, D.P., 2011. Migrating swarms of brittle-failure earthquakes in the lower crust beneath Mammoth Mountain, California. *Geophys. Res. Lett.* 38 (20), L20307.
- Sigmundsson, F., Hooper, A., Hreinsdóttir, S., Vogfjörð, K.S., Ófeigsson, B.G., Heimisson, E.R., Dumont, S., Parks, M., Spaans, K., Gudmundsson, G.B., Drouin, V., Árnadóttir, T., Jónsdóttir, K., Gudmundsson, M.T., Högnadóttir, T., Fridriksdóttir, H.M., Hensch, M., Einarsson, P., Magnússon, E., Samsonov, S., Brandsdóttir, B., White, R.S., Ágústsdóttir, T., Greenfield, T., Green, R.G., Hjartardóttir, A.R., Pedersen, R., Bennett, R.A., Geirsson, H., La Femina, P.C., Björnsson, H., Pálsson, F., Sturkell, E., Bean, C.J., Mollhoff, M., Braiden, A.K., Eibl, E.P.S., 2015. Segmented lateral dyke growth in a rifting event at Bárðarbunga volcanic system, Iceland. *Nature* 517 (7533), 191-195.
- Smith, M.W., Carrivick, J.L., Quincey, D.J., 2016. Structure from motion photogrammetry in physical geography. *Progress in Physical Geography* 40 (2), 247-275.

- Spaggiari, C. V., Kirkland, C. L., Smithies, R. H., Wingate, M. T. D., and Belousova, E. A., 2015. Transformation of an Archean craton margin during Proterozoic basin formation and magmatism; the Albany-Fraser Orogen, Western Australia: *Precambrian Research*, 266, 440-466.
- Thiele, S.T., Micklethwaite, S., Bourke, P., Verrall, M., Kovesi, P., 2015. Insights into the mechanics of en-echelon sigmoidal vein formation using ultra-high resolution photogrammetry and computed tomography. *J Struct. Geol.* 77, 27-44.
- Toda, S., Stein, R.S., Reasenber, P.A., Dieterich, J.H. and Yoshida, A., 1998. Stress transferred by the 1995 $M_w = 6.9$ Kobe, Japan, shock: Effect on aftershocks and future earthquake probabilities. *J. Geophys. Res., Solid Earth*, 103 (B10), 24543-24565.
- Toda, S., Stein, R.S., Sagiya, T., 2002. Evidence from the AD 2000 Izu islands earthquake swarm that stressing rate governs seismicity. *Nature* 419 (6902), 58-61.
- Ukawa, M., Tsukahara, H., 1996. Earthquake swarms and dike intrusions off the east coast of Izu Peninsula, central Japan. *Tectonophysics* 253, 285-303.
- Vollgger S.A., Cruden A.R., 2016. Mapping folds and fractures in basement and cover rocks using UAV photogrammetry, Cape Liptrap and Cape Paterson, Victoria, Australia. *J. Struct. Geol.* 85,168-87.
- White, R.S., Drew, J., Martens, H.R., Key, J., Soosalu, H., Jakobsdóttir, S.S., 2011. Dynamics of dyke intrusion in the mid-crust of Iceland. *Earth and Planet. Sci. Lett.* 304, 300-312.

Appendix 3.1

Aerial image acquisition and processing

Aerial images were captured in JPEG format using a downward-facing Ricoh GR 2 digital camera attached to a DJI Phantom 2 quadcopter. Photogrammetric processing employed Agisoft Photoscan Pro v. 1.2.0 for Windows at the Pawsey Computing and Visualisation Lab (iVEC) at the University of Western Australia.

Photogrammetric model validation procedure

The photogrammetric model 3D geometry and location was constrained by an array of 30 ground control points surveyed with a Leica TS06 total station. Half of the ground control points were used to georectify the dense point cloud, whereas the other half were reserved to double-check the accuracy of the orthorectified image and DEM derived from the dense point cloud (referred to here as validation points). Ground control locations were measured with a minimum precision of ± 4 cm. The small uncertainty on the precision of the ground control locations arises from the propagation of measurement error to second and third base station locations. These additional base station locations were required due to lack of line-of-sight from a single base station to all 30 ground control points along an outward-curving coastline.

The 15 validation points were used to assess the geometric accuracy of the photogrammetric reconstruction by measuring the Euclidian distance between modelled ground control points and their field locations, as surveyed with the total station (Fig. 3b). Accurate photogrammetric models should yield small misfits between the arrays of modelled and measured points. The maximum measurable model accuracy is achieved for control point arrays with root mean square (RMS) error that is less than the measurement error of individual points. Our model approaches the maximum measurable spatial accuracy with a RMS error of 5.5 cm for the 15 validation points. This is close to the total station measurement error of ± 4 cm. Therefore, the geometry of the photogrammetric model is accurate and lies close to the uncertainty of the total station survey.

Further confidence in the spatial and geometric accuracy of the DEM and orthoimage comes from analysis of 15 ground control points used in the construction of the dense point cloud. These control points serve to both orient the dense cloud and constrain its geometry. Projections of these 15 points used for photogrammetric processing of the DEM and orthoimage yield an RMS error of 5.2 cm. The small (6%) reduction in error as compared with independent validation points arises from optimisation of the model geometry to fit these points used in the construction process. Therefore, the accuracy of the dense point cloud, DEM, and orthoimage are principally limited by measurement uncertainty of the ground control points. Any distortions in the model are too small to have any impact on the maps and structural measurements that we extract from these data in subsequent analyses.

Camera specifications	Sensor width (mm)	23.6
	Sensor height (mm)	15.7
	Sensor width - pixel count	4928
	Sensor height - pixel count	3264
	Focal length (mm)	18.3
	Sensor pixel length (um)	4.78
UAV survey	Ground speed (m/sec)	1.5
	Ground Sampling Distance (mm)	0.3
	Side overlap (image area %)	60
	Forward overlap (image area %)	50
	Area (m ²)	13340
	Altitude above sea level (m)	11.4
Photogrammetric model	Image count	1099
	Dense cloud point count	429357800
	Georeferencing points (count)	15
	Georeferencing point error (mm)	5.2 ± 1.4
	Validation points (count)	15
	Validation point error (mm)	5.5 ± 1.8
	Orthoimage resolution (mm/pixel)	3.5
	DEM resolution (mm/pixel)	7.0

Table 1 Camera specifications, aerial survey parameters, and photogrammetric model outputs. Validation and Georeferencing point error are reported as the mean and standard deviation.

	Station ID	Easting (UTM)	Northing (UTM)	Elevation (m)	Modelled misfit (m)
Validation point	GC2	585623.007	6119838.687	0.293	0.090
	GC4	585613.012	6119910.140	1.737	0.079
	GC6	585592.722	6119983.452	2.082	0.013
	GC17	585562.919	6120007.345	2.292	0.042
	GC16	585564.238	6120009.052	1.563	0.040
	01-08	585554.652	6120011.405	0.642	0.063
	01-14B	585556.506	6120016.801	0.474	0.038
	04-01	585554.922	6120036.550	0.921	0.036
	10-15	585546.666	6120065.394	1.455	0.049
	11-02	585550.723	6120068.320	0.674	0.040
	GC13	585398.458	6120214.862	1.947	0.065
	GC11	585423.328	6120185.292	2.368	0.055
	GC15	585472.616	6120121.934	1.405	0.066
	GC8	585518.136	6120088.900	2.254	0.053
	11-02	585550.723	6120068.320	0.674	0.060
Georeference point	GC1*	585612.122	6119803.235	0.034	0.059
	GC3	585607.998	6119874.603	1.243	0.022
	GC19	585615.000	6119948.000	1.500	0.032
	GC6B	585592.708	6119983.466	2.090	0.054
	GC17	585562.919	6120007.345	2.292	0.061
	GC18	585555.224	6120008.980	2.588	0.028
	01-07	585555.146	6120009.962	0.816	0.052
	01-11	585555.286	6120013.269	0.495	0.046
	02-07	585557.773	6120023.055	0.323	0.042
	10-01	585555.119	6120062.905	0.581	0.046
	10-11	585551.046	6120065.401	1.036	0.054
	10-11B	585541.655	6120070.659	1.552	0.056
	GC9	585498.429	6120109.953	1.906	0.050
	GC10	585449.299	6120147.333	1.453	0.045
	GC12	585377.985	6120191.835	10.830	0.050
GC14	585350.305	6120251.325	3.927	0.080	

*survey origin

Table 2 Ground control point locations measured by total station. The modelled misfit is the Euclidean distance from the measured total station location to the modelled location determined from the orthoimage and DEM. The modelled misfit data are shown in Fig. 3b. UTM zone is 50 south.

Appendix 3.2

Decametre scanline methodology

A scanline at the decametre scale captured the entire dyke swarm and surrounding bedrock in the digital dataset. The dyke swarm crosscuts host rocks in a ~90 m wide corridor, with continuous exposure ~180 m north and south of the dyke swarm (Fig. 4 a). The decametre scanline captures fault, joint, and dyke spacing orthogonal to the dyke swarm over a distance of 435 m. Structural orientation and spacing measurements captured all joints and faults with trace lengths ≥ 2 m that intersect the scanline. Precise measurement of fracture apertures from the orthorectified image was not possible due to variations in shadowing, weathering, and composition of fill (e.g. Fig. 3 a and c). Data resolution was approximately 9 mm (i.e. minimum measurable distance between features), which is three times the pixel size (3.5 mm) of the orthoimage.

Unfiltered decametre scanline results

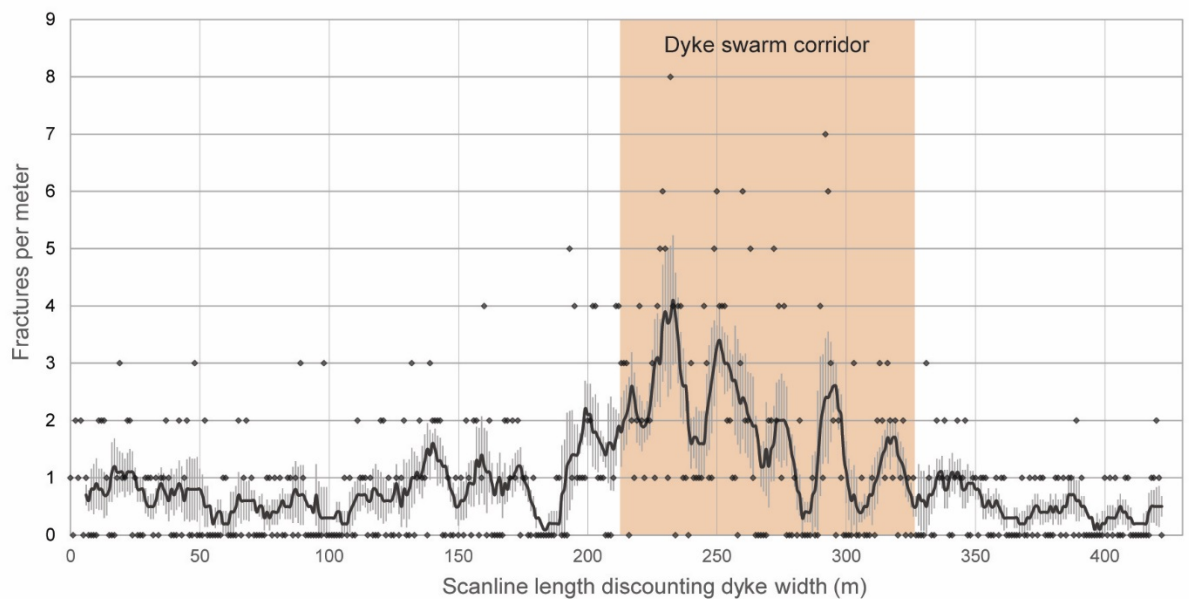


Figure A1 Intensity (fractures/m) of for all orientations of faults and joints greater than 2 m in length that are intersected by the scanline (n=433). The black line is a 5 m moving average of fault-joint intensity, with the standard error and 1 m fracture intensity data displayed following the same convention as Figure 8a. The shaded orange region shows the section of the scanline that is intersected by the dyke swarm.

Decametre scanline strike dispersion profile

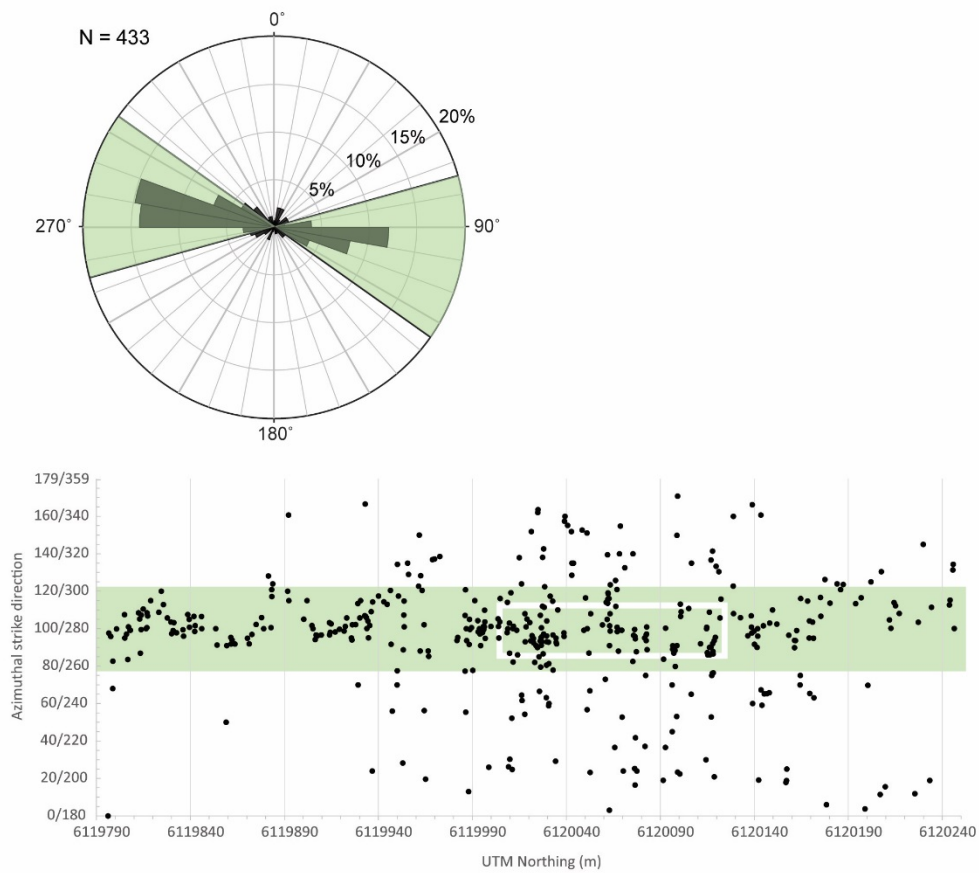


Figure A2 The spatial distribution of faults and joints (black dots) according to strike direction (y-axis). The position and strike direction of dyke swarm segments all fall within the white box. Data within the green shaded region are shown in Figure 8a (n=361). All data (n=433) are plotted on the scanline included in Figure S1.

Metre-scale scanline results

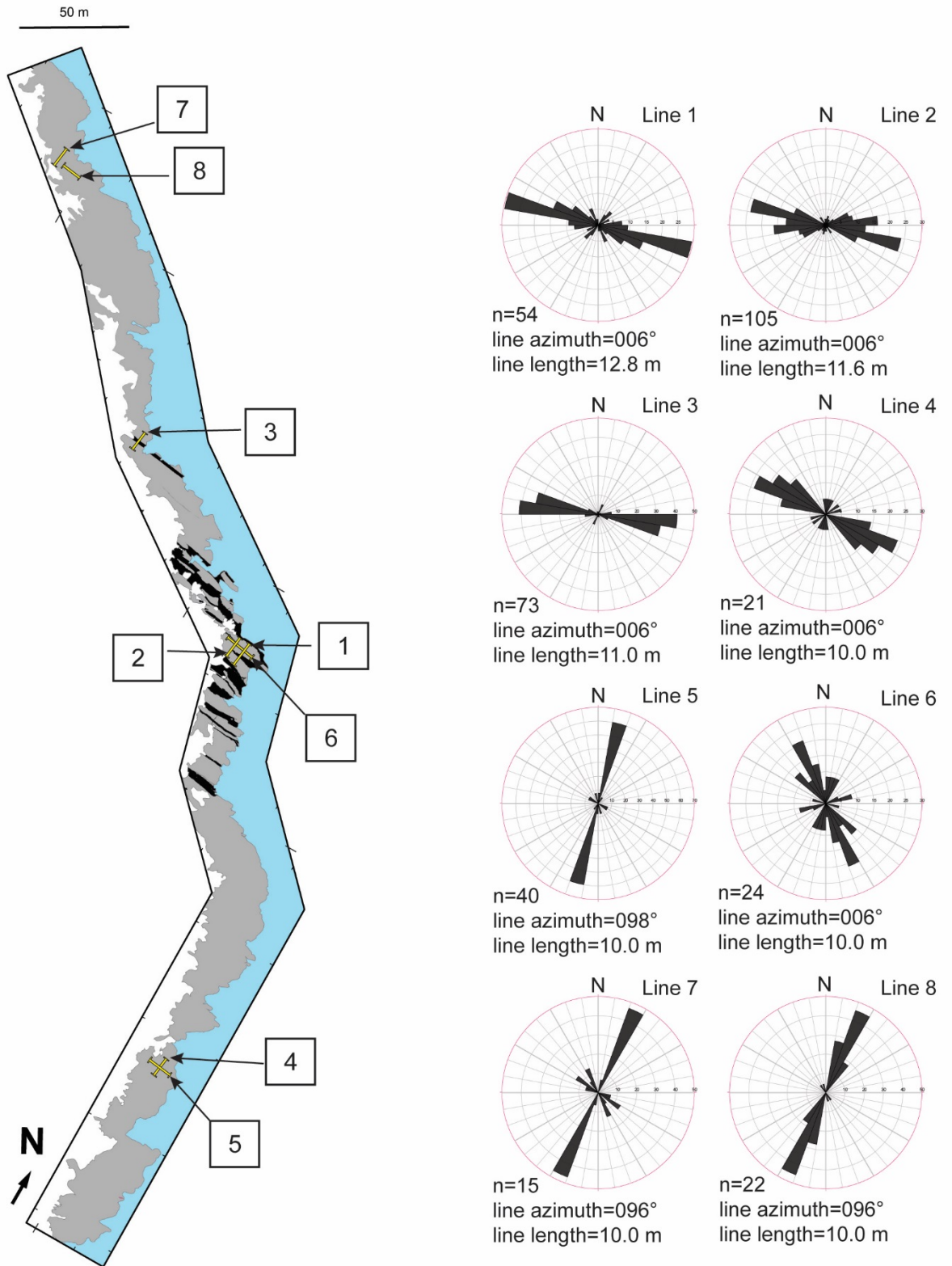
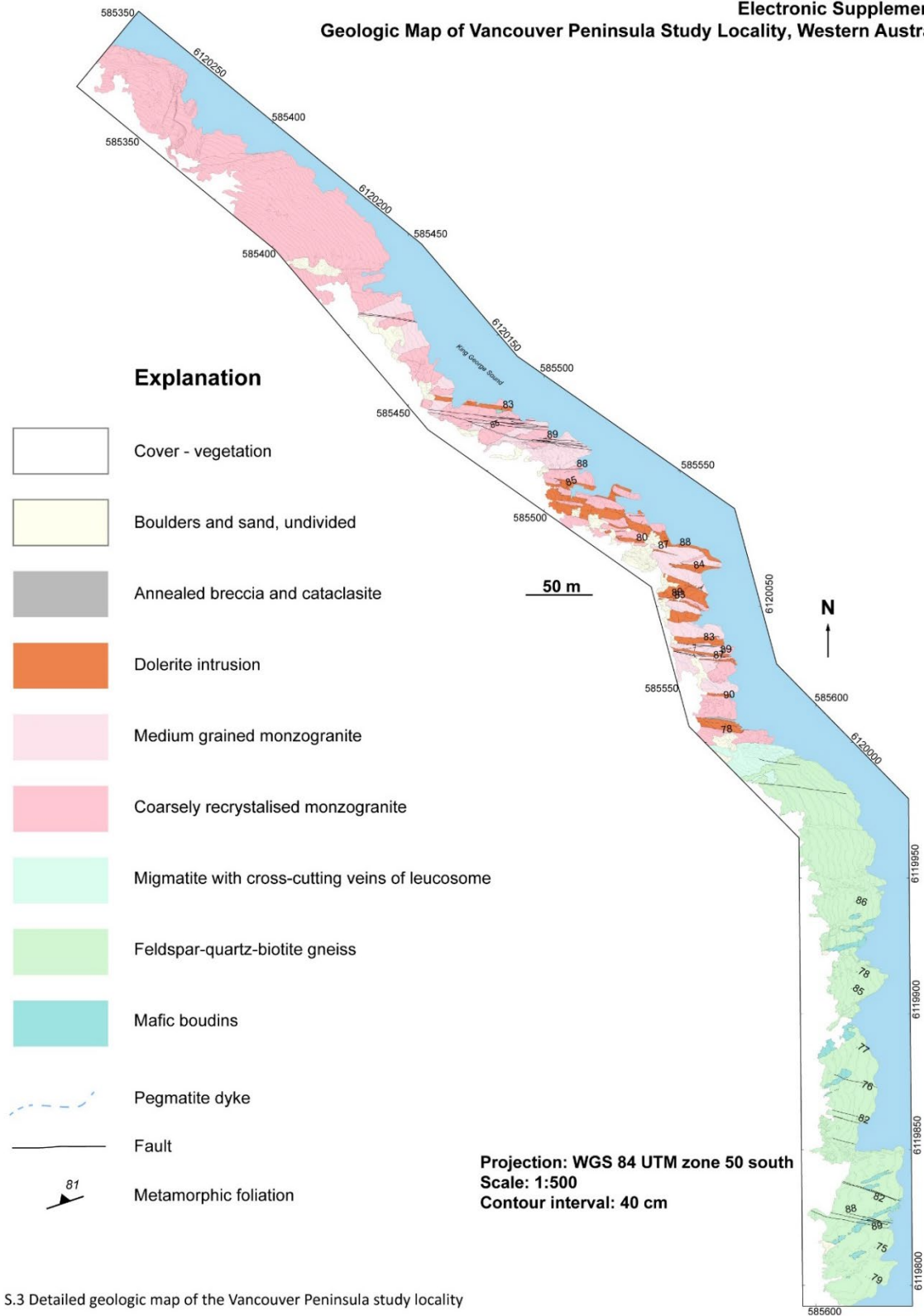


Figure A3 Map of metre-scale scanline site and rose diagrams for all fractures measured at each metre-scale scanline site. Data from sites 1, 2, and 3 are included in Figure 9. Scanlines 1, 2, 3, 4, and 7 are oriented perpendicular to the mean dyke strike direction. The orientation of lines 5, 6, and 8 is parallel to the mean dyke strike.

Appendix 3.3

Electronic Supplement 3 Geologic Map of Vancouver Peninsula Study Locality, Western Australia



S.3 Detailed geologic map of the Vancouver Peninsula study locality

Dyke-induced fracture corridors: evidence for the origin of syn-emplacement seismicity
 Gregory M. Dering, Steven Micklethwaite, Alexander R. Cruden, Stephen J. Barnes, Marco L. Fiorentini

Chapter 4

Dyke propagation and scaling properties revealed from undulating apertures, captured by UAV

Manuscript in the format of Journal of Structural Geology

Gregory M. Dering¹, Steven Micklethwaite², Alexander Cruden², Marco Fiorentini¹

¹ARC Centre of Excellence for Core to Crust Fluid Systems, School of Earth Science, The University of Western Australia, Crawley, Western Australia 6009, Australia

²School of Earth, Atmosphere, and Environment, Monash University, Clayton, 3800, Australia

Corresponding author: Gregory Dering (gregory.dering@research.uwa.edu.au)

Abstract

Using drone-based photogrammetry, >60 outcropping dykes were mapped in 3D at exceptionally high resolution (3-5 mm per pixel) over strike distances up to ~100 m, from the Independence Dyke Swarm, Sierra Nevada, USA. Field observations demonstrate that many of these dykes had multiple pulses of magma input, and that internal crystallisation of the dykes had a significant impact on fracturing and linkage between dyke segments. We develop a digital method for measuring dyke aperture that corrects for outcrop topography. This semi-automated approach was applied to 10 suites of en echelon dykes, to measure aperture at intervals along-strike as narrow as 1 cm, yielding 20,000 aperture measurements from 40 discrete dyke segments. The data reveal that the smaller dykes have tapered length-aperture profiles, but the larger dykes have flat topped length-aperture profiles, with blunt dyke tips and extremely steep aperture gradients. Furthermore, we demonstrate for the first time that dyke apertures have a second order oscillation in amplitude of 10–40 cm along strike. We suggest that solidification and lateral linkage between dyke segments are key processes affecting magma overpressure and thus the growth of dyke networks. We develop a ‘magma breakout’ model that explains the blunt tips between segments and evolution from tapered to flat-topped aperture-length profiles. This model also potentially explains a notable step in the aperture/length scaling properties of dyke populations and the significance of vertical channels of seismicity observed around actively intruding dykes.

4.1 Introduction

Dykes and sills are a key record of magma transport through the crust, supplying melt to volcanic complexes and transferring heat from Earth's interior. Moreover, the transfer of mantle-derived elements into continental crust via mafic and ultramafic dykes contributes to the formation of magmatic sulfide ore deposits. Variation in the aperture and connectivity of dykes is of critical importance for magma through-put and these parameters are thought to be influenced by viscous or elastic host rock deformation, magma pressure variations, stress and magma viscosity (Pollard and Mueller, 1976; Lister and Kerr, 1991). The aperture and hydraulic connectivity of dykes are also influenced by solidification rates and development of load-bearing chilled margins. However, this influence is poorly understood, although the process potentially affects the strength properties of wall rocks and its associated with a hydrodynamic feedback due to the volume change of crystallisation of magma in the dyke (Bruce and Huppert, 1990; Wylie and Lister, 1995; Fialko and Rubin, 1999).

Detailed aperture measurements describing changes within individual dyke segments are rarely reported. Traditional tape-and-compass measurements are affected by the geometry of the outcrop surface intersected by the dyke. As a result, measurement of aperture is time consuming and difficult to do accurately, making detailed systematic data collection prohibitive. However, cases in which they have been examined find significant aperture variations within individual dyke segments (Delaney and Pollard, 1981; Gudmundsson, 1983; Kavanagh and Sparks, 2011; Daniels et al., 2012; Gudmundsson et al., 2012). Gudmundsson et al. (2012) report irregular, second-order aperture variation of 30-50% within the middle portions of basaltic dykes in Iceland. Kavanagh and Sparks (2011) mapped irregular aperture variations along the length of several kimberlite dykes from underground mines, while Pollard and Muller (1976) documented irregular aperture variations of <15% for an 11 km long dyke from Spanish Peaks, Colorado. These results prompt questions as to whether highly irregular aperture results are accurate, or possibly an artefact of thickness measurements derived from variably oriented outcrops. If the observed aperture irregularity is indeed real, is it systematic? If so, what does this information imply for dyke propagation and growth mechanisms?

Until recently, high resolution measurements of dyke aperture variations have not been achievable and so these questions have remained unaddressed. However, in a recent paper Dering et al. (2019a) exploited the data now available from unmanned aerial vehicles (UAVs) and Structure-from-Motion photogrammetry and developed a high-resolution method for aperture measurement. In this study we further develop this method and report aperture measurements for 12 mafic dykes from the Independence Dyke Swarm in eastern California. Our 3D digital reconstructions of outcrops allow dyke margins to be mapped with mm-scale precision at 1-10 cm intervals, across outcrops that expose up to 100 m of strike length. The data reveal that the dyke aperture-length profiles are flat-topped rather than elliptical, display a periodic small-scale amplitude oscillation and exhibit very steep aperture gradients in tip zones (i.e. blunt terminations). Only by obtaining data with such exceptional density and precision has it become feasible to recognise these subtle characteristics. We present a new model for the evolution of the dyke network accounting for both solidification during intrusion and multiple pulses of magma injection.

4.2 Geological setting

The Independence Dyke Swarm is situated in the Mesozoic Cordilleran magmatic arc that formed the Sierra Nevada batholith in southeastern California (Moore and Hopson, 1961). The dyke swarm occupies an elongate corridor extending 600 km NNW from the Mojave Desert in the south to the central Sierra Nevada mountains in the north. The corridor is 40-50 km wide, though a zone of markedly higher dyke density and crustal dilation is restricted to its axial part, spanning 3-4 km (Bartley et al., 2008). The majority of dykes within the swarm were emplaced at 148 ± 1.2 Ma based on K-Ar geochronology (Chen and Moore, 1979; Hopson, 1976) and U-Pb zircon methods (Coleman et al., 1995). The swarm was generated between periods of prolonged and voluminous felsic magmatism that produced granodioritic (123-137 Ma) and granitic plutons (110-135 Ma) in the central Sierra Nevada batholith (Coleman et al., 2005).

The NNW trend of the dyke swarm parallels the Jurassic margin of the Cordilleran subduction zone (Glazner et al., 1999), however individual dykes within the swarm trend 10-20° counterclockwise, striking NW to WNW (Glazner et al., 1999; Martinez-Poza et al., 2014). Furthermore, dykes are

commonly segmented in left-stepping en echelon arrays. These observations led previous workers to suggest that the dykes were emplaced into a zone of incipient shear accommodating regional sinistral transpression. Subsequent regional deformation within the magmatic arc was accommodated within the dyke swarm, with some dykes showing evidence of overprinting solid-state deformation.

The focus of this study is a portion of the dyke swarm in the eastern Sierra Nevada mountains where exposure is exceptionally complete and post-emplacment deformation is minimal (John Bartley, personal communication). The study area lies within the axial part of the dyke swarm where net crustal dilation approaches 20% and the density of dykes across-strike is on the order of 100 per kilometre. The locations of the sites studied in detail using data collected by UAV photogrammetry are provided in Figure 1. Long term erosion, combined with Pleistocene glacial denudation, has revealed mafic dykes emplaced by a combination of elastic and minor ductile-plastic processes, as evidenced by mylonitic fabrics (Carl and Glazner, 2002). The depth of emplacement is estimated to be 8-11 km, based on Al-Hornblende geobarometry from nearby plutonic host rocks (Ague and Brimhall, 1988; Mahan et al., 2003). A consistent isotopic composition of mafic dykes throughout the swarm suggests a shared lithospheric source and previous workers have proposed that magma transport was mainly vertical from a large lithospheric magma reservoir (Glazner et al., 2008).

4.2.1 Study site

The studied dykes lie within the catchment of the South Fork of Big Pine Creek, a glacially denuded series of hanging valleys that drain to the north from a headwall cirque. The dyke swarm is hosted in a hornblende granodiorite of the Jurassic Tinemaha pluton (Fig. 1), which is medium-grained and equigranular with variable concentrations of mafic enclaves and aplite masses up to several hundred meters long. Dykes within the Tinemaha pluton occur in two distinct orientations. The dominant orientation is westerly, with a mean strike of 275° and cross cut an older set of north-striking dykes that comprise <5% of the total swarm. This older population has preferentially accommodated minor dextral shear that post-dates the entire dyke swarm. The data in this study are from the westerly-striking dyke suite that dominate the swarm in this region, which have been subject to only very minor solid-state

deformation relative to the northerly-striking suite. These westerly striking dykes are oriented $\sim 60^\circ$ counterclockwise to the mean trend of the dyke swarm throughout the Sierra Nevada and Inyo Mountains (Bartley et al., 2006). Outside the vicinity of the Tinemaha pluton, dykes dominantly strike northwest, which is only $30\text{--}40^\circ$ from the regional trend of the swarm. There is no evidence for local post-emplacement block rotation (Hopson et al., 2008), so the difference in orientation is interpreted to be a primary feature of the swarm.

Within the Big Pine Creek catchment, westerly-striking dykes are concentrated in two prominent corridors. The axes of the corridors are ~ 2 km apart and data from both corridors are presented in this study (Fig. 1a). The size, orientation, and mineralogy of dykes is similar in both corridors. The mean dyke dip is 85°S , and ranges from 65°S to 85°N . The composition of the swarm throughout the eastern Sierra Nevada is mainly that of calc-alkaline diabase and diorite but also includes sparsely distributed fine-grained felsic dykes (e.g. Coleman et al., 2005).

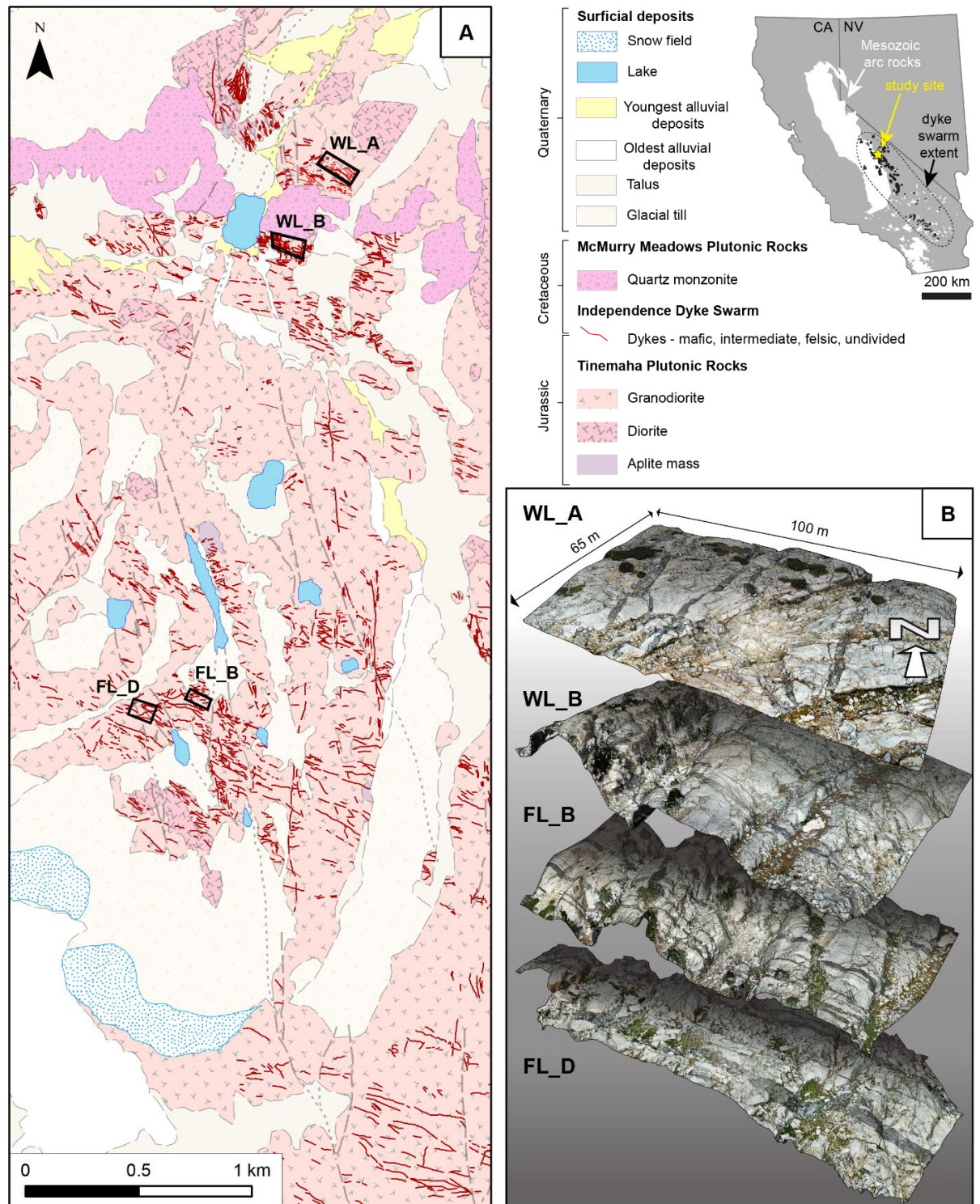


Figure 1. Location and geological setting of the Independence Dyke Swarm in the southern Big Pine Creek catchment. A) Geological map showing two main corridors defined by westerly-striking dykes. Study sites WL_A and WL_B lie within the northern corridor and site FL_B and FL_D lie within the southern corridor. B) 3D digital outcrop reconstructions used in this study derived from UAV photogrammetry. Outcrop morphologies are a product of recent glacial denudation and erosion.

4.3 Methodology

4.3.1 Digital outcrop reconstruction

We combine field observations with digital mapping and structural measurements made from 3D outcrop models (Fig. 1b). The digital outcrop models were produced using photogrammetry techniques which combines computer vision and photogrammetry algorithms to extract 3D geometries from a series of digital 2D images (Bemis et al., 2014). The technique relies on detecting and matching features (arrays of pixels) between overlapping images which capture a static scene from different locations. The ‘structure’ of the scene can then be reconstructed to produce a dense point cloud, which provides a 3D photorealistic representation of the colour, texture, and geometry of the outcrop. For more detailed discussions of SfM and MVS methods in geoscience, see Bemis et al., (2014), Carrivick et al. (Chap. 3, 2016), and Dering et al. (2019a).

The high precision structural data used in this study were extracted from five photogrammetric models (Fig. 1a). Images were collected using a 16 MP camera mounted to a small (< 2 kg) UAV quadcopter. The camera distance to outcrop surface was 9 - 14 m, yielding a ground sampling distance of 2 - 5 mm. Steeply dipping outcrop surfaces that were poorly resolved using the UAV-mounted camera were captured from ground level. Terrestrial and aerial photosets were combined and processed using commercial photogrammetry software Agisoft Photoscan Pro v.1.2. The total area represented by each photogrammetric model was between 6,000 m² to 14,000 m².

Spatial and geometric precision of the models was achieved using an array of ground control points. The ground control points were surveyed using a Trimble RTX GPS with location accuracy of 20 mm and measurement precision of 30 mm. A minimum of 15 survey points was measured at each site. Spatial error for each model was quantified by comparing the location of ground control points in orthorectified imagery against a subset of ground control points withheld from the model building process (following the method described in Dering et al., 2019a).

4.3.2 High resolution aperture measurement

For this study, aperture was measured by comparing the distance of points on opposing dyke walls to a suitably-oriented reference plane. The method is modified from Dering et al. (2019b). Aspects of the methodology that are critical to this study are repeated here.

Aperture data were extracted from dense 3D point clouds using the open source software CloudCompare (<https://www.danielgm.net/cc/>). Dyke wall traces were mapped using the Compass plugin (Thiele et al., 2017) for CloudCompare, based on least-cost edge-matching algorithms. The 3D traces of both dyke margins, for any given dyke, are extracted by sampling a narrow swath of points, referred to here as a *trace cloud*. A reference plane is constructed parallel to the local orientation of the dyke (Dering et al., 2019b, Fig. 8c & d). At a given position along strike, the aperture is calculated by measuring the difference in distance to the reference plane between opposing point pairs in each trace cloud. It is worth noting that dyke dip is well-constrained in areas of high relief and irregular topography and, accurate results can be obtained in digital space where it is difficult to calculate true aperture using conventional tape-and-compass techniques (e.g. Dering et al. 2019b, Fig. 9).

The continuity of dyke traces is commonly broken up due to a combination of segmentation marked by emplacement-related stepovers, as well as post-emplacement faulting or areas of covered outcrop. Our method assumes that the orientations of the two dyke margins involved in each measurement are near-parallel. For most dyke segments, it is enough to assign a single reference plane to the entire segment. In those cases where more geometrically complex dykes are present (i.e. characterised by sharp changes in strike or dip) a single plane is only representative of the dyke orientation over a short distance, thus requiring many more reference planes.

Precision and accuracy were checked by imposing a synthetic dyke of fixed aperture on the dense cloud models. The aperture of the synthetic dyke was measured using the identical method as for the natural dykes. In the study results, aperture data from two synthetic dykes are presented alongside natural dyke measurements to demonstrate the precision of our method relative to the variability observed in the natural datasets. This method both verifies the accuracy of the point cloud and is used to assign a

confidence limit that can be applied to real dykes of similar dimensions and orientation within the models.

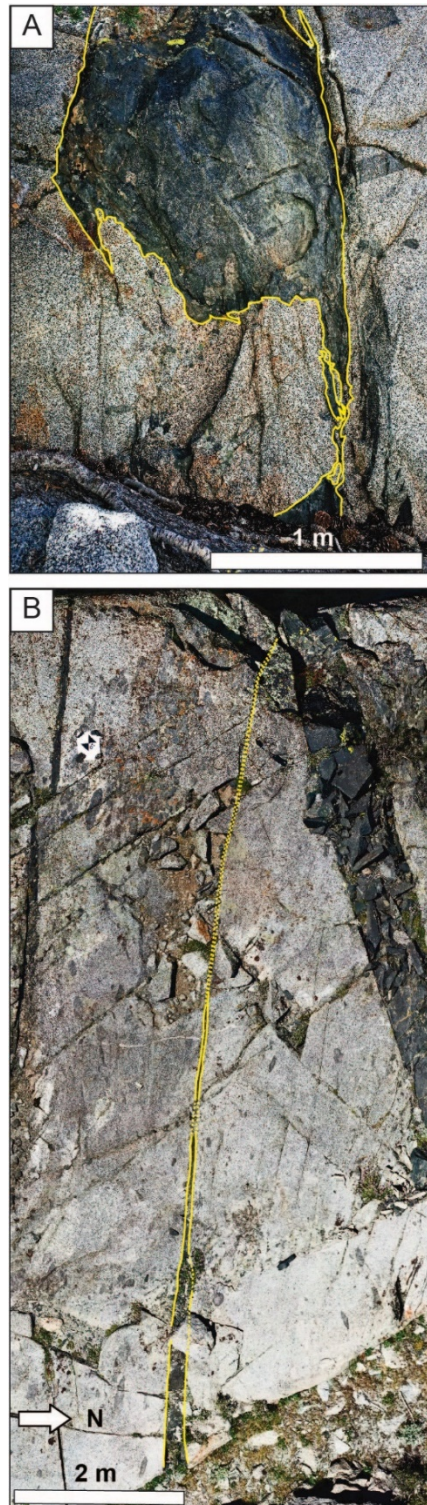


Figure 2 Dyke tips are described as either blunt or bladed-shaped. (a) Blunt-ended dyke exhibiting an extreme change in aperture toward the tip where several cm-scale blade-shaped tips occur. Exposure is a vertical outcrop (looking west). (b) Blade-shaped dyke that tapers gently toward the tip.

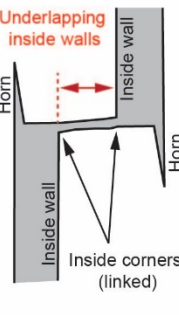
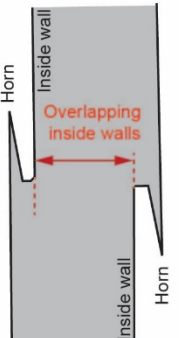
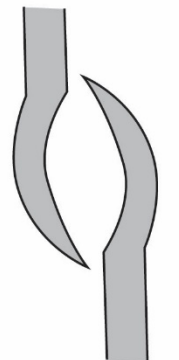
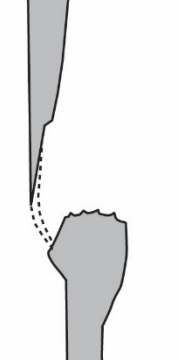
Linkage type	Schematic	Field examples		
A Breakout type 1: Inside walls that <i>underlap</i> across strike				
B Breakout type 2: Inside walls <i>overlap</i> across strike				
C Mutually propagating tips Curved paths result in 'hand-shake' geometries				
D Hybrid/ Asymmetric Tapered and blunt tips interact in a step-over				

Figure 3 Definitions and field examples of the four types of linkage zones that describe the majority of segment terminations. Most common is the rupture of blunt-ended dykes that link via interior corners. Dykes with this type of corner breakout are further subdivided according to (a) Segments that underlap across strike; and (b) Segments that overlap across strike. Dashed yellow lines denote internal zonation of dykes defined by textural contrasts. Less common linkage types are (c) Broken bridges associated with blade-shaped dykes; (d) Asymmetrical tip interaction where opposing tips exhibit a combination of both blunt and bladed-shaped features.

4.4 Tip zones

Dyke linkage between adjacent dyke segments at stepovers is a ubiquitous feature of the swarm. Here we present the most common stepover configurations and field evidence for the role of solidification and multiple magma pulses in dyke linkage.

To a first-order, dyke tips within the study area can be described according to whether the decrease in aperture toward the tip is gradual or abrupt. Gradually tapered terminations approximate blade-shaped profiles, whereas blunt tips are typically more complex and associated with horn structures and stepped margins (Fig. 2a & Fig. 3a & b; cf. Kattenhorn and Whatkeys, 1995). The tip zones documented here belong to segments that are part of larger en echelon dykes. In most cases, dyke tips lie within obvious stepover zones (cf. Nicholson and Pollard, 1985), shared by the tip of the adjacent dyke segment (Fig. 3).

The most common stepover geometry involves blunt-ended segments that terminate in roughly flat ends that are perpendicular to the main strike direction. The dyke tips are commonly straight-sided, resulting in rectangular tip morphologies and exhibit minimal deflection in propagation direction in stepover regions (Fig. 3a & b). Dykes tips with this distinct geometry are present in 55% of the observed stepovers. A defining feature of blunt-tip dyke segments are magma breakouts that consistently breach the tip zone corner that lies closest to the adjacent dyke segment, hereafter referred to as the 'inside' corner. Linkage of breakout features appears to be the most common mechanism by which segments coalesce to form a unified conduit. Slender horns that extend from blunt terminations show evidence of early crystallization (Fig. 3a & d). Another common feature are slender horns parallel to the outer dyke margin that project beyond the breakout zone. Horns vary in length, but rarely exceed the aperture dimension.

Blunt-ended mafic dyke segments with similar flat terminations and lateral breakout features are also found in the Rooi Rand Dyke Swarm, South Africa (Kattenhorn and Whatkeys, 1995). In the Rooi Rand dykes, phenocryst concentrations and host rock deformation led to the interpretation that inflation of the blunt tips preceded magmatic breakout and linkage.

We carefully mapped chilled margins in the dyke swarm where visible (Fig. 4), paying close attention to their geometries at tips and where stepovers have linked together (Figs. 3 & 4). In several cases multiple chill margins were present within a single dyke (see example in Fig. 4f), indicating multiple pulses of magma injection. Though not always the case, the majority of pulses young toward the centre of the dyke, suggesting injection preferentially occurs here rather than along the margins of pre-existing increments. Chilled margins at the tips of dykes or dyke segments are typically rounded relative to the morphology of the dyke (e.g. Fig. 3a). Assuming that the chilled margins developed elastic strength as they formed, then such rounding would have significant impact on the fracture toughness of any dyke segment. Where adjacent dyke segments have linked, chilled margins often thin or disappear (c.f. Fig. 4d–g). This consistent geometry likely arises due to later pulses of magma breaking through the chilled margin during segment linkage. Figure 3 shows that linkage between adjacent dyke segments occurs behind rather than at the segment tips. Many of the segments link at their inner corners, rather than at their tips, even when their tips curve toward one another (Fig. 3d), similar to the models of Nicholson and Pollard (1985).

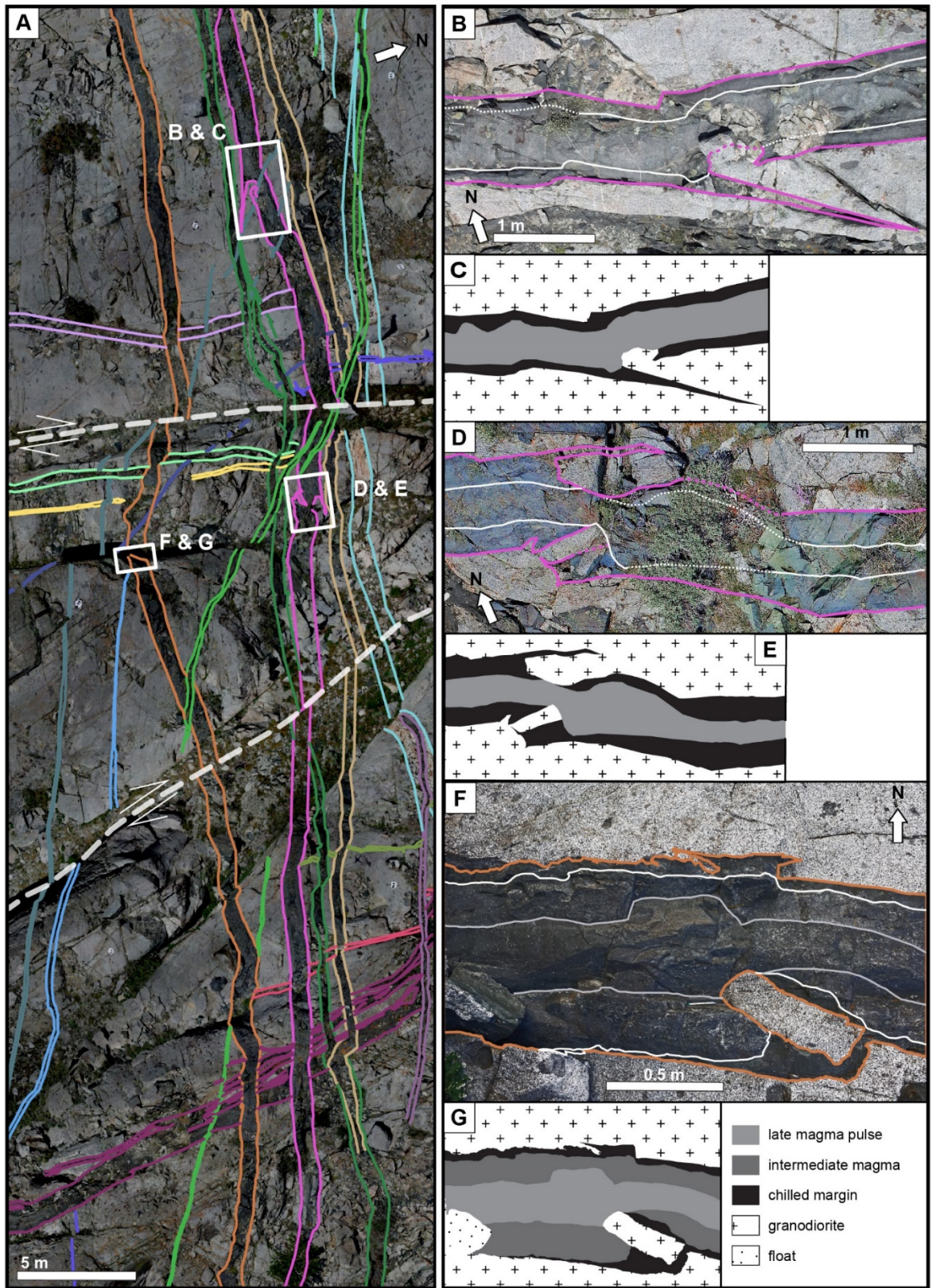
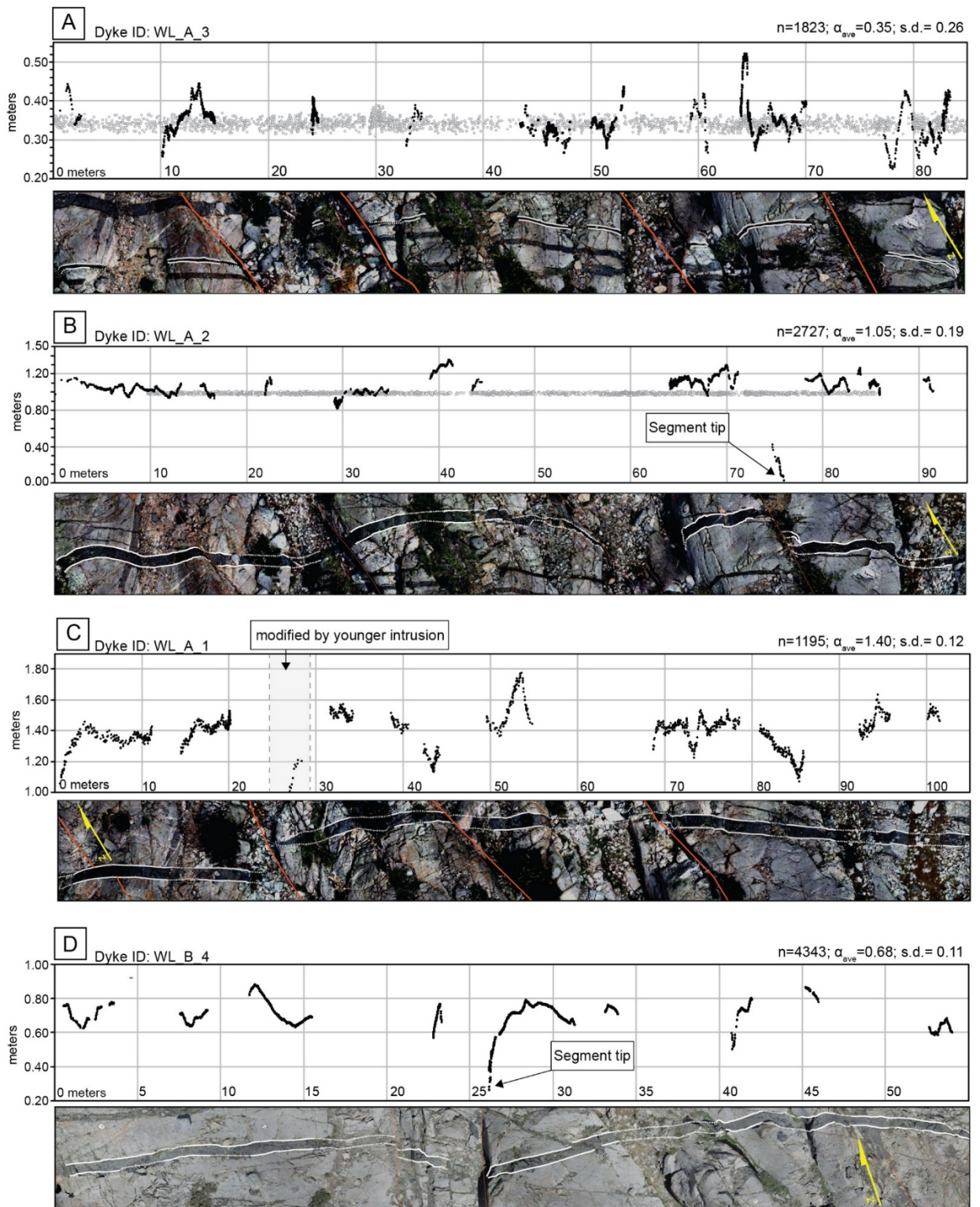


Figure 4 (a) Geologic map from the WL_B survey area with individual dykes distinguished by color of the wall trace. Dashed lines denote small faults. Remnants of breached stepovers that are linked by magmatic breakouts are highlighted and shown in detail at right. Photos of fully linked dyke segments with pronounced textural contrast between fine-grained chilled margins and phenocryst-bearing core zones (b, d, and f). Geologic maps for each photo show that chilled margins in each linkage zone are cross-cut and partially removed by later phases of magma injection. Boundaries between magma pulses denoted by white lines (dashed were concealed). Blade-shaped horns appear to be abandoned following the earliest propagation phase in favor of linkage and magma flux via interior corner breakouts. (c, e, and g).



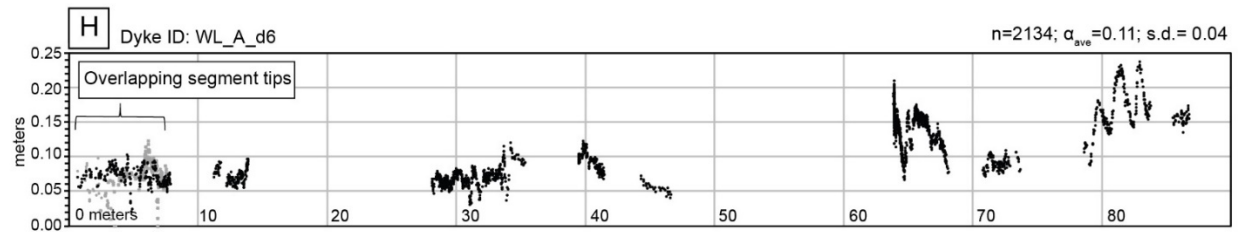
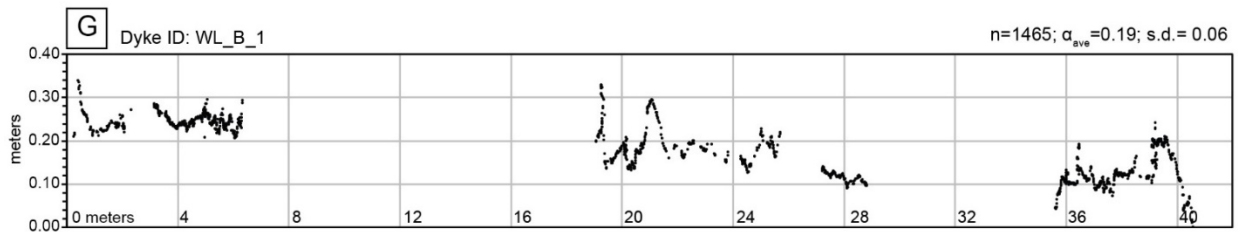
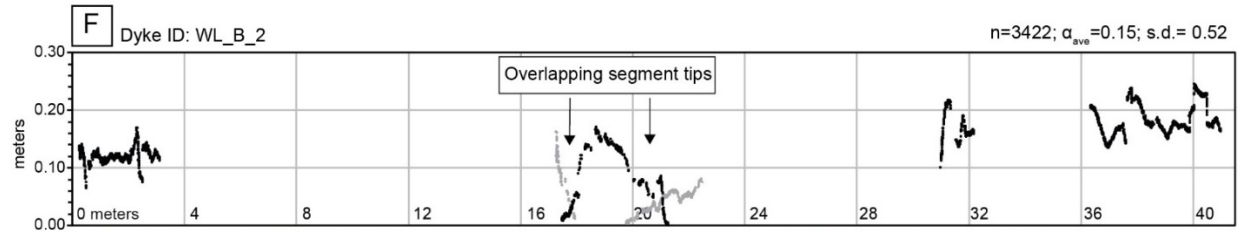
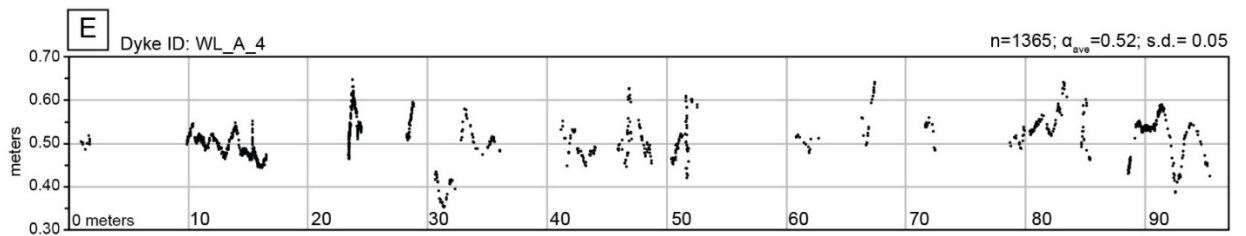


Figure 5 Aperture profile results from 8 dykes with orthoimages for reference. The measured portions of dykes are shown by solid white lines in orthoimages whereas approximate and inferred dyke margins are shown by dashed lines. Red lines denote faults. Alignment of orthoimages and plotted results is variable and approximate due to the transformation of inclined and rotated segments into a normalized reference plane. Gaps in the data are areas where opposing dyke walls could not both be accurately mapped. For each dyke the number of measurements (n), average aperture (α_{ave}), and 1 standard deviation (s.d.) are given. In (a) aperture results for 0.35 m wide synthetic dyke, and in (b) for a 0.9 m wide synthetic dyke, are superimposed (open gray circles) on the outcrop data for comparison purposes. (a) through (e) present results for dykes with flat-topped profiles that exhibit no net change aperture. (f) through (h) are results for multi-segment dykes that show a collective decrease in maximum aperture of consecutive segments. In (f) and (h) the decrease in maximum aperture is from right to left. Data from overlapping segments are distinguished by gray dots. The segments of the dyke in (g) decrease in aperture from left to right.

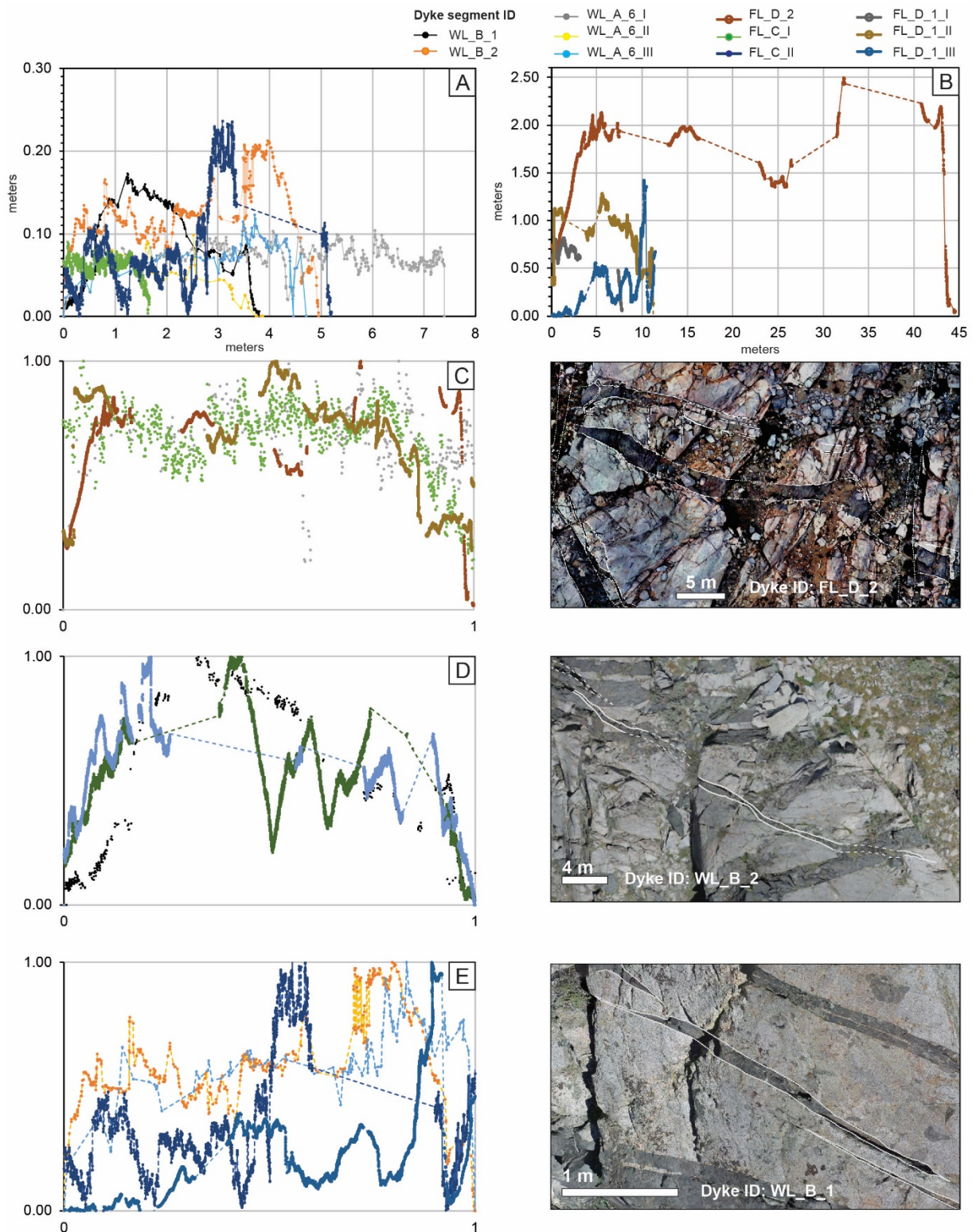


Figure 6 Aperture data from 11 dyke segments exposed from tip to tip. (a) Aperture profiles for segments less than 0.5 m wide. (b) Aperture profiles for segments greater than 0.5 in width. Segment geometries are normalised for comparison purposes and subdivided according to whether they are; (c) flat-topped, (d) symmetrically tapered, and (e) asymmetrically tapered. Plan view images of representative dykes are given at right.

4.5 Aperture results

4.5.1 *Blunt and flat-topped aperture profiles*

Aperture measurements for eight dykes that were traceable for more than 30 m along strike are presented in Figure 5 and data derived from an additional three dykes are in Electronic Supplement 1. Exposed tips and stepover zones reveal that their apertures change abruptly, tapering to a blunt termination over a few metres. This observation leads to the further conclusion that some tips or linkage zones are likely completely obscured across even small covered regions.

Measurement precision was determined by projecting synthetic dykes of similar size and orientation to the real dykes in each digital outcrop model. Aperture results from each of the synthetic dykes yielded standard deviations of 8–9 mm. For comparison purposes, synthetic dyke measurements are superimposed on aperture results from two real dykes (Fig. 5a and b).

Using the first-order aperture profiles, at length scales of 10–100 m, the dykes can be divided according to; (1) flat-topped apertures with very little detectable net change along the strike of the dyke (Fig. 5a–e), and (2) aperture profiles that exhibit some degree of overall taper (Fig. 5f–h). Dykes exhibiting flat-topped profiles have average apertures that range from 35 to 140 cm and broadly similar morphologies. Among dykes of this type, segmentation is sparsely observed, though covered areas may conceal additional tip zones. Where tip zones are measured, the change in aperture is abrupt. For example, dyke WL_A_2 (Fig. 5b) exhibits a linkage zone around 75 m. Mutually propagating tips, resulting in a handshake-type structure is preserved, though only the margins of the left (i.e. west) segment were exposed well enough to measure. The change from average aperture of 105 cm to zero at the tip occurs entirely within the interval from 71 and 75.5 m on the profile. Outside this short interval, the standard deviation in aperture is only 14 cm, with a maximum deviation of 30 cm from the mean. Dyke WL_B_4 (Fig. 5d) exhibits a similarly abrupt segment termination, tapering from 80 to 28 cm between 26 and 28 m on the profile (point cloud density from 25–26 m was too low to measure aperture). Including these zones of precipitous aperture reduction, the subset of dykes in Figure 5a–e do not exhibit elliptical opening profiles predicted by linear elastic fracture mechanics.

Dykes with some degree of quantifiable taper are thinner overall (< 35 cm) and comprised of multiple segments. These dykes show a collective decrease in the maximum aperture of consecutive segments (Fig. 5 f–h). Data from dyke WL_B_2 represent at least three segments and show a net decrease in aperture of approximately 7 cm over 42 m. The observed portion of dyke WL_B_1 comprises at least two segments which show a collective decrease of approximately 13 cm over 41 m. Dyke WL_A_d6 also shows a decrease approximately 13 cm in local aperture maxima, but over a much longer distance of 86 m. The complete overlap of thin segments around 5 m on the profile is not observed elsewhere in the data, but is notable in the context of branching or horsetailing associated with the termination of fracture systems in general. Further segmentation of dyke WL_A_d6 in the interval from 10–86 m is not known due to intervening cover. Averaged of the entire observed interval of each tapered dyke, the rate of aperture change is from $1.5\text{--}3.5\text{ mm}\cdot\text{m}^{-1}$. Changes in aperture over lengths of 2–10 m mainly conform to the tapering direction of the overall array (e.g. Fig 5g, 19–27 m; Fig 5h, 79–84 m). However, exceptions exist (e.g. Fig. 5f, 17–21 m; Fig. 5h. 64–68 m) and gaps in the data make it unclear how aperture trends at this scale relate to the geometry of individual segments within the array.

A remarkable feature of all the dykes is a short period oscillation in aperture that is pervasive along strike (second-order aperture variations). The peak-to-peak amplitude of oscillation ranges from the detection limit (8–9 mm) up to 42 cm. For a given dyke, the size of the aperture oscillation varies along strike and does not correlate with broader scale changes in dyke size. Among dykes with an average aperture < 0.3 m, the oscillatory signal ranges up to 15 cm, and represents a deviation up to 20%, which far exceeds the errors associated with the measurement method (Fig. 5f–h). The largest peak-to-peak amplitudes (42 cm) not associated with tip zones occur along dyke WL_A_1 and represent deviations of 30% from the average aperture of 1.4 m (Fig 5c, at 53.5 m and 85 m). However, large oscillations are also associated with significantly narrower dykes, such as WL_A_3, which exhibits peak-to-peak amplitudes up to 25 cm, a deviation of 71% from the mean aperture of 35 cm (Fig. 5a, from 65–66 m, and 77–83 m). It therefore appears that the amplitude of oscillation is not directly proportional to the size of the dyke. The frequency of oscillation ranges from several cm up to 2 m. Detailed mapping demonstrates the oscillations are related to both finely stepped margins and smoothly tapered changes in

aperture (Electronic Supplement 2). These dykes show very little evidence of post-emplacment deformation, and the oscillations vary in wavelength along each dyke, and from dyke to dyke, which rules out the possibility of post-emplacment boudinage.

4.5.2 Dyke segments

Among the 11 dykes analysed in this study, 8 of them contain discrete segments that could be measured along their entire length. In total, 12 segments were analysed, ranging in length from 1.6 m to 45 m, and in aperture from 6 cm to 2.5 m (Fig. 6a & b). Though these segments represent only fractions of complete dykes, the internal aperture variability is similar to that of the overall dykes.

Figure 6 provides a comparison between individual dyke segment profiles. There are flat-topped profiles (Fig. 6c), symmetrical profiles with a maximum aperture near the dyke midpoint that tapers toward the tips (Fig. 6d), and asymmetric profiles with a maximum aperture closer to one tip than the other (Fig. 6e). Blunt terminations are common (Fig. 6a–c), as are second-order oscillations in aperture that are abrupt and large in relation to the absolute aperture (20–40%).

The dyke segments with flat-topped profiles are among the smallest measured (1.6–7.4 m long). Interestingly, these small segments are associated with dykes that exhibit moderately tapered profiles overall (Fig. 5f, from 17–21 m; Fig. 5g, from 35.5–41 m). The smallest dyke segments share similar aperture values of 5–8 cm even though their length varies between 1.6 m and 7.4 m. The high mapping resolution achieved by UAV photogrammetry means that dyke segments smaller than these would also be within detection limit and gives us confidence that the smallest dyke segments reported here are at or near the lower size limit for the swarm.

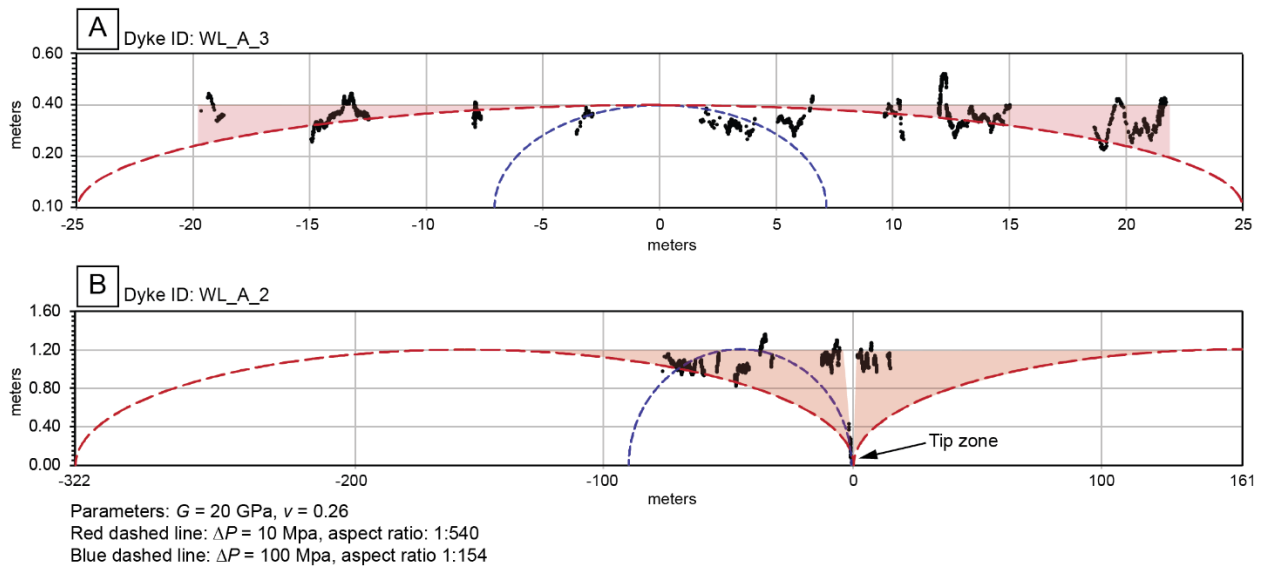


Figure 7 Aperture profiles for several flat-topped dykes illustrate the poor fit of these data to elliptical aperture profiles from LEFM (Pollard and Muller, 1976). Analytical solutions are given for magmatic overpressure of 10 MPa (red dashed line) and 100 MPa (blue dashed line).

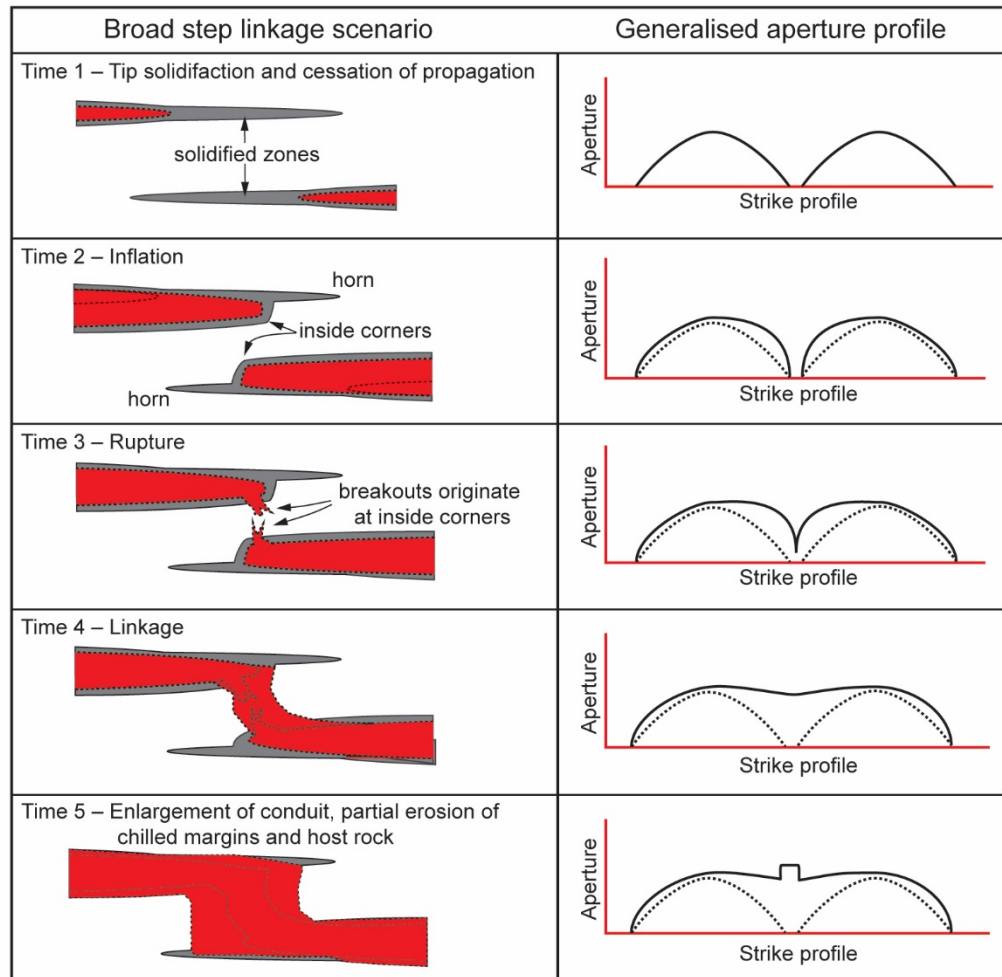


Figure 8 Conceptual model of tip evolution with respect to segment linkage and observed aperture profiles from solidified dykes. In the left-most column, solidified dyke tips pose a mechanical barrier to further propagation. Magma is continuously supplied to the core of the arrested segments, leading to inflation, the formation of blunt tips. The solidified dyke margins eventually fail catastrophically, producing a magmatic breakout and coalescence with the adjacent segment. The geometry of the linkage zone is further modified by thermomechanical erosion, which removes some of the pre-existing solidified margin. An alternative linkage scenario is shown on the right that illustrates incremental dyke growth by repeated cycles of magma injection and solidification into the core of a dyke.

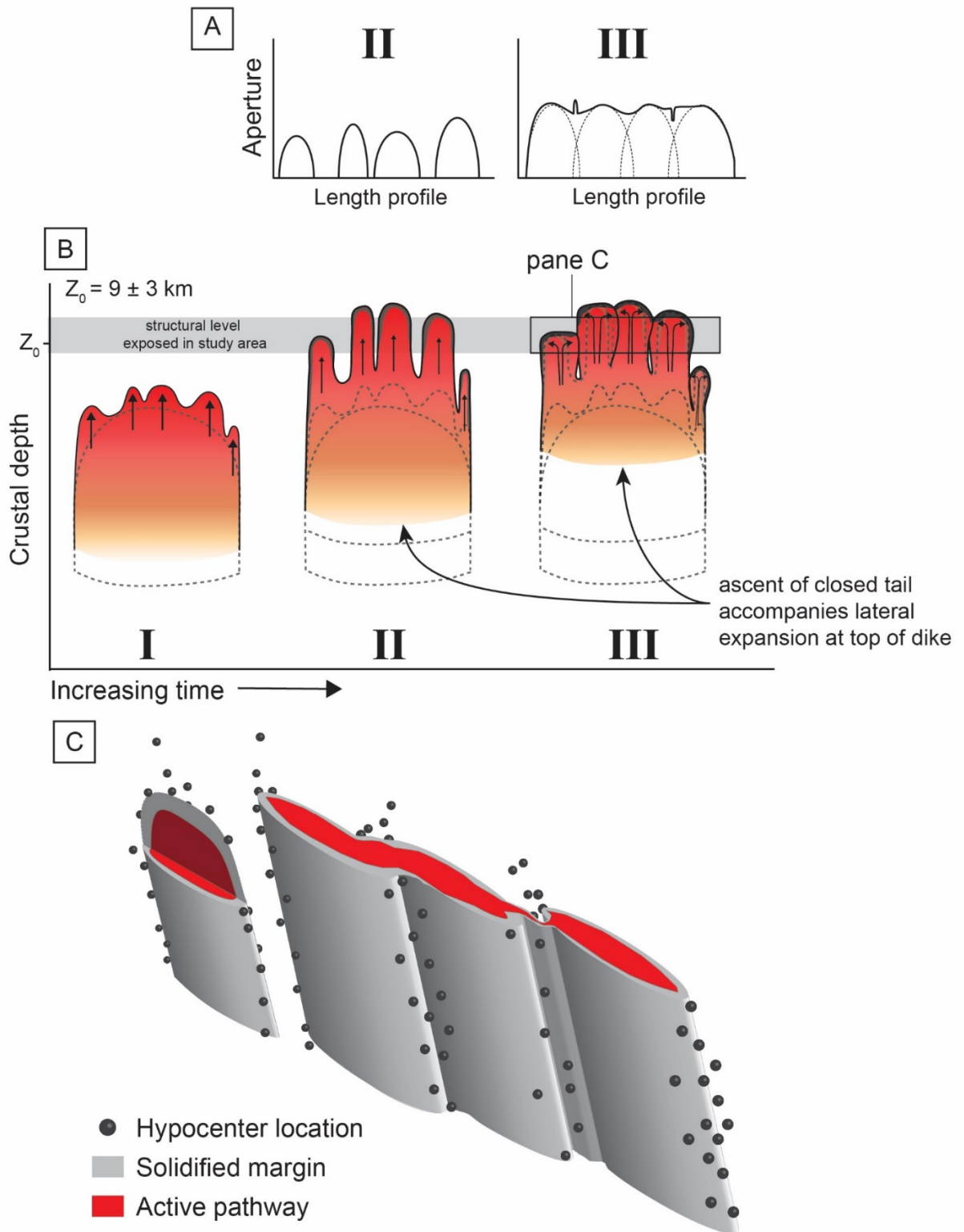


Figure 9 A conceptual model of dyke emplacement that accounts for aperture profiles and patterns of segment linkage documented by this study. (a) The aperture profile of an idealised en echelon dyke showing that the aperture of individual segments approaches the maximum aperture of the complete dyke in the emplacement phase II, prior lateral coalescence of the segments. In phase III, the abrupt peaks and dips in aperture reflect the variable evolution of linkage zones in response to magma through-put. (b) A strike-parallel view of an idealised dyke, that initially ascends vertically (time I), before becoming segmented and beginning to solidify (time II). Lateral propagation and coalescence of segments occurs when buoyant magma continues to ascend through the dyke after the uppermost edge has ceased to propagate vertically and begun to solidify (time III). (c) A 3D cut away view of the partially linked segments near the top of a dyke shows the inferred spatial relationship between vertically distributed hypocentres and magmatic breakout occurring in linkage zones.

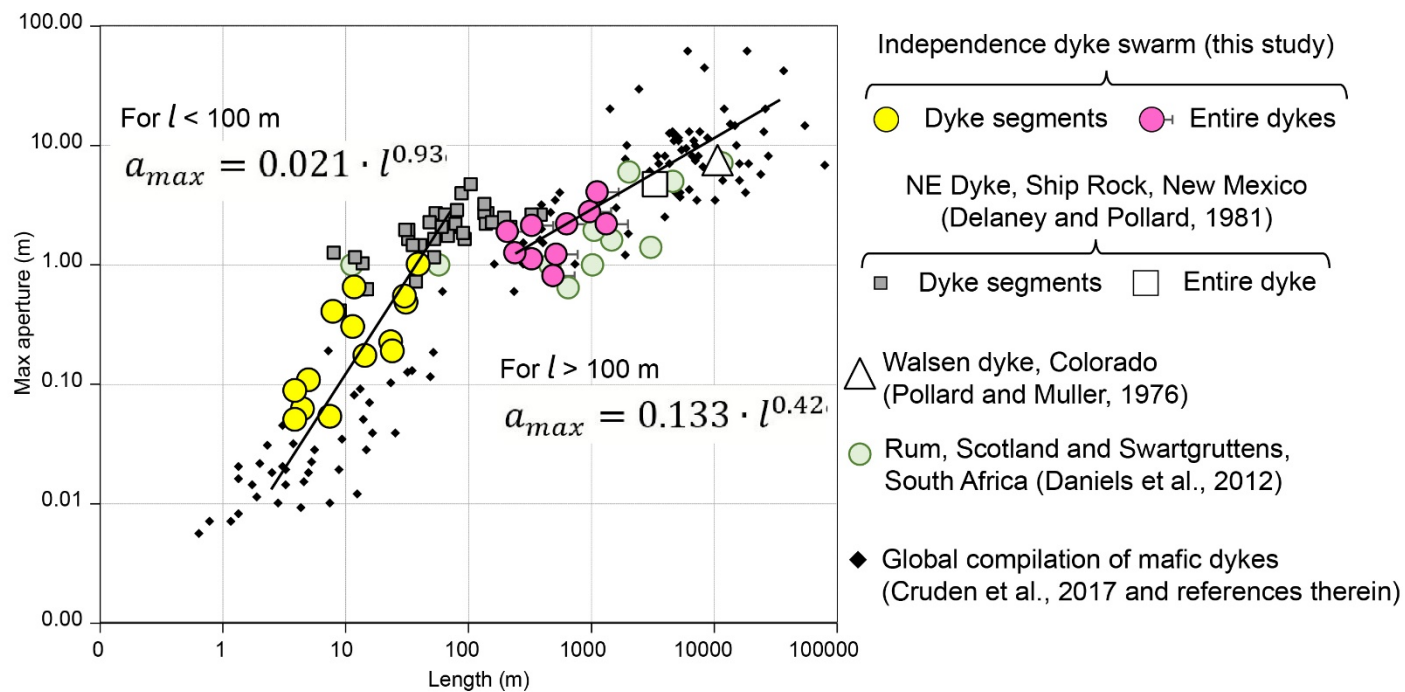


Figure 10 Dyke length (l) versus maximum aperture (a_{max}) for mafic dykes define a semicontinuous trend when plotted at log scale. Data up to ~ 100 m in length define a linear trend with a steeper slope than for lengths greater ~ 100 m. Power law regression fit to the two groups yield power law exponents.

4.6 Discussion

4.6.1 Flat-tops and blunt ends diverge from predicted aperture profiles

We first compare between measured dyke apertures and those based on the LEFM analytical solution for dyke aperture, given by Pollard and Muller (1976):

$$w_y = \frac{l}{2G} [(\Delta P)(1 - \nu)] = A \sin \theta \quad \text{Eq. 1,}$$

where θ is the angular position from the dyke centre, and A is a constant. Equation 1 shows that the ratio of half the aperture w_y to dyke length l is sensitive to the net driving magmatic pressure ΔP and properties of the host rock, which are the shear modulus G and Poisson's ratio ν . Typical elastic properties of the host rock are constrained by both laboratory experiments (Johnson, 1984) and geophysical data from analogous arc settings (e.g. Myers et al., 1998). The driving pressure, ΔP is the combined buoyancy force and magma pressure in excess of the minimum horizontal stress acting on the dyke walls (Shaw, 1980).

The flat-topped aperture profiles identified in this study differ from the idealised elliptical profiles predicted by LEFM by testing for a range of ΔP (10 and 100 MPa). In each case, the net change in aperture along each dyke is much less than predicted and the measured aperture profiles adhere to neither scenario (Fig. 7). The sensitivity of these results were evaluated with respect to values of G and ν and have been to hold across a range of geologically reasonable parameters that are described further in Electronic Supplement 2.

Flat-topped aperture profile midsections can be reproduced by invoking a symmetrical increase in the driving stress from the centre of a dyke toward both dyke tips (Pollard and Muller, 1976; Hoeks, 1995). While not impossible, we are not aware of a viable mechanism to induce the required symmetrical stress gradient with maxima toward the tips. Indeed, the driving stress likely *decreases* toward the dyke tips during the propagation phase due to viscous forces within the dyke (Lister and Kerr, 1991). However, the effects of viscosity on the aperture of mafic dyke segments of the size analysed here are predicted to be very small because viscosity-induced stresses are 2-3 orders less than the magmatic overpressure

(Lister and Kerr, 1991)(Electronic Supplement 2). Either way, it is extremely difficult to reproduce the sharp aperture gradients at dyke tips and the second-order aperture oscillations using such an approach.

4.6.2 *A breakout model for dyke growth*

We argue that the aperture data from the IDS swarm shows that inflation of dyke tips continued after an initial phase of propagation had ceased (dyke arrest). With continued inflation, wall rock failure occurred as a result of magma pressure-driven breakouts across solidified dyke walls (chill margins), leading to segment linkage.

This process accounts for the cross-cutting relations documented in linkage zones (Fig. 4b–f), including the abandonment of horns as propagation paths and abrupt changes in the thickness of fine-grained margins around tip zones (Fig. 4b–f). In terms of elastic deformation, the rapidly solidified dyke tips inhibit further crack propagation as a result of either, 1) increasing the fracture toughness ahead of the remaining pressurised melt, or 2) increasing the minimum principal stress in the vicinity of the dyke tip, effectively increasing the strength of the host rock by reducing the differential stress. According to this qualitative model, the portion of the dyke that becomes inflated, and thus the location of the inside corners, where magmatic breakouts are most commonly observed (Fig. 3a & b), is related to the distance the solidification front advances back into the dyke from the tip prior to breakout.

Segment linkage by magma breakout is capable of producing the observed flat-topped aperture profiles, as summarised in Figure 8 (e.g. high length/aperture ratio). The low length/aperture ratio exhibited by segments prior to rupture is a function of the mechanical barrier posed by the solidified tip zone. Under these conditions, magma overpressure drives further inflation of the dyke segments without further tip propagation to form the observed blunt terminations.

4.6.3 *Aperture as a record of conduit evolution*

The growth of large dykes with flat-topped profiles by the coalescence of tapered, en echelon segments can be understood in terms of a regime in which dominant propagation direction is vertical rather than horizontal. We propose that the two types of aperture profiles represent a continuum of

emplacement processes (Fig. 9a & b). Mafic and intermediate magmas of the IDS were positively buoyant due to the density contrasts with the host rock and are inferred to have ascended kilometers from a source region. However, the lengths of en echelon segments suggest distances of lateral tip propagation were several orders of magnitude less, on the order of meters to tens of meters. A conceptual model for the vertical evolution of a single dyke is presented as a buoyant magma pulse that is disconnected from a parent reservoir and becomes segmented along its ascent path (Fig. 9b). The lateral expansion of en echelon segments is attributed to one or both of the following processes: 1) On-going magma injection, leading to dyke growth in all dimensions; 2) Propagation arrest and solidification at the top of the dyke that forces buoyant magma in the conduit below to spread laterally. Lateral propagation of the dyke leads to linkage between segments, increase in fracture surface area but decrease in magma pressure. Crystallisation leads to development of load-bearing chilled margins, effectively increasing the fracture toughness at the magma front. Because of crystallisation, particularly at dyke tip zones, propagation can be temporarily arrested, until the tip zone inflates, and breakout occurs catastrophically through the chilled margin often forming features such as horns.

4.6.4 Implications for geophysical monitoring of dyke propagation

In our proposed model we argue that dyke segments link by abrupt rupture of arrested, inflating dyke segments. When considered in 3D (Fig. 9c), this model has implications for the interpretation of several aspects of dyke-induced seismicity that are widely documented but remain poorly understood.

During dyke emplacement, seismicity is irregularly distributed along the path of the dyke, well behind the main propagation front (e.g. White et al., 2011; Sigmundsson et al., 2015). In a review of dyke-induced seismicity, Rivalta et al. (2015) contrast the steady advance of hypocentre locations that are correlated with the advancing dyke tip, versus a less organised tail of seismicity that recedes with time. Furthermore, correlations between stalled dyke propagation and earthquake clusters have been identified previously (the Afar Rift, Grandin et al., 2011; Kilauea, Hawaii, Rubin et al., 1998; and Iceland, Woods et al., 2018). Woods et al. (2018) point out that transient dyke arrest alone does not trigger seismicity. Consistent with the model we present in Figure 9, it has been speculated that pressure

changes in the dyke conduit around a step, kink, or similar structural bottleneck are viable mechanisms to excite clusters of seismicity and may explain widely distributed seismicity along dyke paths in the hours prior to solidification (Keir et al., 2009; Belachew, 2011).

Migration of magma at crustal depths greater than ~5 km is commonly associated with seismicity that occurs in vertical, pipe-shaped swarms several km in height, on timescales of hours to days (e.g. Hotovec-Ellis et al., 2018). The spatio-temporal distribution of hypocentre locations from such events commonly lack a unified migration direction and have been correlated with magmatic degassing at the surface (Shelly and Hill, 2011; Lindenfeld et al., 2012). These observations have, understandably, led to an interpretation that the pipe-like swarms are genetically related to volatile release above a region of magmatic unrest. However, the patterns of dyke linkage and magma flux observed from the IDS provide an alternative explanation for the geophysical observations. We suggest that within dyke networks that principally propagate vertically, dyke segments laterally coalesce via magmatic breakouts. For steeply-dipping en echelon dyke segments, this model predicts steeply plunging corridors of tip interaction and seismic energy release associated with breakouts (Fig. 9c). Volatile release may have little to do with the seismicity and may be principally sourced from the dyke segments.

.4.6.5 Implications for scaling relationships

Measurements of maximum aperture and length show that the dimensions of IDS dykes are similar to mafic dykes from other settings across at least 4 orders of magnitude. Complete dykes and individual segments from this study are compared with dimensional data for >300 mafic dykes that have been previously compiled from published and unpublished sources to understand emplacement mechanisms (Cruden et al., 2017) (Fig. 10). Similar to other tabular intrusions, Cruden et al. (2017) show that the growth of mafic dykes follow power-law scaling relationships that can be described in terms of the maximum opening perpendicular to the dyke plane (a_{max}) and horizontal length (l) by the following equation:

$$a_{max} = bl^c \quad \text{Eq. (2)}$$

such that b is a constant and c is the power law exponent. In log-log space, Eq. 2 describes a line with a slope of c . Examined in detail, smaller mafic dykes fit a steeper scaling line ($c \approx 0.9$) than larger dykes ($c \approx 0.4$) which marks a transition from growth that favors aperture growth over horizontal lengthening to a regime dominated by increasing horizontal lengthening. This transition occurs around an aperture of 1 m and length of 100 m. Decreasing slopes of geometric growth curves that also favor lengthening over aperture widening with increasing size have previously been recognized in isolated dyke and vein datasets (Olson, 2003, and references therein). However, the expression of a similar relationship in this global compilation suggests that the balance of conditions governing dyke propagation and growth may be inherently scale-dependent.

The breakout model for dyke growth suggests there is a shift in dyke propagation regimes that is reflected in the scaling relationships. The IDS data from segments and complete dykes comprise a broad and continuous range of aperture values from 5 cm to 5 m. However, a marked break exists in the length data, with no dykes in the 50–220 m length range. The average length/aperture aspect ratio of the segments (150) is about half that of the complete dyke segments (320). Consistent with our model, in the initial phase of vertical propagation the horizontal lengths of individual dyke segments are impeded by mechanical interaction with adjacent segments. Inflation of arrested segments results in a decrease in the length/aperture aspect ratios of individual segments. The second phase of dyke propagation is marked by the linkage of adjacent inflated segments, which leads to flat-topped aperture profiles and an abrupt increase in length/aperture ratio due to the coalescence of multiple segments.

We found a similar, but less distinct contrast between the aspect ratios of segments and a complete dyke within data from the NE dyke at Ship Rock, New Mexico (Delaney and Pollard, 1981) (Fig. 10). The NE dyke is 3200 m long, comprising 35 en echelon segments. In both the IDS and Ship Rock data, dyke segments define a markedly steeper power-law slope in comparison to complete dykes. Despite differences in tectonic setting and emplacement depth, the Ship Rock and IDS segments, along with other small dykes reported by Cruden et al. (2017), exhibit similar relationships between aperture and length growth.

4.7 Conclusion

Using UAV photogrammetry and a newly developed measurement technique, we collected >20,000 aperture measurements from 40 mafic dyke segments, belonging to the Independence Dyke Swarm, California, USA. The key observations arising from this analysis are:

- Dykes >0.5 m wide exhibit flat-topped aperture profiles with blunt terminations.
- Oscillatory aperture variations with wavelengths up to 10s of cm in length are a pervasive, second-order phenomenon in almost all dykes.
- A characteristic feature of blunt dyke terminations are ruptured inner margins, which display the same characteristic geometry in many stepover zones.
- Aperture-length profiles from larger dykes within the swarm reveal flatter midsections and thicker ends than predicted by linear elastic fracture mechanics.
- The apertures of short dyke segments are commonly 1-2 orders of magnitude larger than expected for buoyancy-driven dykes.

A model for dyke growth is introduced that accounts for these observations by the lateral coalescence of overpressured dyke segments. We refer to this as a ‘magma breakout’ model and argue that dyke propagation is arrested in stepover zones even though magma continues to be supplied. Continued inflation of the arrested dyke segments culminates in the catastrophic failure of the dyke wall as a result of accumulated magmatic overpressure. This model explains vertical channels of seismicity observed between segments of active dyke intrusions, as well as a notable step in the length/aperture scaling properties of dykes.

4.8 References

- Ague, J. J., and Brimhall, G. H., 1988, Magmatic Arc Asymmetry and Distribution of Anomalous Plutonic Belts in the Batholiths of California - Effects of Assimilation, Crustal Thickness, and Depth of Crystallization: Geological Society of America Bulletin, v. 100, no. 6, p. 912-927.
- Bartley, J. M., Glazner, A. F., Coleman, D. S., Kylander-Clark, A., Mapes, R., Friedrich, A. M., Till, A., Roeske, S., Sample, S., and Foster, D., 2007, Large Laramide dextral offset across Owens Valley, California, and its possible relation to tectonic unroofing of the southern Sierra Nevada: Geological Society of America Special Paper, v. 434, p. 129.
- Bemis, S. P., Micklethwaite, S., Turner, D., James, M. R., and Thiele, S., 2014, Ground-Based and UAV-based photogrammetry: A Multi-Scale, high-resolution mapping tool for structural geology and paleoseismology, Journal of Structural Geology, v.69, p. 163-178.
- Bruce, P. M., and Huppert, H. E., 1990, Solidification and melting along dykes by the laminar flow of basaltic magma, *in* Ryan, M. P., ed., Magma Transport and Storage, Wiley, p. 420.
- Carl, B. S., and Glazner, A. F., 2002, Extent and significance of the Independence dike swarm, eastern California: Geologic Evolution of the Mojave Desert and Southwestern Basin and Range: Geological Society of America Memoir, v. 195, p. 117-130.
- Carrivick, J. L., Smith, M. W., and Quick, J. E., 2016, Structure from Motion in the Geosciences, Oxford, Wiley-Blackwell, Analytical Methods in Earth and Environmental Science, 208 p..
- Chen, J. H., and Moore, J. G., 1979, Late Jurassic Independence dike swarm in eastern California: Geology, v. 7, no. 3, p. 129-133.
- Coleman, D. S., Glazner, A., Miller, J., Bradford, K., Frost, T., Joye, J., and Bachl, C., 1995, Exposure of a late Cretaceous layered mafic-felsic magma system in the central Sierra Nevada Batholith, California: Contributions to Mineralogy and Petrology, v. 120, no. 2, p. 129-136.
- Coleman, D. S., Bartley, J. M., Glazner, A. F., and Law, R. D., 2005, Incremental assembly and emplacement of Mesozoic plutons in the Sierra Nevada and White and Inyo Ranges, California: Geological Society of America Field Forum, 95 p.
- Cruden A. R., McCaffrey K.J.W., Bunker A. P., 2017, Geometric Scaling of Tabular Igneous Intrusions: Implications for Emplacement and Growth, *in* Breikreuz C., Rocchi S., eds,

- Physical Geology of Shallow Magmatic Systems. *Advances in Volcanology*. Springer, 409 p.
- Daniels, K. A., Kavanagh, J. L., Menand, T., and Sparks, R. S. J., 2012, The shapes of dikes: Evidence for the influence of cooling and inelastic deformation, *Geological Society of America Bulletin*, v. 124, no. 7/8, p. 10-18.
- Delaney, P.T. and Pollard, D.D., 1981, Deformation of host rocks and flow of magma during growth of minette dikes and breccia-bearing intrusions near Ship Rock, New Mexico, U.S. Geological Survey Prof. Paper 1202, 69 p.
- Dering, G.M., Micklethwaite, S., Cruden, A.R., Barnes, S.J. and Fiorentini, M.L., 2019a, Evidence for dyke-parallel shear during syn-intrusion fracturing: *Earth and Planetary Science Letters*, 507, pp.119-130, doi.org/10.1016/j.epsl.2018.10.024.
- Dering, G.M., Micklethwaite, S., Thiele, S.T., Vollgger, S.A. and Cruden, A.R., 2019b, Review of drones, photogrammetry and emerging sensor technology for the study of dykes: Best practises and future potential: *Journal of Volcanology and Geothermal Research*, v. 363, p. 148-166, doi.org/10.1016/j.jvolgeores.2019.01.018.
- Fialko, Y. A., and Rubin, A. M., 1999, Thermal and mechanical aspects of magma emplacement in giant dike swarms: *Journal of Geophysical Research-Solid Earth*, v. 104, no. B10, p. 23033-23049.
- Glazner, A. F., Bartley, J. M., and Carl, B. S., 1999, Oblique opening and noncoaxial emplacement of the Jurassic Independence dike swarm, California: *Journal of Structural Geology*, v. 21, no. 10, p. 1275-1283.
- Glazner, A. F., Carl, B. S., Coleman, D. S., Miller, J. S., and Bartley, J. M., 2008, Chemical variability and the composite nature of dikes from the Jurassic Independence dike swarm, eastern California: *Geological Society of America Special Papers*, v. 438, p. 455-480.
- Grandin, R., Jacques, E., Nercessian, A., Ayele, A., Doubre, C., Socquet, A., Keir, D., Kassim, M., Lemarchand, A., and King, G. C. P., 2011, Seismicity during lateral dike propagation: Insights from new data in the recent Manda Hararo-Dabbahu rifting episode (Afar, Ethiopia): *Geochemistry Geophysics Geosystems*, v. 12, no. 4, Q0AB08.
- Gudmundsson, A., 1983, Form and dimensions of dykes in eastern Iceland: *Tectonophysics*, v. 95, no.

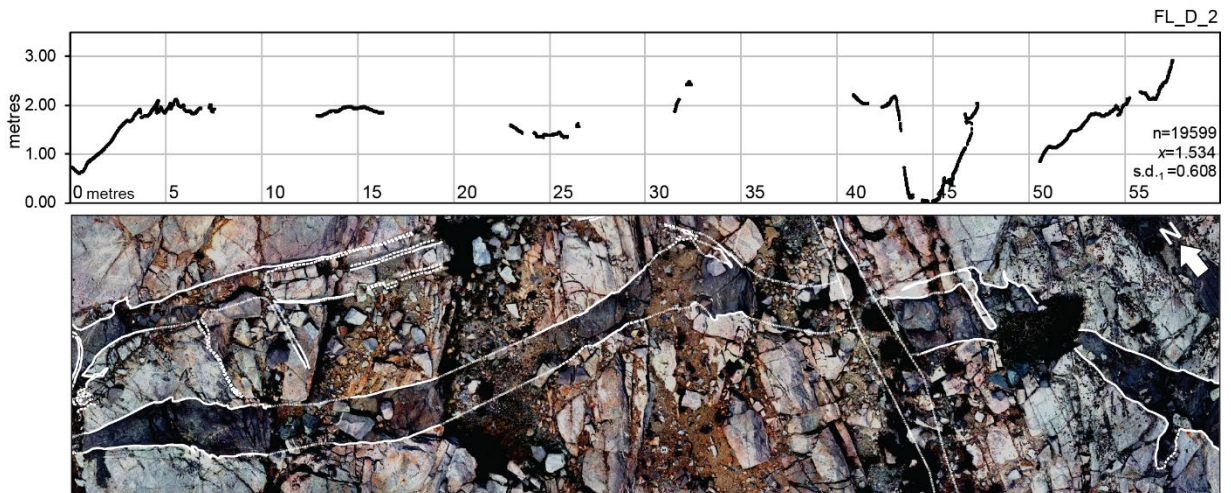
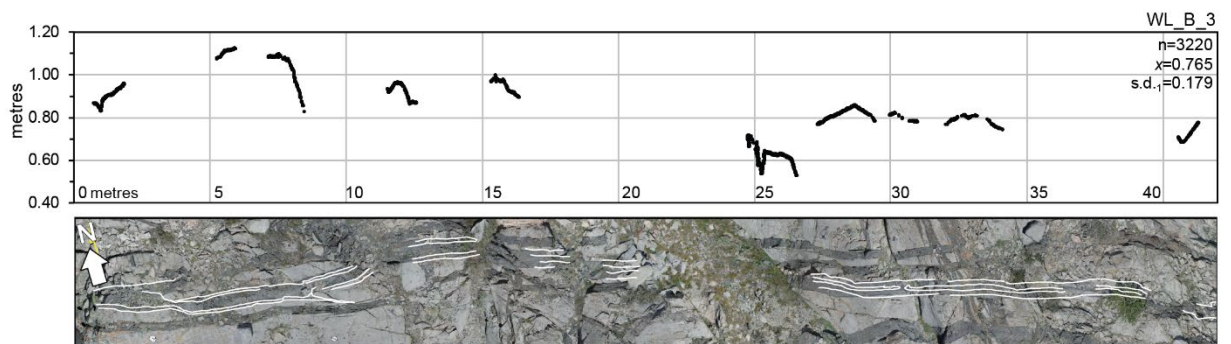
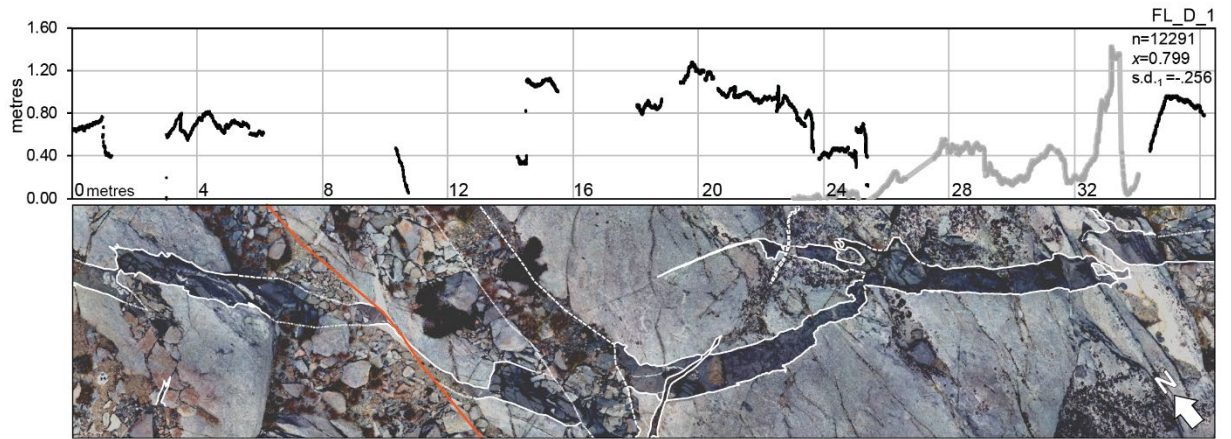
3-4, p. 295-307.

- Gudmundsson, A., Kusumoto, S., Simmenes, T. H., Philipp, S. L., Larsen, B., and Lotveit, I. F., 2012, Effects of overpressure variations on fracture apertures and fluid transport: *Tectonophysics*, v. 581, no. Supplement C, p. 220-230.
- Hoek, J. D., 1995, Dyke propagation and arrest in proterozoic tholeiitic dyke swarms, Vestfold Hills, East Antarctica: *Physics and Chemistry of Dykes*, p. 79-93.
- Hopson, R. F., Hillhouse, J. W., and Howard, K. A., 2008, Dike orientations in the Late Jurassic Independence dike swarm and implications for vertical-axis tectonic rotations in eastern California: *Ophiolites, Arcs, and Batholiths: A Tribute to Cliff Hopson*, v. 438, p. 481-498.
- Hotovec-Ellis, A. J., Shelly, D. R., Hill, D. P., Pitt, A. M., Dawson, P. B., and Chouet, B. A., 2018, Deep fluid pathways beneath Mammoth Mountain, California, illuminated by migrating earthquake swarms: *Science Advances*, v. 4, no. 8.
- Johnson, T. L., 1984, Measurement of Elastic Properties and Static Strength: US Department of Defense, Report 4770, 24 p.
- Kattenhorn, S., and Watkeys, M., 1995, Blunt-ended dyke segments: *Journal of Structural Geology*, v. 17, no. 11, p. 1535-1542.
- Kavanagh, J. L., and Sparks, R. S. J., 2011, Insights of dyke emplacement mechanics from detailed 3D dyke thickness datasets: *Journal of the Geological Society, London*, v. 168, p. 13.
- Keir, D., Bastow, I. D., Whaler, K. A., Daly, E., Cornwell, D. G., and Hautot, S., 2009, Lower crustal earthquakes near the Ethiopian Rift induced by magmatic processes.
- Kusumoto, S., Geshi, N., and Gudmundsson, A., 2013, Aspect ratios and magma overpressures of non-feeder dikes observed in the Miyakejima Volcano (Japan), and fracture toughness of its upper part: *Geophysical Research Letters*, v. 40, no. 6, p. 1065-1068.
- Lindenfeld, M., Rumpker, G., Link, K., Koehn, D., and Batte, A., 2012, Fluid-triggered earthquake swarms in the Rwenzori region, East African Rift: Evidence for rift initiation: *Tectonophysics*, v. 566, p. 95-104.
- Lister, J. R., and Kerr, R. C., 1991, Fluid-mechanical models of crack propagation and their application to magma transport in dykes: *Journal of Geophysical Research*, v. 96, no. B6, p. 28.

- Mahan, K. H., Bartley, J. M., Coleman, D. S., Glazner, A. F., and Carl, B. S., 2003, Sheeted intrusion of the synkinematic McDoyle pluton, Sierra Nevada, California: *Geological Society of America Bulletin*, v. 115, no. 12, p. 1570-1582.
- Martinez-Poza, A. I., Glazner, A. F., and Bartley, J. M., 2013, 3D Analysis of a multiple dike intrusion and later deformation, Independence Dike Swarm, California, GSA Annual Meeting: Denver, Colorado.
- Moore, J. G., and Hopson, C. A., 1961, The Independence dike swarm in eastern California: *American Journal of Science*, v. 259, no. 4, p. 241-259.
- Murase, T., and McBirney, A. R., 1973, Properties of some common igneous rocks and their melts at high temperatures: *Geological Society of America Bulletin*, v. 84, no. 11, p. 3563-3592.
- Myers, S. C., Beck, S., Zandt, G., and Wallace, T., 1998, Lithospheric-scale structure across the Bolivian Andes from tomographic images of velocity and attenuation for P and S waves: *Journal of Geophysical Research: Solid Earth*, v. 103, no. B9, p. 21233-21252.
- Nicholson, R., and Pollard, D., 1985, Dilation and linkage of echelon cracks: *Journal of Structural Geology*, v. 7, no. 5, p. 583-590.
- Olson, J.E., 2003, Sublinear scaling of fracture aperture versus length: An exception or the rule?: *Journal of Geophysical Research*, v. 108, no. B9, doi:10.1029/2001JB000419.
- Pollard, D. D., and Muller, O. H., 1976, The effect of gradients in regional stress and magma pressure on the form of sheet intrusions in cross section: *Journal of Geophysical Research*, v. 81, no. 5, p. 975-984.
- Pollard, D. D., and P. Segall, Theoretical displacements and stresses near fractures in rock: With applications to faults, joints, veins, dikes and solution surfaces, 1987, *in Fracture Mechanics of Rock*, ed. B. K. Atkinson, Academic, San Diego, Calif. pp. 277-350.
- Rivalta, E., Taisne, B., Bungler, A. P., and Katz, R. F., 2015, A review of mechanical models of dike propagation: Schools of thought, results and future directions: *Tectonophysics*, v. 638, p. 1-42.
- Rubin, A. M., Gillard, D., and Got, J. L., 1998, A reinterpretation of seismicity associated with the January 1983 dike intrusion at Kilauea Volcano, Hawaii: *Journal of Geophysical Research: Solid Earth*, v. 103, no. B5, p. 10003-10015.

- Shaw, H. R., 1980, The fracture mechanisms of magma transport from the mantle to the surface: *Physics of magmatic processes*, v. 64, p. 201-264.
- Shelly, D. R., and Hill, D. P., 2011, Migrating swarms of brittle-failure earthquakes in the lower crust beneath Mammoth Mountain, California: *Geophysical Research Letters*, v. 38, no. 20.
- Sigmundsson, F., Hooper, A., Hreinsdottir, S., Vogfjord, K. S., Ofeigsson, B. G., Heimisson, E. R., Dumont, S., Parks, M., Spaans, K., Gudmundsson, G. B., Drouin, V., Arnadottir, T., Jonsdottir, K., Gudmundsson, M. T., Hognadottir, T., Fridriksdottir, H. M., Hensch, M., Einarsson, P., Magnusson, E., Samsonov, S., Brandsdottir, B., White, R. S., Agustsdottir, T., Greenfield, T., Green, R. G., Hjartardottir, A. R., Pedersen, R., Bennett, R. A., Geirsson, H., La Femina, P. C., Bjornsson, H., Palsson, F., Sturkell, E., Bean, C. J., Mollhoff, M., Braiden, A. K., and Eibl, E. P. S., 2015, Segmented lateral dyke growth in a rifting event at Bardarbunga volcanic system, Iceland: *Nature*, v. 517, no. 7533, p. 191-U158.
- Thiele, S. T., Grose, L., Samsu, A., Micklethwaite, S., Vollgger, S. A., and Cruden, A. R., 2017, Rapid, semi-automatic fracture and contact mapping for point clouds, images and geophysical data: *Solid Earth*, v. 8, no. 6, p. 1241.
- White, R. S., Drew, J., Martens, H. R., Key, J., Soosalu, H., and Jakobsdottir, S. S., 2011, Dynamics of dyke intrusion in the mid-crust of Iceland: *Earth and Planetary Science Letters*, v. 304, no. 3-4, p. 300-312.
- Woods, J., Donaldson, C., White, R. S., Caudron, C., Brandsdóttir, B., Hudson, T. S., and Ágústsdóttir, T., 2018, Long-period seismicity reveals magma pathways above a laterally propagating dyke during the 2014–15 Bárðarbunga rifting event, Iceland: *Earth and Planetary Science Letters*, v. 490, p. 216-229.
- Wylie, J. J., and Lister, J. R., 1995, The effects of temperature-dependent viscosity on flow in a cooled channel with application to basaltic fissure eruptions: *Journal of Fluid Mechanics*, v. 305, p. 239-261.

Appendix 4.1



Appendix 4.2

Parameter	Symbol	Units	Value used	Estimated range	Source
Properties of emplacement environment					
Depth	z	m	9,000	8,000-11,000	Ague and Brimhall, 1988
Geothermal gradient	ΔT	°C/km	30	22-39	Turcotte and Schubert, 2002
Lithostatic pressure	σ	MPa	240	200-310	Pollard and Fletcher, 2001
Average density of crust	ρ	kg/m ³	2700	2500-2800	Turcotte and Schubert, 2002
gravitational acceleration	g	m/s ²	8.91		
Properties of Tinemaha granodiorite host rock					
Density of granodiorite at 270 °C	ρ_r	kg/m ³	2780	2650-2900	Gudmundsson, 2001
Shear modulus	G	GPa	20	18-30	Johnson, 1984
Poisson's ratio	ν	--	0.26	0.20-0.28	Johnson, 1984
Friction coefficient	u_s	--	0.43		
Properties of IDS magma					
Density	ρ_m	kg/m ³	2650	2600-2800	Murase and McBirney, 1973
Magma pressure	P_m	MPa	*--	10 ⁰ - 10 ⁵	Turcotte and Schubert, 2002
Vertical height of magma column	H_m	m	*--	100 - 10000	
Temperature	T_m	°C	1150	950-1200	Murase and McBirney, 1973

*-- To be estimated

Notation	Symbol	Units
dyke length	l	m
aperture	a	m
maximum aperture	a_{max}	m
half aperture	w_y	m
angular position along slit	θ	degrees
regional horiz. stress normal to crack ($S_y = S_h$)	S_y	MPa
regional horiz. stress parallel to crack ($S_x = S_H$)	S_x	MPa
constant	A	--
constant	B	--
driving pressure ($S_y - P_m$)	ΔP	MPa
magmatic pressure gradient	∇P	MPa · m ⁻¹
gradient in confining stress normal to dyke	∇S	MPa · m ⁻¹

Tectonic stress state	Symbol	Units	Weak transtension	Weak transpression	Extension
stress ratio	R	--	0.55	0.45	0.5
Maximum horizontal stress	S_H	MPa	166		
Minimum horizontal stress	S_h	MPa	76		
Maximum vertical stress	S_v	MPa	240	240	240

$$R = \frac{S_H - S_h}{S_v - S_h}$$

Horizontal magmatic pressure gradient

$$w_y = \frac{l^2 \sin 2\theta}{16G} [(\nabla P - \nabla S)(1 - \nu)] = B \sin \theta$$

Buoyancy force calculation

Buoyancy force	ΔP_b	$\frac{\text{Mpa} \cdot \text{m}^{-1}}$	0.1274
----------------	--------------	---	--------

$$\Delta P_b = g \times (\rho_r - \rho_m) \times H_m$$

Chapter 5: Conclusions

Insights into dyke emplacement mechanisms using new high-resolution 3D digital outcrop methods

5.1. Key research outcomes

This study develops new digital workflows tailored to the analysis of dykes in outcrop using UAV photogrammetry. In Chapter 2 recently developed tools for the analysis of geologic features from 3D point clouds, structural aspects of mafic dyke swarms were resolved at mm resolution over areas of tens of thousands of square meters. This approach enabled measurement of dyke-related structures with a precision that could be quantified and at a data density not previously feasible. In Chapter 3 these new methods were used measure deformation intensity across a well-exposed dyke swarm on the south coast of Western Australia. In Chapter 4 high resolution dyke aperture data from the Sierra Nevada, USA, were compared dyke profile geometries predicted from fracture mechanics. The main outcomes of from the projects are summarised below.

5.1.1. Digital outcrop methods

Digital outcrop models can be used as research tools that go beyond qualitative visualization. UAV-photogrammetry enables precise measurement of bedrock structures over length-scales and at resolutions not previously achievable. As a result UAV-based techniques are set to provide a step-change in field observations and enable us to address many outstanding questions about dyke emplacement.

5.1.2 Dyke-induced fracture corridors

The high resolution structural transect provides spatial constraints on macrofracture development around the Albany dyke swarm and demonstrates that shear failure occurs in the host rocks around the dyke swarm, rather than by rupture of solidified plugs within dykes. Fracturing and faulting associated with intrusions differs from the development of damage around amagmatic faults, which normally involves an increase in fracture intensity toward a fault core. Fracturing precedes and accompanies dyke swarm formation, both as opening mode tensile failure and shear failure on planes that are parallel to the orientation of the dykes, within the host rocks around the dykes. We suggest that tensile failure occurred ahead of propagating dykes, as joints, which are then reactivated under shear as the dykes continue to propagate due to changing host rock elastic properties and local stress reorientation. Our outcrop observations and this model of dyke parallel faulting contrast with conventional understanding of dyke-fault interactions, which normally invokes a fault angle of $\sim 30^\circ$ to the dyke plane. Our finding that rupture occurs on faults parallel to the dykes and that host rock damage preceded magma

intrusion is consistent with seismological and geodetic observations from dyke emplacement events in Iceland in 2006 and 2007 (White et al., 2011).

5.1.3 Aperture variation

Within the Independence Dyke Swarm, internal crystallisation of the dykes has a significant impact on fracturing and linkage between dyke segments. Furthermore, we demonstrate for the first time that dyke apertures have a second order oscillation in amplitude of 20–40 cm along strike. We suggest crystallisation and lateral linkage between dyke segments are key processes affecting magma overpressure and thus the growth of dyke networks. A model for dyke growth that explains the blunt tips between segments, second-order dyke aperture variations and evolution from tapered to flat topped aperture-length profiles. Our model also potentially explains a notable step in the aperture/length scaling properties of dyke populations and the significance of vertical channels of seismicity observed around actively intruding dykes. The data presented here are derived from dykes emplaced at mid-crustal depths, characterised by high lithostatic pressures and thermal gradients more subdued than typical upper crustal settings. It remains unclear whether second order aperture oscillation is a feature of dykes in other settings because it has not previously been feasible to collect data of similar density and precision. Above the brittle-ductile transition, the mechanical aspects of dyke propagation and inflation are predicted to vary linearly with depth.

5.2 Future research

This study employed a combination of new high-precision methods, alongside traditional field work to define dyke geometries and fracture networks. The results have been compared with analytical solutions derived from linear elastic fracture mechanics. This approach produced an array of surprising results that merit further investigation, as detailed below.

At Albany, the dyke swarm occupies a deformation corridor defined by fractures visible to the unaided eye (i.e. apertures ≥ 0.5 mm). Studies of fault-related damage zones demonstrate an empirical relationship between the intensity of micro-fractures in quartz and macro-fractures that scales with distance from the fault core (Mitchell and Faulkner, 2009). A systematic investigation of microstructural deformation spanning the presently defined dyke corridor could be used to further compare dyke-induced deformation (which act as mode I cracks occupied by overpressured fluids) from the distributed damage documented around fault cores.

In Chapter 3 (Section 3.6.2), a model is presented which predicts changes in the bulk elastic properties of the host rock around the Albany dyke swarm sufficient to alter the trajectories of regional

stresses. This concept should be evaluated quantitatively with laboratory rock mechanics experiments, following the general approach of Faulkner et al. (2006).

Chapter 4 presents dyke aperture and segmentation data measured parallel to strike. These structural relationships are preserved in glacially polished outcrop surfaces that broadly expose a subhorizontal plane through a dyke swarm. However, subvertical exposures of the dyke swarm are also available for study, representing a cross-sectional view through the swarm. UAV-photogrammetry methods are well-suited to surveys of such outcrops. The geometry of dykes measured in the sub-vertical (i.e. dip-parallel) dimension would be expected to reflect gradients in lithostatic stress and driving magmatic pressure not apparent in horizontal sections. To our knowledge, vertical aperture profiles of natural dykes have never been produced.

Intrusion-hosted magmatic sulfide ore deposits are associated with dykes and other magmatic conduits that host prolonged magma flux (e.g. Barnes and Mungall, 2018; Barnes et al., 2016). We speculate that such conditions are more likely to be met within intrusions that maintain hydraulic connection to a remote, pressurised source region, rather than isolated intrusions with closed tails (cf. Dahm, 2000). However, little attention has been given to geometrical differences that may distinguish these two types of intrusions. In terms of driving forces, hydraulically-connected dykes are predicted to exhibit larger magmatic overpressure. In Chapter IV we demonstrate that solidified linkage zones can preserve evidence of magmatic overpressure and suggest the relationship between segment linkage and overpressure is a useful line of inquiry with implications for mineral exploration.

5.3 References

- Barnes, S.J. and Mungall, J.E., 2018, Blade-shaped dikes and nickel sulfide deposits: A Model for the emplacement of ore-bearing small intrusions, *Economic Geology*, v.113, p.789-798.
- Barnes, S.J., Cruden, A.R., Arndt, N. and Saumur, B.M., 2016, The mineral system approach applied to magmatic Ni–Cu–PGE sulphide deposits, *Ore Geology Reviews*, v.76, p.296-316.
- Dahm, T., 2000, On the shape and velocity of fluid-filled fractures in the Earth, *Geophysical Journal International*, v. 142(1), p.181-192.
- Faulkner D.R., Mitchell T.M., Healy D., Heap M.J., 2006, Slip on 'weak' faults by the rotation of regional stress in the fracture damage zone, *Nature* 444 (7121), p. 922-925.
- Mitchell, T., Faulkner, D., 2009, The nature and origin of off-fault damage surrounding strike-slip fault zones with a wide range of displacements: a field study from the Atacama fault system, northern Chile, *Journal of Structural Geology*, v. 31, p. 802-816.
- White, R.S., Drew, J., Martens, H.R., Key, J., Soosalu, H., Jakobsdóttir, S.S., 2011, Dynamics of dyke intrusion in the mid-crust of Iceland, *Earth and Planetary Science Letters*, v.304, p. 300-312.

Appendix I

Dyke tips and melt pathways: Insights from UAV Photogrammetry

Accepted for oral presentation at the 13th International Nickel-Copper-PGE Symposium, September 7-9, 2016, Fremantle, Western Australia, Australia

Gregory Dering¹, Stephen J. Barnes², Steven Micklethwaite³, Alexander Cruden³, Marco Fiorentini¹, and Eric Tohver¹

¹ARC Centre of Excellence for Core to Crust Fluid Systems, School of Earth Science, The University of Western Australia, Crawley, Western Australia 6009, Australia

²Mineral Resources Flagship, CSIRO, Kensington, Western Australia 6151, Australia

³School of Earth, Atmosphere, and Environment, Monash University, Melbourne, Victoria 3800, Australia

*Corresponding author: gregory.dering@research.uwa.edu.au

Abstract

In the context of intrusion-related magmatic sulfide deposits, structural culminations and perturbations are important sites for sulfide melt accumulation. Examples of mineralised culminations include tips of blade-shaped dykes (e.g. Expo intrusive suite, Raglan trend) and keels boat-shaped intrusions (Huangshandong, China). Sites of structural perturbation include step-overs in magma conduits (Discovery Hill dyke, Voisey's Bay) and dyke-sill transitions. Despite the recognition of structural controls on sulfide concentration, magma dynamics and conduit development remain poorly understood in the context of intrusion-related magmatic sulfide deposits. Physical processes of magma emplacement remain enigmatic in part because of limited exposure, post-emplacement deformation, or both. Studies of analogous structural culminations from well-exposed, non-deformed mafic intrusion networks yield insights relevant to emplacement processes and magma dynamics of mineralised systems. To understand conduit growth and magma migration we combine drone-based structural mapping with magnetic fabric analysis, detailed geochemical traverses, and microtomography. This integrated approach is applied to an exceptionally well-exposed suite of gabbroic dykes on south coast of Western Australia. The host rock is Proterozoic orthogneiss and monzogranite of the Albany-Fraser orogen. We map brittle deformation around dyke tips and step-over regions, showing that dyke tip geometry is related to fault-fracture networks developed ahead of the dyke propagation front. Dyke arrest and inflation accounts for the ingress of magma into late-forming faults at dyke tips. Faults and fractures developed around mafic dykes are potential traps for high density, low viscosity sulfide melt.

Appendix II

AN ELEVATED PERSPECTIVE: DYKE-RELATED FRACTURE NETWORKS ANALYSED WITH UAV PHOTOGRAMMETRY

Accepted for oral presentation at the 7th International Dyke Conference, 18-20 August 2016, Beijing, China

Gregory Dering*¹, Steven Micklethwaite³, Stephen J. Barnes², Alexander Cruden³, Marco Fiorentini¹,
and Eric Tohver¹

¹ARC Centre of Excellence for Core to Crust Fluid Systems, School of Earth Science, The University of Western Australia, Crawley, Western Australia 6009, Australia

²Mineral Resources Flagship, CSIRO, Kensington, Western Australia 6151, Australia

³School of Earth, Atmosphere, and Environment, Monash University, Melbourne, Victoria 3800, Australia

*Corresponding author: gregory.dering@research.uwa.edu.au

Abstract

An abundance of data from seismic and geodetic monitoring has provided new insight into dyke propagation and emplacement mechanisms. These studies show that faulting and fracturing is part of the magma emplacement process, preceding and accompanying intrusion on timescales of hours and days. Unfortunately, the precision of earthquake hypocentre locations is typically limited to tens or hundreds of meters, which cannot resolve whether the hypocentres relate to strain of wall rock fragments within the dykes, in a process zone around the intrusion or peripherally in the country rock.

To better understand the distribution and role of brittle deformation associated with dyke emplacement we examine an exceptionally well exposed swarm of 19 dolerite dykes, along a swath of coastline near the town of Albany, Western Australia. The dykes are vertical and emplaced in Neoproterozoic monzogranite of the Albany-Fraser orogen. The age of the dykes is poorly constrained, but probably post-dates the onset of regional exhumation of the monzogranite at 1.1 Ga (Scibiorski et al, 2015). Faults and fractures cross cut foliation in the monzogranite. The fault rocks are cataclasites containing granitic host rock fragments, and no mafic material. An early dyke within the swarm is faulted, whereas other dykes have solidified against the faults. This suggests faulting was on-going during the earliest phase of dyking but preceded the bulk of magma emplacement.

We use Structure-from-Motion photogrammetry and an unmanned aerial vehicle (UAV) for accurate, high resolution 3D reconstruction of outcrop and extraction of structural data. The model is constructed from 1099 images collected from a digital camera mounted to the body of a small quadcopter, flying semi-autonomously over a survey area of $\sim 10,000$ m². Commercial photogrammetry software (Agisoft Photoscan Pro) was used to construct a dense point cloud. From the point cloud, a ground resolution cell size of 3.5 mm was achieved by construction of an orthorectified image mosaicked from the field images, draped on a digital elevation model (DEM) of the same resolution. Internal model accuracy is constrained in 3D by the use of ground control points surveyed with a total station (30-90 mm measurement precision). The locations and orientation of faults, fractures, and dyke margins were sampled along a digital scanline oriented orthogonal to the dyke swarm. Planes were fit to the vertices of 3D fault and fracture traces using a Random Sample and Consensus (RANSAC) algorithm and least squares regression analysis implemented in Java (Thiele et al., 2015).

The cumulative thickness of the 19 dyke segments is ~ 35 m (average aperture 1.8 m) emplaced over a distance of 105 m, measured perpendicular to strike. The first critical observation is that dyke emplacement is accommodated by mode one extension, but the faults and fractures are parallel with the dykes, with a total dispersion of $<20^\circ$. Secondly, the number of faults/fractures increase into the dyke swarm, which has 2.2 ± 0.7 more fractures, per unit length of scanline, in host rocks intruded by dykes relative to the background value. This suggests a broad damage zone developed around the dyke swarm. However, thirdly, within the swarm fractures are heterogeneously distributed such that there is no

measurable systematic distribution of faults and fractures relative to individual dyke segments. Instead, shear failure and fracturing are widely distributed through the volume of host rock affected by dyke emplacement. Faults with measurable displacement have mostly accommodated 10 – 40 cm of dextral shear with a maximum measured displacement of 1.2 m.

These results confirm the surprising observation that dyke-parallel shear failure is closely associated with intrusion events in the middle and upper crust (White et al., 2011; Smith et al., 2004). Our findings differ from numerical models of overpressured dyke propagation in brittle-elastic rock that predict shear failure on faults oriented approximately 30° to the dyke plane (Pollard and Rubin, 1989). We further provide the first evidence that dyke-parallel shear failure occurs in the damage zone associated with a dyke swarm but appears to be unrelated to elevated tensile stress at the leading edges of propagating dykes. Indeed, theoretical predictions of dyke-induced damage suggest damage should decay to a negligible amount over a distance of less than one dyke width perpendicular to the dyke wall (Meriaux et al., 1999). In contrast, we find no systematic variation of damage distribution in the near-field of individual dykes. We suggest the dyke swarm occupies a network of faults and fractures that nucleated prior to and ahead of propagating dykes and remained active during the early stages of emplacement. The mechanics of how such a process operates is not well explained by current theory and remains an outstanding problem.



Figure caption: High resolution UAV photogrammetry orthoimage of dyke tips emplaced in granitic host rock (left). Geologic map of same outcrop showing relations of dykes to faults and fractures (right).

References

- Meriaux, C., Lister, J. R., Lyakhovsky, V., and Agnon, A., 1999. Dyke propagation with distributed damage of the host rock. *Earth and Planetary Science Letters* 165, 177-185.
- Rubin, A. M., and Pollard, D. D., 1988. Dike-Induced Faulting in Rift Zones of Iceland and Afar. *Geology* 16, 413-417.
- Scibiorski, E., Tohver, E., and Jourdan, F., 2015. Rapid cooling and exhumation in the western part of the Mesoproterozoic Albany-Fraser Orogen, Western Australia. *Precambrian Research* 265, 232-248.
- Smith, K. D., von Seggern, D., Blewitt, G., Preston, L., Anderson, J. G., Wernicke, B. P., and Davis, J. L., 2004. Evidence for deep magma injection beneath Lake Tahoe, Nevada-California. *Science*, 305 1277-1280.
- Thiele, S. T., Micklethwaite, S., Bourke, P., Verrall, M., and Kovesi, P., 2015. Insights into the mechanics of en-echelon sigmoidal vein formation using ultra-high resolution photogrammetry and computed tomography. *Journal of Structural Geology* 77, 27-44.
- White, R. S., Drew, J., Martens, H. R., Key, J., Soosalu, H., and Jakobsdottir, S. S., 2011. Dynamics of dyke intrusion in the mid-crust of Iceland. *Earth and Planetary Science Letters* 304, 300-312.

Appendix III

High resolution analysis of dyke tips and segments, using drones

Accepted for oral presentation at the American Geophysical Union Annual Conference, December 12-16, 2016, San Francisco, California

Gregory Dering*¹, Steven Micklethwaite², Alexander Cruden²

¹ARC Centre of Excellence for Core to Crust Fluid Systems, School of Earth Science, The University of Western Australia, Crawley, Western Australia 6009, Australia

²School of Earth, Atmosphere, and Environment, Monash University, Melbourne, Victoria 3800, Australia

*Corresponding author: gregory.dering@research.uwa.edu.au

Abstract

We analyse outstanding exposures of dykes from both coastal (Western Australia) and high altitude glacier-polished (Sierra Nevada, California) outcrops, representing intrusion at shallow upper crustal and midcrustal conditions respectively. We covered 10,000 m² of outcrop area sampling the ground at a scale of 35 mm per pixel. Using Structure from Motion photogrammetry from ground-based and UAV photographs lacking GPS camera positions (>500 images per study), we generated and calibrated a 3D geometry of dense point clouds by selectively using 25-30 ground control points measured by high precision GPS (40-90 mm error). Ground control points used in the photogrammetric model building process typically yielded a root mean square error (RMSE) of 5 cm. Half the ground control points were withheld from the model building process and these yielded RMSE values only 6-10% higher than the points used for georeferencing, suggesting good internal consistency of the dataset and accuracy relative to the reference frame, at least for the purposes of this study. The structural orientations of the dykes and associated fractures were then extracted digitally using the iterative Random Sample Consensus method (RANSAC) and least squares plane fitting. Furthermore, fracture intensity relative to dykes was measured along a series of scanlines and the running average and variance calculated. All results were compared against field measurements. Results show fracture intensity increasing toward the dykes in the shallow crustal West Australian dykes but no such fractures exist around the midcrustal Californian dykes. Despite this there is a remarkable uniformity of geometry, and by implication process, between the two dyke sets. In order to extract full value from the big visual data now available to us, the near future requires dedicated research into software solutions for expert-driven, semi-automatic mapping of geology and structure.

Appendix IV

Relating Seismicity to Dike Emplacement, and the Conundrum of Dyke-Parallel Faulting

Accepted for poster presentation at the American Geophysical Union Annual Conference, December 12-16, 2016, San Francisco, California

Gregory Dering*¹, Steven Micklethwaite³, Stephen J. Barnes², Alexander Cruden³, Marco Fiorentini¹,
and Eric Tohver¹

¹ARC Centre of Excellence for Core to Crust Fluid Systems, School of Earth Science, The University of Western Australia, Crawley, Western Australia 6009, Australia

²Mineral Resources Flagship, CSIRO, Kensington, Western Australia 6151, Australia

³School of Earth, Atmosphere, and Environment, Monash University, Melbourne, Victoria 3800, Australia

*Corresponding author: gregory.dering@research.uwa.edu.au

Abstract

Seismic monitoring shows that faulting and fracturing precede and accompany magma emplacement on timescales of hours and days. One outstanding problem is that the precision of earthquake hypocentre locations is typically limited to tens or hundreds of meters and cannot resolve whether the hypocentres relate to strain of wall rock fragments within the dykes, in a process zone around the intrusion or peripherally in the country rock. We examine a swarm of 19 dolerite dykes, near Albany, Western Australia using an unmanned aerial vehicle and Structure-from-Motion photogrammetry to obtain accurate, high resolution 3D reconstructions of outcrop and to digitally extract structural data. We find rare overprinting relationships indicate dike emplacement and faulting was coeval and that the number of faults/fractures increase into the dyke swarm (2.2 ± 0.7 more fractures, per unit length in host rocks intruded by dykes relative to the background value). The faults are cataclasite-bearing and parallel to the dykes but intriguingly dyke emplacement appears to have been accommodated by mode 1 extension. We further provide the first evidence that dyke-parallel shear failure occurs in a damage zone associated with the dyke swarm. These results support seismological observations of dyke-parallel shear failure associated with some intrusion events, which contradict Mohr-Coulomb theory and numerical modelling of dyke propagation in brittle-elastic rock, where shear failure is predicted to occur on faults oriented approximately 30° to the dyke plane. We suggest the dyke swarm occupies a network of joints and fractures formed prior to swarm emplacement but then reactivated ahead of propagating dykes and remaining active during the early stages of emplacement.

Appendix V

Arrested in the Ivrea Zone: Ni sulfide mineralisation in lower continental crust, La Balma igneous complex (NW Italian Alps)

Accepted for oral presentation at the 14th Biennial SGA Meeting, 20-23 August 2017, Québec City, Canada

Gregory Dering*, Marco Fiorentini, Christopher Gonzalez, Allison Davis

ARC Centre of Excellence for Core to Crust Fluid Systems, School of Earth Science, The University of Western Australia, Crawley, Western Australia 6009, Australia

*Corresponding author: gregory.dering@research.uwa.edu.au

Abstract

Our understanding of how mantle-derived magmas are transferred to sites of ore formation is limited by the accessibility of intrusion networks at crustal roots. The Ivrea Zone (NW Italian Alps) represents a largely intact section of lower to middle continental crust modified in composition and structure by voluminous mantle melts. Exhumation and tilting of the Ivrea Zone reveals an elongate mafic-ultramafic intrusive complex in cross section that hosts Ni-sulfide mineralisation, termed here the La Balma igneous complex, where we investigate mechanisms of magma arrest and sill formation. The complex comprises one or more sills with a cumulative length of at least 9 km and thickness of 400 m. New mapping suggests the mineralised intrusion post-dates voluminous plutonism of the well-studied Mafic Complex and ascended at least 2 km through mafic lower crust. A comparison of the parental melt density with bulk densities for the host rocks under lower crustal conditions shows that buoyancy force is the first order control on the structural level of magma arrest and subsequent sill emplacement.

1 Introduction

Models for emplacement of intrusion-hosted magmatic Ni-Cu-PGE sulfide deposits emphasize ascent of mantle-derived magmas along large, steeply dipping, planar discontinuities (i.e. translithospheric faults and shear zones). However, many world class magmatic Ni-Cu-PGE sulfide deposits exhibit a component of subhorizontal flow and/or emplacement at the deposit scale, including Norlisk-Talnak, Voiseys Bay, and Eagle. Ponding of mantle-derived magma at the Moho and within the lowermost continental crust, commonly referred to as magmatic underplating, is a result of density contrasts between mantle peridotite and less dense overlying crust. The underplating magmas themselves subsequently alter the lithospheric density profile by the addition of dense mafic material to the lowermost crust, with the potential to produce strong layering in regions of the crust interacting with voluminous mantle melts.

P-wave seismic velocity profiles (Rudnick and Fountain, 1995 and references therein) reveal the layering of the deep crust despite the paucity of structurally intact and exposed lower continental crust outcrops, layering of the deep crust is revealed by nonlinear P wave acceleration in seismic velocity profiles (Rudnick and Fountain, 1995 and references therein). Seismic reflection experiments demonstrate the presence of underplated material in tectonic settings including rifts, diffuse extensional provinces, continental margins, and paleosuture zones in Precambrian crust (Thybo and Artemieva, 2013 and references therein). These settings have also been found to be prospective for magmatic Ni-Cu-PGE mineralisation (Begg et al. 2010). The distribution of magmatic Ni-Cu-PGE sulfide deposits in space and time suggests favourable, pre-existing translithospheric structures, combined with active tectonism promote ascent of mantle melts through the crust to form orthomagmatic deposits. What remains poorly

understood is the architecture of crustal-scale magma transport networks that deliver magma to sites of ore formation.

The Ivrea Zone is among the most extensively exposed sections of underplated continental crust and exemplifies the abrupt structural transition from mafic plutonic rocks to overlying metasedimentary rocks at paleodepths of 20 ± 5 km (Demarchi et al., 1998). Here we present new mapping, structural data, and magma density analysis from a mineralised sill complex within the Ivrea Zone, the La Balma igneous complex. These data collectively suggest that pre-existing density contrasts in evolved continental crust influence the emplacement depth and overall intrusion geometry of deep-seated mafic intrusions.

2 Geologic setting

Magmatic underplating has resulted in the emplacement of a large (>200 km³) mafic pluton into lower crustal metasediments, commonly referred to as the Mafic Complex and Kinzigite Formation, respectively. The Kinzigite Formation comprises metapelites, marble, and calc-silicate paragneiss. Within the tilted crustal section, metamorphic grade increases with paleodepth from southeast to northwest from amphibolite to granulite facies (Fig. 1). Westernmost (i.e. deepest) exposures of granulite facies metapelites are strongly restitic, retaining only small amounts of migmatite. The Mafic Complex is considered to be the result of prolonged mantle magmatism from 288 Ma to 259 Ma (Peressini et al., 2007). It is a composite pluton dominated by gabbros and norites. Ultramafic cumulates occur as small, isolated horizons, comprising $<1\%$ of the Mafic Complex. The maximum exposed thickness of the Mafic Complex is ~ 10 km. The roots of the Mafic Complex and underlying mantle peridotite are concealed in the footwall of knapps of the Alpine Orogeny. The boundary between Ivrea Zone and supracrustal Alpine rocks is referred to as the Insubric Line (Schmid et al., 1989). However, in the region between Val Strona and Val Mastallone, the Insubric line is a diffuse zone 10-200 m thick characterised by slivers of mafic rocks tectonically interleaved with mylonitised schists of overlying Alpine knapps. The northern extent of the La Balma igneous complex is overridden and by mylonite of the Insubric Line. Thus our estimate of 9 km for the length of the La Balma igneous complex is a minimum.

Key events in the evolution of the Ivrea Zone through time include: peak metamorphism, timing of mantle-derived magmatism, exhumation, and tilting. P-T conditions of these events are reasonably constrained by a range of geo-barometers and chronometers. Regional metamorphic isograds (Fig. 1) were established during peak granulite-amphibolite facies metamorphism at 299 ± 5 Ma (Vavra et al., 1999). Notably, emplacement of the Mafic Complex post-dates peak metamorphism, with inception of mafic plutonism at 288 ± 4 Ma (Peressini et al., 2007). Garnet and orthopyroxene mineral chemistry show equilibration temperature and pressure within the Mafic Complex increases with paleodepth (Demarchi

et al., 1998). Garnet gabbro from the structurally deepest zone yields equilibration estimates of 730-810°C at 0.7-0.9 GPa, corresponding to a depth of 20-25 km. Granulite-facies Kinzigites cooled slowly to background temperatures of 600°C at 180 Ma (Ewing et al. 2015), suggesting the westernmost Ivrea Zone remained at mid- to lower-crustal depths at least until the early Jurassic. Assuming tilting accompanies exhumation, a range of thermochronometers track extension from 25-30 km depth to surface between the Jurassic and Miocene in the val Strona section of the Ivrea Zone (Wolff et al., 2012).

3 La Balma ultramafic intrusive complex

3.1 Internal architecture

The La Balma igneous complex is a sill or collection of sills with a combined lateral outcrop extent of c. 9-10 km and thickness on the order of 100s of m. The northern half of the La Balma igneous complex is tilted 70-80° SE, roughly concordant with overlying igneous and metasedimentary rocks of the val Strona section. From northwest to southeast, the sill comprises a gradational succession from olivine adcumulate to pyroxenitic orthocumulate (Figure 2). The uppermost portion of the sill is olivine websterite that intrudes overlying amphibole gabbro. The intrusive is contact is complex: blocks of amphibole gabbro roof rocks meters to tens of meters in length are incorporated into pyroxenitic orthocumulates. Partial melting of the gabbroic xenoliths is evident from invasion of ultramafic melt along foliation planes in xenoliths and delicately crenulated intrusive contacts. Late veins of feldspar pegmatoid originate from the partially melted xenoliths and propagate 10s of cm into adjacent pyroxenitic cumulates. The basal contact of the sill is tectonically modified everywhere it has been observed. Brittle shear is focused along the inferred floor of the sill where basal dunite lies adjacent to (Fe)garnet-bearing gabbro in the footwall. Shear fabrics and cataclasite lenses penetrate basal dunite up to 1 m from the contact. The footwall gabbro is injected by cm-scale ultramafic pseudotachylite veins, presumably derived from slip along the contact with adjacent dunite. Deformation along the base of the sill and in the adjacent footwall rocks are the result of brittle-elastic mechanisms at conditions after solidification of the sill complex.

3.2 Ni-sulfide mineralisation

Nickle sulfides occur as disseminated, intercumulus phases. Concentrations of 1-3% are found mainly in lherzolite and harzburgite toward the core of the sill. Pyrrhotite and pentlandite are the dominant sulfide phases with lessor chalcopyrite, mackinawite, and cubanite. Minor disseminations away from the middle of the sill include small (<10 m) pods with 1-3% disseminated sulfides in the basal dunite. WW-II-era adits toward the core of the sill exploit disseminated sulfides and concentrations up to 10% and sparse zones of massive sulfide. These historic ore-grade concentrations occur as elongate north-south bodies, roughly parallel to the strike of the sill. Changes in sulfide concentration are diffuse. The absence of

sharply defined mineralogical horizons, reefs, or abrupt textural changes is consistent with the gradational succession in overall sill composition. Ubiquitous interstitial texture of sulfides suggests sulfur saturation was reached after sill emplacement and during late stages of magma crystallisation.

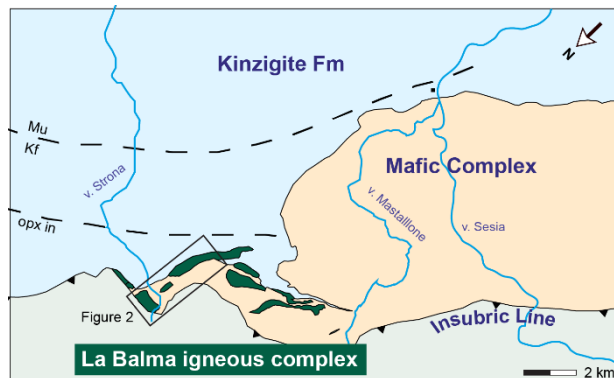


Figure 1. Generalised geologic map of the west-central Ivrea Zone, showing the intrusive contact between the Mafic Complex and overlying Kinzigite Formation, as delineated by Quick et al., 2003. The La Balma igneous complex lies along the margin of the northernmost exposed portion of the Mafic Complex, as mapped by us. Southern extent of the La Balma igneous complex is modified from Ferrario et al. (1984) and Brodie et al. (1992). Map is oriented such that the approximate regional paleo-up direction is toward the top. Metamorphic isograds (dashed lines) denote increasing metamorphic grade.

4 Magma-rock density contrasts

4.1 Rationale

To evaluate the role of pre-existing crustal layering in the emplacement of the La Balma igneous complex, we model a 1D density profile of the Ivrea Zone lower crust around the La Balma igneous complex. The model incorporates mean bulk densities for the Mafic Complex and overlying granulite-facies pelitic gneiss of the Kinzigite Formation. We compare these results with the calculated density for an estimated primary melt of the La Balma igneous complex. Pressure-Temperature (P-T) conditions for the entire system are assigned according to published thermobarometry for the westernmost Ivrea Zone prior to onset of exhumation.

4.2 Host rock densities

For given P-T conditions, in situ density of crustal rocks is a function of bulk composition and modal mineralogy. We use Gibbs free minimization and thermodynamic modelling to determine rock densities based on the above parameters using *Perple_X* (Connolly, 2009) with internally consistent thermodynamic data for solids (Holland and Powell, 1998; rev 2002). Representative average densities for the two host rock units at 740°C and 0.82 GPa are reported in Table 1. Mean density is estimated for

an average bulk composition compiled from new and previously published bulk rock geochemical data from val Strona, val Mastallone, and val Sesia (n=76). The modelled mineral assemblage is characteristic of restitic granulite-facies metapelites. Phases present in trace amounts are excluded to retrieve rock densities irrespective of small (<10%) variation in P, T, and composition for granulite-facies metasedimentary rocks. Density of the gabbroic host rocks is calculated from a mean composition compiled from new and published bulk compositions of gabbro of the Mafic Complex from val Strona and val Sesia (n=21).

4.3 Primary melt density

Calculation of silicate melt density at fixed P-T conditions is based on the bulk rock composition and thermodynamic properties of major oxides. Density of the primary liquid (ρ) has a linear dependence on the properties of each oxide component, summarised by the following equation:

$$\rho = \sum_{i=1}^N \frac{X_i M_i}{V_i}$$

Such that X_i is the mole fraction of each oxide, M_i is the molecular mass, and V_i is the fractional volume of oxide i , and N is total number of oxides that constitute the melt. The effects of P-T on V_i are accounted for by experimentally derived coefficients of thermal expansion and compressibility. New olivine geochemical data have been used to estimate the primary liquid composition to produce peridotite of La Balma igneous complex, reported by Davis et al., 2017 (this volume). Using major element concentrations reported therein, a range of fluid densities for a mantle-derived parental melt are calculated from major oxides following the method of (Table 1). The scenario assumes isothermal ascent of a single batch of mantle-derived high-MgO gabbroic melt at 1300°C and 0.8 GPa, to a site of accumulation within the lower crust. Cooling and crystallisation begin upon arrest and lateral propagation of the melt at its shallowest crustal depth. For high MgO melts at these conditions, SiO₂ and H₂O concentrations disproportionately affect fluid density, as compared with the other major oxides. H₂O content of the primary liquid remains poorly constrained. However, the presence of amphibole disseminated as an intercumulus phase in peridotite suggests the primary melt contained at least some H₂O.

Representative host rocks			Representative primary melts				
	Granulite-facies metapelite	Garnet-bearing gabbro	Primary melt (24% Mgo, 0.5% Ti,	melt 1	melt 2	melt 3	melt 4
Assemblage (0.8 GPa, 750° C)	Ksp + Plg + Gt + Sil + Qtz	Opx + An + Gt(Fe)+Cpx	wt% SiO ₂	48	46	46	45
			wt% H ₂ O	.01	1	0.01	.01
Ivrea zone ρ (this study) (g cm ⁻³)	3.08	3.28	0.8 Gpa, 1300° C	2.96	2.93	3.01	3.04
Lower crustal ρ (Rudnick and Gao, 2003) (g cm ⁻³)	Global average (0.25% H ₂ O)			na	na	na	na
	3.031						

Table 1. Representative rock and silicate melt densities for the west-central Ivrea Zone. Thermodynamically derived densities for Ivrea Zone rocks are greater than global averages for equivalent crustal rocks based on seismic p-wave velocities.

5 Discussion and implications

5.1 Buoyancy force

A wide range of aethenospheric melt compositions are capable of ascending through the lower crust, but only the most mafic, anhydrous endmember (45 wt% SiO₂, 01.% H₂O) is predicted to reach a level of neutral buoyancy at the base of the Kinzigite Formation. Higher silica contents of primary mafic melts reduce density and increase buoyancy contrasts between melt and host rock. The mean density of the granulite-facies Kinzigite Formation is just 1% more than the global average of Rudnick and Gao (2003). Garnet-bearing gabbroic rocks exceed the global average by 6%. Preliminary results reveal the sensitivity of density to small changes in composition at fixed P-T conditions. Such variation is expected in natural systems is exceptionally well characterised in the Ivrea Zone. Future thermodynamic modelling should consider this chemical heterogeneity and uncertainties in empirically determined P-T conditions posed in the literature.

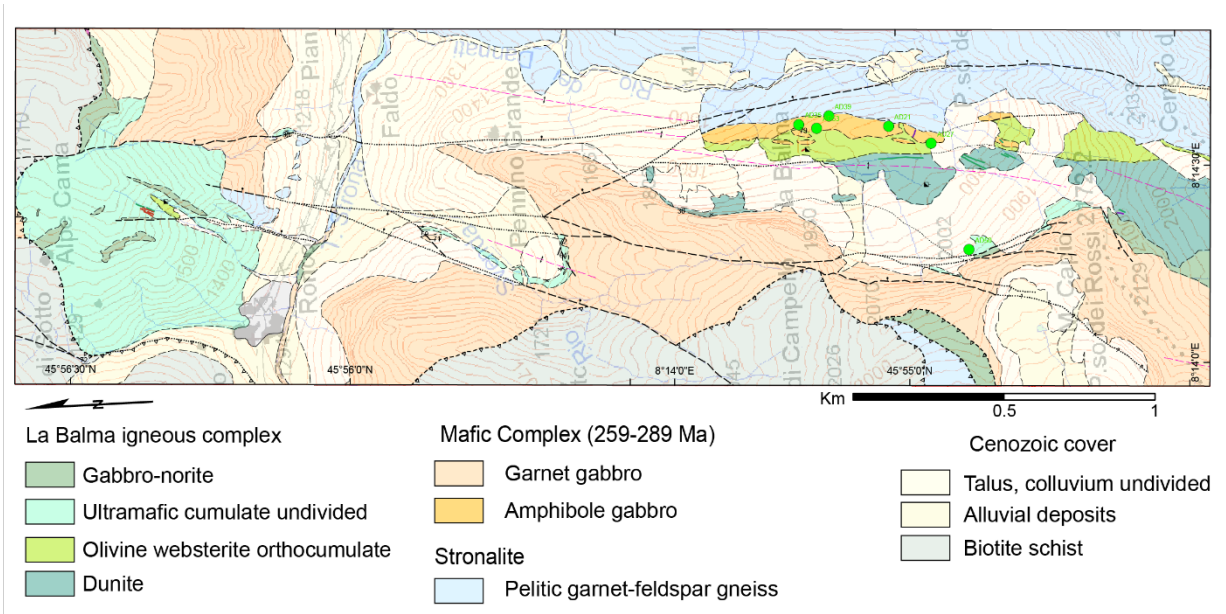


Figure 2. The present structural setting of the La Balma igneous complex preserves a window into primary intrusive relationships related to sill emplacement and differentiation. Amphibole gabbro of the Mafic Complex is partially incorporated into olivine websterite of the La Balma body. Geologic map is oriented such that the approximate inferred paleo-up direction is toward the top.

5.2 Magma transfer through evolved lithosphere

The composition of Post-Archean lower continental crust is commonly bimodal, consisting of peraluminous granulites and mafic rocks. These compositional differences result in density and rheological contrasts. In the Ivrea Zone, the physical contrast is abrupt between metasedimentary granulite and gabbroic rocks. The La Balma igneous complex is a sill or suite of sills resulting from the arrest and differentiation of asthenospheric melt within the lower crust. This process can be understood in terms of density differential by taking into account the bimodal composition and structure of the Ivrea Zone lower crust. Abrupt density contrasts in the lower crust are reasonable in the context of magmatic underplating. Moreover, magmatic underplating is widely documented in a range of tectonic settings also conducive to formation of orthomagmatic ore deposits. We suggest pathways for mantle melts to sites of sulfide accumulation are not only controlled by steep, translithospheric faults and suture zones but also by physical properties of deep continental crust, such as density. Such insights are useful in moving from 2D to 3D characterisation of lithospheric- and camp-scale magma pathways.

References

- Connolly JAD, Petrini K (2002) An automated strategy for calculation of phase diagram sections and retrieval of rock properties as a function of physical conditions. *Journal of Metamorphic Petrology* 20:697-708.
- Begg GC, Hronsky JAM, Arndt NT, Griffin WL, O'Reilly SY, Hayward N (2010) Lithospheric, Cratonic, and Geodynamic Setting of Ni-Cu-PGE Sulfide Deposits. *Economic Geology* 105:1057-1070. doi: DOI 10.2113/econgeo.105.6.1057.
- Brodie KH, Rutter EH, Evans P (1992) On the structure of the Ivrea-Verbano Zone (northern Italy) and its implications for present-day lower continental crust geometry. *Terra Nova* 4:34-40.
- Demarchi G, Quick JE, Sinigoi S, Mayer A (1998) Pressure gradient and original orientation of a lower-crustal intrusion in the Ivrea-Verbano Zone, northern Italy. *The Journal of geology* 106:609-622.
- Ewing TA, Rubatto D, Beltrando M, Hermann J (2015) Constraints on the thermal evolution of the Adriatic margin during Jurassic continental break-up: U–Pb dating of rutile from the Ivrea–Verbano Zone, Italy. *Contributions to mineralogy and petrology* 169:1-22.
- Ferrario A, Garuti G, Rossi A, Sighinolfi GP (1983) Petrographic and metallogenic outlines of the "La Balma-M. Capio" ultramafic-mafic body (Ivrea-Verbano Basic Complex, NW Italian Alps) In: Schneider HJ (ed) *Mineral Deposits of the Alps and of the Alpine Epoch in Europe*. Springer-Verlag, Berchtesgaden, Germany, pp 404.
- Holland TJB, Powell R (2011) An improved and extended internally consistent thermodynamic dataset for phases of petrological interest, involving a new equation of state for solids. *Journal of Metamorphic Geology* 29:333-383.
- Locmelis M, Fiorentini ML, Rushmer T, Arevalo R, Adam J, Denyszyn SW (2016) Sulfur and metal fertilization of the lower continental crust. *Lithos* 244:74-93.
- Peressini G, Quick JE, Sinigoi S, Hofmann AW, Fanning M (2007) Duration of a large mafic intrusion and heat transfer in the lower crust: a SHRIMP U–Pb zircon study in the Ivrea–Verbano Zone (Western Alps, Italy). *Journal of Petrology* 48:1185-1218.
- Quick JE, Sinigoi S, Snoke AW, Kalakay TJ, Mayer A, Peressini G (2003) Geologic map of the southern Ivrea-Verbano Zone, northwestern Italy. US Geological Survey.
- Rudnick RL, Fountain DM (1995) Nature and composition of the continental crust: a lower crustal perspective. *Reviews of geophysics* 33:267-309.
- Schmid SM, Aebli HR, Heller F, Zingg A (1989) The role of the Periadriatic Line in the tectonic evolution of the Alps. *Geological Society, London, Special Publications* 45:153-171.

- Schnetger B (1994) Partial melting during the evolution of the amphibolite-to granulite-facies gneisses of the Ivrea Zone, northern Italy. *Chem Geol* 113:71-101.
- Sinigoï S, Quick JE, Mayer A, Demarchi G (1995) Density-controlled assimilation of underplated crust, Ivrea-Verbano Zone, Italy. *Earth and Planetary Science Letters* 129:183-191.
- Spera FJ (2000) Physical properties of magma. *Encyclopedia of volcanoes*:171-190.
- Thybo H, Artemieva IM (2013) Moho and magmatic underplating in continental lithosphere. *Tectonophysics* 609:605-619.
- Vavra G, Schmid R, Gebauer D (1999) Internal morphology, habit and U-Th-Pb microanalysis of amphibolite-to-granulite facies zircons: geochronology of the Ivrea Zone (Southern Alps). *Contributions to Mineralogy and Petrology* 134:380-404.
- Wolff R, Dunkl I, Kiesselbach G, Wemmer K, Siegesmund S (2012) Thermochronological constraints on the multiphase exhumation history of the Ivrea-Verbano Zone of the Southern Alps. *Tectonophysics* 579:104-117.